

**STRUCTURAL, ELECTRONIC AND MAGNETIC
STUDIES ON COPPER MANGANITE AND
STRONTIUM FERRITE**

COMPUTERISED

A THESIS SUBMITTED TO THE
UNIVERSITY OF POONA
FOR THE DEGREE OF
DOCTOR OF PHILOSOPHY
IN CHEMISTRY



BY
SHAILAJA DILIP KULKARNI

M. Sc.

538.22 : 666.3/.7 (043)
KUL

PHYSICAL CHEMISTRY DIVISION
NATIONAL CHEMICAL LABORATORY
PUNE 411 008 (INDIA)

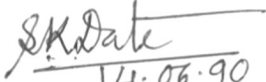
JUNE 1990

COMPUTERISED

CERTIFICATE

This is to certify that the thesis entitled 'Structural, Electronic and Magnetic Studies on Copper Manganite and Strontium Ferrite' describes the research work done by Mrs. Shailaja Dilip Kulkarni under my supervision for the Degree of Doctor of Philosophy in Chemistry of the University of Poona. Such material as has been obtained from other sources has been duly acknowledged in the thesis.

National Chemical Laboratory
Pune 411 008.


14.06.90
(Dr. S.K. Date)
Research Guide

CONTENTS

	<u>Page No.</u>
CHAPTER 1 : GENERAL INTRODUCTION	
1.1 <u>INTRODUCTION TO CERAMICS</u>	1
1.1.1 High-tech ceramics	1
1.1.2 Classification of high-tech ceramics	2
1.1.3 Present status and scope of the research	9
1.2 <u>THEORY OF MAGNETISM</u>	15
1.2.1 Introduction	15
1.2.2 States of isolated ion/atom	17
1.2.3 Ions in the crystalline lattice	19
1.2.4 Ions in the magnetic field	24
1.2.5 Non-cooperative and cooperative phenomenon in solids	30
1.3 <u>PREPARATIVE TECHNIQUES</u>	43
1.3.1 Importance of fine particles	43
1.3.2 Principles underlying the preparative techniques	44
1.3.3 Various preparation methods	45
REFERENCES	54
 CHAPTER 2 : EXPERIMENTAL	
2.1 <u>SYNTHESIS</u>	58
2.1.1 Preparation in general	58
2.1.2 Preparation of strontium hexaferrite : Important features	60
2.1.3 Preparation of copper manganite: Important features	62
2.2 <u>CHARACTERIZATION TECHNIQUES</u>	72
REFERENCES	74

CHAPTER 3 ; STRONTIUM HEXAFERRITE

3.1	<u>INTRODUCTION</u>	75
3.1.1	X-ray and magnetic structure of M-type ferrite	75
3.1.2	Working of a permanent magnet	76
3.1.3	Literature survey	81
3.2	<u>RESULTS AND DISCUSSION</u>	89
3.2.1	Thermal studies	90
3.2.2	XRD studies	96
3.2.3	IR studies	106
3.2.4	SEM studies	109
3.2.5	Mossbauer studies	113
3.2.6	Magnetic properties	115
3.3	<u>SUMMARY</u>	134
	REFERENCES	139

CHAPTER 4 : COPPER MANGANITE

4.1	<u>INTRODUCTION TO SPINELS</u>	143
4.1.1	X-Ray structure of spinel	143
4.1.2	Classification of spinels on the basis of cation distribution	146
4.1.3	Structure of manganite	147
4.2	<u>RESULTS AND DISCUSSION</u>	149
4.2.1	Ceramic technique	149
4.2.2	Coprecipitation technique	156
4.3	<u>SUMMARY</u>	160
	REFERENCES	163
	List of Publications	165
	Acknowledgement	166

CHAPTER 1

General Indrouction

1.1 INTRODUCTION

1.1.1 High-tech ceramics

We approach twenty first century with mixed feelings. Scientific progress has launched us in high-tech era, but at the same time the increasing demand on natural resources have put the sources dwindling to exhaustion. Both these facts have set the scientific community in frantic efforts to develop new materials with superior properties. High-tech ceramics is one such group of challenging materials [1-3]. With the emergence of the new era of engineering plastics and ceramic composites, these materials created a great deal of interest amongst the scientific as well as engineering communities. The discovery of the high temperature superconducting ceramics in 1986 has given a further impetus to the tremendous R and D activities carried out all over the world. The possible use of high-tech ceramics over metals and plastics, has driven the attention of materials scientists towards the unexplored secrets of this field.

Ceramics, by definition, are nothing but nonmetallic materials processed at high temperatures. High-tech ceramics differ from the conventional ceramics by virtue of their novelty of preparation and superior mechanical, electrical/electronic, magnetic and optical properties useful for high technological applications. Beauty of high-tech ceramics is revealed when the requirements include high temperature resistance, electrical resistivity, dielectric strength, corrosion and abrasion resistance, low weight and fracture

toughness. These materials are basically pure and/or mixed oxides, nitrides or carbides of Si, Al, Zr and Fe. The present status of world wide sale of high-tech ceramics has been depicted in Fig. 1 [1].

1.1.2 Classification of high-tech ceramics

These ceramics can be classified into two broad categories namely (a) electronic ceramics and (b) structural ceramics [3]. A more detailed classification of high performance ceramics by function, material and application is provided in Table 1 [2].

1.1.2.1 Electronic ceramics

Electronic applications account for approximately two-thirds of the total market value of the world production of high-tech ceramics. This class can be further divided into the following areas.

(a) Magnetic ceramics

Soft ferrites, hard ferrites, garnets and magnetic recording media form this class of ceramics. Soft ferrites based on Mn-Zn and Ni-Zn ferrites have been in use as magnetic cores in high frequency coils and transformers. High magnetic permeability and low magnetic losses are the two deciding criteria for soft ferrites. Hard ferrites used as permanent magnets basically constitute Ba/Sr hexagonal ferrites. The figure of merit of a permanent magnet is its energy product $(BH)_{\max}$. The usage of hard ferrites covers a variety of applications such as DC permanent magnet motors,

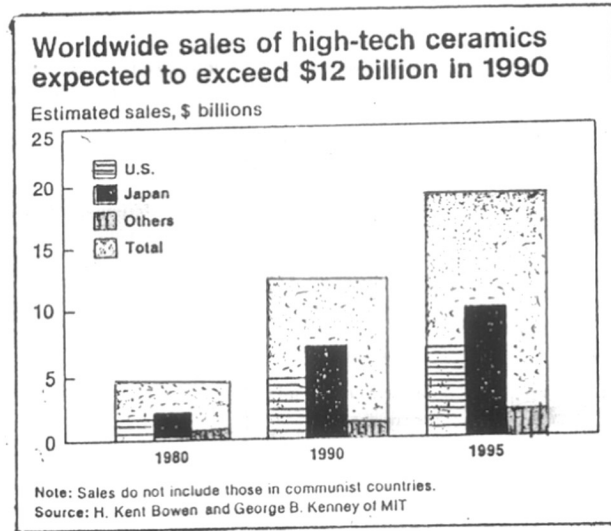


FIG. 1 : World wide sale of high - tech ceramics .

Table-1: Classification of High Tech Ceramics by Function [2]

Electronic/ Electric Functions	Insulation materials (alumina, Beryllium oxide, magnesium oxide)	IC circuit substrate, package, wiring substrates, resistor substrate, electronics interconnection substrate	
	Ferroelectrics materials (Barium titanate, Strontium titanate)	Ceramic capacitor	
	Piezoelectric materials	Vibrator, oscillator, filter etc. transducer, ultrasonic humidifier, piezoelectric spark generator, etc.	
	Semiconductor materials (Barium titanate, silicon carbide, zinc oxide- bismuth oxide, vanadium oxide and other transition metal oxides)	NTC thermistor	Temperature sensor, temperature compensation, etc.
		PTC thermistor	Heater element, switch, temperature compensation, etc.
		CTR thermistor	Heat sensor element
Thick film thermistor		Infrared sensor	
Varistor		Noise elimination, surge current absorber, lighting arrestor, etc.	
Sintered cadmium sulfide material		Solar cell	
Ion conducting materials (beta-alumina, zirconium dioxide)	Silicon carbide heater	Electric furnace heater, miniature heater, etc.	
	Solid electrolyte for sodium battery Zirconia ceramics	Oxygen sensor, pH meter, fuel cells	
Magnetic Functions	Soft ferrite	Magnetic recording head, temperature sensor, etc.	
	Hard ferrite	Ferrite magnet, fractional horse power motors, etc.	
Optical Functions	Translucent alumina	High pressure sodium vapor lamp	
	Translucent magnesium, mullite etc.	For a lighting tube, special purpose lamp, infrared Transmission window materials	
	Translucent yttria-thoria ceramics	Laser material	
	PLZT ceramics	Light memory element, video display and storage system, light modulation element, light shutter, light valve	
Chemical Functions	Gas sensor (zinc oxide, ferric oxide, tin oxide)	Gas leakage alarm, automatic ventilation fan, hydrocarbon fluoro-carbon detectors, etc.	
	Humidity sensor (magnesium chromate-titanium dioxide)	Cooking control element in microwave oven, etc.	
	Catalyst carrier (cordierite)	Catalyst carrier for emission control	
	Organic catalyst	Enzyme carrier, zeolites	
Thermal Functions	Electrodes (titanates, sulfides, borides)	Electrowinning aluminium, photochemical processes, chlorine production	
	Refractoriness/insulation, heat collection (zirconium dioxide, titanium dioxide ceramics)	Infrared radiator, high temperature industrial furnace lining, heat sink for electronic parts	

Table 1 continued

Mechanical Functions	Cutting tools (alumina, titanium carbide, titanium nitride, others)	Ceramic tool, sintered SiN Cermets tool, artificial diamond Nitride tool
	Wear resistant materials (alumina, zirconia)	Mechanical seal, ceramic liner, bearings, thread guide, pressure sensors
	Heat resistant materials (silicon carbide, alumina, silicon nitride, others)	Ceramic engine, turbine blade, heat exchangers, welding burner nozzle, high frequency combustion crucibles
Biological Functions	Alumina ceramics implantation	Artificial tooth root, bone and joint, drug administration
	Hydroxyapatite bioglass	
Nuclear Functions	Nuclear fuels	
	Cladding material (silicon carbide boron carbide, graphite)	
	Shielding material (alumina, silicon/boron carbide, graphite)	

loud speakers, erase heads, magnetos, rubber magnets etc. Mn-Mg garnets and single crystalline garnets have been extensively used in devices like circulators/isolators, phase shifter etc.

(b) Ferroelectric and piezoelectric ceramics

BaTiO_3 is the popular material used as ceramic capacitors with effective dielectric permittivities, while PZT/PLZT i.e. pure and modified lead zirconate titanate still forms basis for most of the ceramic piezoelectric materials.

(c) Ceramic substrates

Ceramics used as substrates had revolutionary impact on electronic industry. Multilayer ceramic packages serve to interconnect IC modules. Heat dissipation in the packaging and time delay introduced due to capacitance of the substrate are the two key factors in the miniaturization of the IC.

(d) Conducting ceramics

Most of the traditional ceramics are insulators but variety of ceramics like SnO , ZnO , ZrO_2 , $\text{La}(\text{Sr})\text{CrO}_3$ and many of the manganites like CuMn_2O_4 show good electrical conductance. Recently Y-Ba-Cu-O and similar systems have been shown to be superconducting even at $\approx 90^\circ\text{K}$ which is likely to be a breakthrough in the technology of power generation and transmission. These conducting ceramics find their use in high temperature fuel cell (stabilized zirconia), thermistors (i.e. temperature dependent resistors) with negative temperature coefficients (e.g. NiO-MnO systems) as well as positive temperature coefficients (La doped BaTiO_3).

Other applications such as varistors (voltage dependent resistors) based on SiC, ZnO have been used for voltage surge protection. The family namely, manganites provided candidates with many new types of magnetic alignment. They offer a field for basic studies such as cooperative Jahn-Teller effect. The unusually high electrical conductivity in case of CuMn_2O_4 has been explained by a hopping mechanism. Ceramic gas sensors based on oxides, are used to analyse O_2 , CO, H_2O , H_2 etc. in the automotive industry for combustion control to meet the pollution control measures. Stabilized ZrO_2 , ZnO, SnO_2 ceramics are the examples, which change their resistance in presence of trace gases. Rare earth perovskites like $\text{La}_{1-x}\text{Sr}_x\text{MO}_3$ ($M = \text{Cr}, \text{Ni}, \text{Fe}$) and even CuMn_2O_4 are the encouraging candidates for the same.

(e) Optical ceramics

Variety of ceramics either transparent or translucent to electromagnetic radiations, come under this category. PLZT (lead lanthanum zirconate titanate) ceramics show transparency which can be varied with the application of electric field (electro-optic effect), useful for fabricating welding goggles, high speed shutters, optical communication systems etc. LiNbO_3 , cordierite (for microwave) sapphire (infrared) are the recent materials.

1.1.2.2 Structural ceramics

Properties like fatigue life, creep strength, thermal shock resistance, fracture toughness are of importance for their applications as structural ceramics. The main drive for development of these ceramics was provided by the

challenging task of design of a ceramic engine operating at high temperature leading to the fuel economy of 30%.

Structural ceramics are classified as follows.

(a) ZrO₂ based ceramics

Toughened zirconia ceramics has got fracture strength and toughness value approaching to those of metals, while its thermal coefficient of expansion matches to that of cast iron, at the same time its thermal conductivity is low. Some of the present problems are (i) low creep resistance in TZP and PSZ, (ii) ageing of PSZ at 150-300°C, (iii) decomposition of t-ZrO₂ in PSZ above 700°C.

(b) SiN and related compounds

SiN shows excellent mechanical properties at high temperatures. It also has low thermal coefficient of expansion, good thermal conductivity and is considered as primary candidate for ceramic engines operating at temperatures >1000°C.

(c) Ceramic composites

The ceramic fibers are incorporated into a ceramic matrix to form a composite having superior properties. Commercially available ceramic fibers are based on SiC and Al₂O₃. PSZ and 2TA are the examples of particulate composites.

(d) Ceramic coatings

Ceramic coatings on metals have been used for protecting metal surfaces from oxidation and chemical corrosion. Carbide based coatings have been used inside

refractory lining of high temperature furnaces to increase the emissivity. Wear resistance coatings of carbide, nitride, and boride are finding greater use in cutting tools and ornaments.

1.1.3 Present status and scope of research

This section reviews the status of magnetic and conducting ceramics, the areas chosen for present study and the scope of the present work.

1.1.3.1 Present status

In magnetic ceramics, permanent magnets (PM) form a major class of compounds. Fig. 2 shows the development of PM from the year 1900 upto 1980 [4]. Pioneering work has been done by Japanese workers. In 1930 an alloy called Alinco was discovered with energy product ≈ 6 MGOe. Major conceptual advance occurred in 1940 when Neel, Kittel and others introduced the idea of single domain particles. In 1950s Phillips (Netherlands) produced permanent magnets based on Ba/Sr ferrites with strong uniaxial magnetic anisotropy and high coercive force with high electrical resistance as an added advantage. These are well suited for the use where the demagnetising fields are high, such as in motors. They use inexpensive materials and are cheap to produce. In 1950 successful attempt was made to produce elongated single domain particles at GE known as ESD magnets. However the coercive force of a PM was lower than the Stoner-Wohlfarth model [5] and the discrepancies led to a newer model of magnetization reversal in single domain particles. Discovery

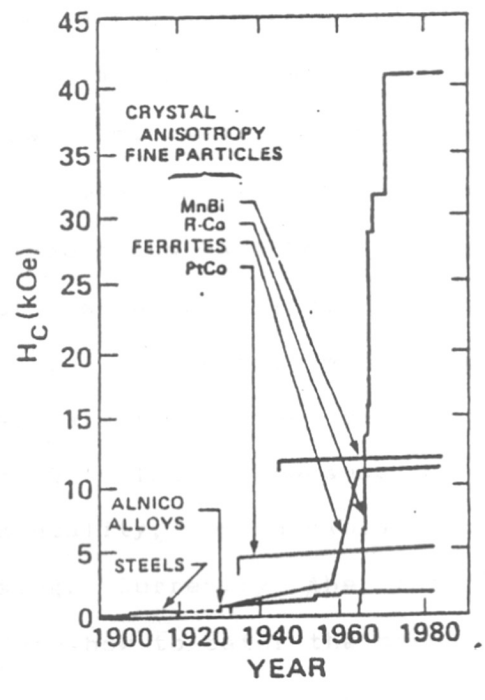
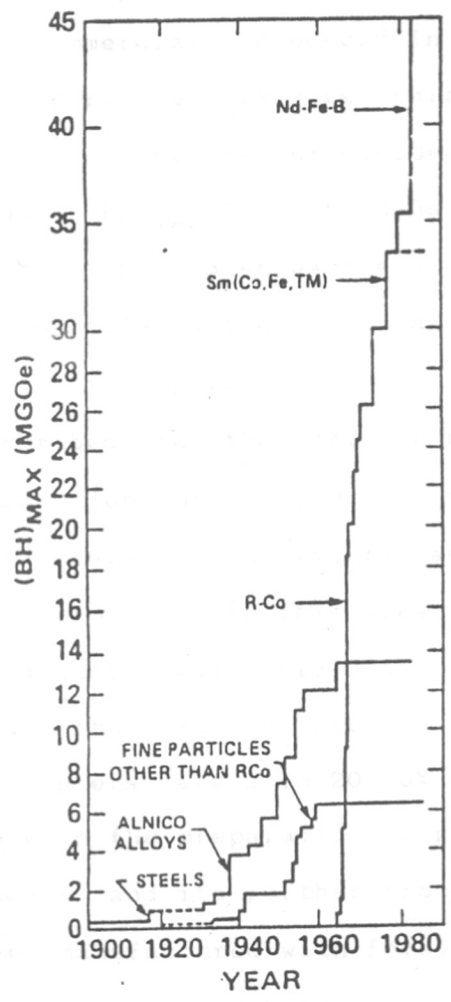
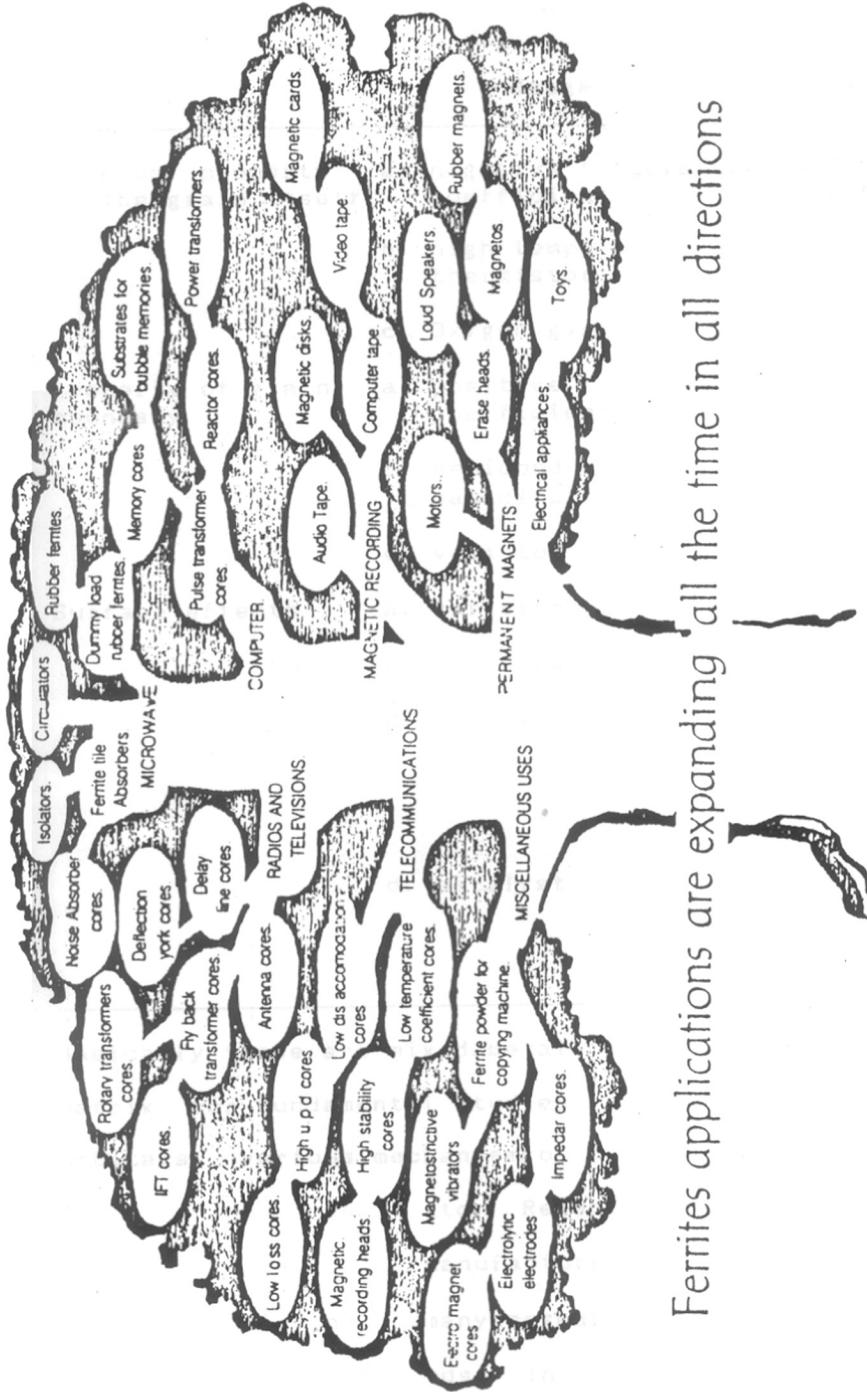


FIG.2 : Energy product and coercivity of permanent magnets.

of rare earth magnets had an revolutionary impact on industry and SmCo_5 magnets (not necessarily single domain particles) was commercially produced in 1970 with $(\text{BH})_{\text{max}} \approx 20 \text{ MGOe}$; but the particles reverse their magnetization by domain wall motion. The recent discovery of $\text{Fe}_{14}\text{Nd}_{12}\text{B}$ magnet in 1983 shows $(\text{BH})_{\text{max}} \approx 30-45 \text{ MGOe}$ but has low Curie temperature = 300°C . Fig. 3 shows the wide applications of hard ferrites which reflects their crucial role in the high technology.

A perspective of the Indian scene has been well described in the article by Jain [6] and Das [3]. The production of ferrites in India commenced about two decades ago. Several laboratories and industries have been actively participating in this area; but the share of India in world production was only 0.4% [6]. The prices are much higher than those in the international market; and the performance parameters are also 20-30% smaller. This is because of the lack in the preparation of good quality, reproducible ferrite powder and its further processing. Currently the ferrites are manufactured with foreign knowhow to cater the needs of the consumer industry.

(B) Conducting ceramics : Table 2 illustrates such ceramics using their various properties [7].



Ferrites applications are expanding all the time in all directions

Y. Hoshino (ICF-5)

FIG. 3 : Applications of ferrites

Table 2 :

Property	Usage	Examples
Physical property of the grain itself	a. negative temperature coefficient	NiO-MnO CuO-MnO systems
	b. high temperature thermistors	NiMn ₂ O ₄
	c. Oxygen gas sensors	PSZ, ZnO
Property of grain boundary	a. positive temperature coefficient	La doped BaTiO ₃
	b. semiconducting capacitors	
	c. varistor	ZnO
Surface effects	a. varistor	BaTiO ₃
	b. gas sensor	SnO ₂ , Fe ₂ O ₃ , ZnO
	c. humidity sensor	ZnO-Cr ₂ O ₃
		MgCr ₂ O ₄ -TiO ₂
d. catalyst	TiO ₂ -V ₂ O ₅ Fe ₂ O ₃ , NiO, Al ₂ O ₃	

Basically these are mixed metal oxides which provide an ideal matrix for fundamental studies [8] such as role of d and f orbitals, various mechanisms of electrical conductance, p-n junction phenomena, etc. Recent trend in the research of these materials is, manufacture of application - oriented products. In India, many research laboratories are busy in studying these compounds. In NCL, spinel manganites [9] and ferrites [10,11] have earlier been studied. Various types of

magnetic interactions, mechanisms for electrical conductance have been proposed. Some of the established systems like thermistors have been taken up by industry and indigenous production is established.

1.1.3.2 Scope of the present work

It is known that fundamental exploratory research regularly produces unexpected but often useful results. The incentive for the present work lies in the vast scope for R & D in exploitation of the well established materials through novel routes of preparation and processing as well as characterizing them with the modern sophisticated techniques such as ESCA, low angle XRD etc. The raw materials required are available in abundance in our country and the demand for high performance ceramics is increasing day by day, so it will be prudent to concentrate for R & D efforts in this area. Mixed metal oxide systems have been selected for the present study. These systems especially magnetic oxides have been traditionally used as ideal matrix for exploring basic concepts in solid state physics. Spin glasses and more recently random magnets have challenged the established concepts [4].

The basic framework of the thesis will be constrained to two particular systems, namely, strontium hexaferrite and copper manganite with the main aim of understanding of the relationship between their properties and the macro, micro and atomic structures. Efforts have been taken to design rather than imperically developing the materials. The urge

and essence of research in this area emphasizes the need for better mechanisms of coupling the science of magnetism and processing technology. Keeping this in mind, elaborate discussion is given on theory of magnetism in Section 1.2 and the preparation and processing techniques in Section 1.3 of Chapter 1.

Chapter 2 describes the experimental and instrumental characterization part while Chapter 3 deals with the results and discussion on Sr hexaferrite. Study on Cu manganite has been well described in Chapter 4.

1.2 Theory of Magnetism

1.2.1 Introduction

Magnetism is one of the basic phenomenon of nature established to understand the unsolved mysteries of the universe. The historical background of magnetism leads one to the remote past when the phenomenon of magnetism was known through a permanent magnet called 'lodestone' which was nothing but Fe_3O_4 found in natural state. In the middle ages, a host of superstitions gathered around the magnet, but the true founder of science of magnetism was William Gilbert in 1600. The electromagnets were discovered by Oersted in 1820. Ewing was the first who considered a magnet, made up of a regular framework of elementary magnets. The phenomenon was understood in more classical way when important law on magnetism was established by Pierre Currie. Modern magnetism based on quantum mechanics was developed by Van Vleck in 1932. Many significant contributions were made by Neel

(ferrimagnetism), Kittel (ferromagnetism and antiferromagnetism), Anderson (exchange interactions) etc.

To understand the basic concepts underlying the term magnetism, one has to analyse the nature of interactions taking place at atomic and/or electronic level. Truly speaking, every material is magnetic in nature as it possesses charged particles which are in continuous motion. Magnetism in any material is mainly due to the motion of electrons. Since the spin magnetic moment of nucleus is smaller by a factor of 10^3 than that of the electrons, it may be neglected. Some of the important concepts are presented below [12-23].

Motion of electron both spinning as well as orbital, results in the nonzero magnetic moment given by following expressions.

$$\text{Orbital magnetic moment} = \mu_l = \frac{-e\omega_0 r^2}{2c} \quad \dots (1)$$

$$= -\frac{e}{2mc} P_l \quad \dots (2)$$

where e = electronic charge, ω_0 = angular velocity of electron, r = radius of circular orbit, c = velocity of light, P_l = orbital angular momentum of electron.

Similarly spin magnetic moment is given by

$$\mu_s = (-e/2mc) \cdot 2 \cdot P_s \quad \dots (3)$$

where P_s = spin angular momentum of electron. The minus sign indicates that the magnetic dipole moment points in the direction opposite to the vector representing the angular momentum.

The understanding of magnetism in solids can be attempted in a stepwise approach as follows.

- (1) Calculation of energy states of atom/isolated ion.
- (2) Calculation of energy states of ions in crystal lattice.
- (3) Effect of magnetic field on ions in the crystal lattice.
- (4) Magnetism in solids as a cooperative effect.

1.2.2 States of isolated ion/atom ;

An isolated ion/atom has number of electrons and its total angular momentum, and so also the total magnetic moment arises from a combination of individual orbital and spin angular momenta. The relative orientations of the orbital and spin moments of various electrons are governed by interactions between the electrons which are mainly of the following type.

- (1) Coulomb interactions, which couple together the orbital motion of the electrons and so also their spin momenta.
- (2) Spin-orbit interactions which magnetically couple the orbital motion of each electron to its own spin.
- (3) Interactions due to the electric field of neighbouring ions of the crystalline lattice.

In this section the coulombic interactions are considered while the other two are dealt with in Section 2.3. When the interelectronic interactions are stronger than spin-orbit interactions, Russel Saunder coupling scheme is used to calculate the total angular momentum of the atom [24,25]. The state of an isolated ion/atom is then represented by $2S+1L_J$ where S, L, J are the integral quantum numbers of

538.22:666.3/.7(043)
KUL

Table 3 : The several terms associated with a given electronic configuration

Configuration	Singlet	Doublet	Triplet	Quartet	Quintet	Sextet
p, p^5	-	P	-	-	-	-
p^2, p^4	S, D	-	P	-	-	-
p^3	-	P, D	-	S	-	-
d^1, d^9	-	D	-	-	-	-
d^2, d^8	S, D, G	-	P, F	-	-	-
d^3, d^7	-	P, D, D, F, G, H	-	P, F	-	-
d^4, d^6	S, S, D, D, F, G, G, I	-	P, P, D, F, F, G, H	-	D	-
d^5	-	S, P, D, D, D, F, F, G, G, H, I	-	P, D, F, G	-	S

atom/ion. Table 3 illustrates number of different states for various electronic configurations.

Out of these several terms the ground term is chosen with the help of Pauli's principle and Hund's rules. For the systems having more than half filled configuration a method called hole formalism is followed.

1.2.3 Ions in crystalline lattice

1.2.3.1 Localised electron model

This model is applied to a crystalline lattice where the perturbation of a central ion by its neighbours is not so very great and an ion to a large degree retains its identity in the crystal. It is customary to express the energy of an atom/ion containing unpaired electrons and nuclei with nonzero spins by a total Hamiltonian as follows [19] :

$$\mathcal{H} = \mathcal{H}_{el} + \mathcal{H}_{CF} + \mathcal{H}_{LS} + \mathcal{H}_{SS} + \mathcal{H}_{Ze} + \mathcal{H}_{HF} + \mathcal{H}_{Zn} + \mathcal{H}_{II} + \mathcal{H}_Q \quad \dots(4)$$

The first three terms constitute the atomic Hamiltonian, and the last six form the spin Hamiltonian. The subscripts mean as follows :

\mathcal{H}_{el} : electronic interactions, \mathcal{H}_{CF} : crystal field interactions, \mathcal{H}_{LS} : spin orbit interactions, \mathcal{H}_{SS} : spin-spin interactions, \mathcal{H}_{Ze} : electronic Zeeman interactions, \mathcal{H}_{Zn} : nuclear Zeeman interactions; \mathcal{H}_{HF} : hyperfine interactions, \mathcal{H}_{II} : nuclear spin interactions, \mathcal{H}_Q : quadrupolar interaction.

The first three terms are the high energy terms. This section mainly deals with the crystal field and spin orbit interactions. The crystal field term \mathcal{H}_{CF} shifts and splits

the electronic energy. This field arises from the electrostatic charges of the ions in ionic compounds and from the chemical bonds in covalent compounds. Crystal field is given by an electric potential of the type $V = \sum_{i,j} \frac{Q_j}{r_{ij}}$, where the summation is over the Q_j ionic charges and i electrons. The above equation is true for the point charge approximation and ordinarily only nearest-neighbour ligands are taken into consideration. Several series of transition elements are categorised in Table 4 [12] according to the amount of various energies.

Table 4 :

	Coulomb energy difference between the ground state and excited state cm^{-1}	Crystal field energies cm^{-1}	Spin orbit energies cm^{-1}
Fe group ions	$10-40 \times 10^3$	$10-20 \times 10^3$	100-800
Pd group ions	$5-20 \times 10^3$	$20-40 \times 10^3$	400-2000
Pt group ions	$5-20 \times 10^3$	$20-40 \times 10^3$	800-5000
rare earth ions	$5-40 \times 10^3$	≈ 200	600-3000

(a) Fe group ions : 3d electrons :

Crystal field effects dominate the spin-orbit coupling but not the Coulomb interactions, so the separate one electron momenta still couple to give resultant orbital angular momentum and spin angular momentum separately. But

the directions of P_L and P_S are strongly influenced by crystal fields, where P_L = orbital angular momentum of atom, P_S = spin angular momentum of atom.

(b) Other transition series : 4d, 5d electrons :

Crystal field and spin-orbit effects are comparable with the Coulomb terms.

(c) Rare earth ions : 4f and 5f electrons :

Since crystal field effects are small, Coulombic interactions within the central ion remain dominant and spin-orbit coupling exercises a greater control over the orientations of spin and orbital angular momenta.

Since our study is mostly related to 3d electron systems only, we will concentrate more on 3d systems.

1.2.3.2 3d systems

For 3d systems, following expression describes relative magnitude of the components of \mathcal{H} expressed in cm^{-1} .

$$\mathcal{H}_{el} (\approx 2 \times 10^4 \text{ cm}^{-1}) > \mathcal{H}_{cub} (10^4 \text{ cm}^{-1}) \gg \mathcal{H}_{noncub} (2 \times 10^2 \text{ cm}^{-1}) \approx \mathcal{H}_{LS} (2 \times 10^2 \text{ cm}^{-1})$$

$$\text{where } \mathcal{H}_{CF} < \begin{matrix} \mathcal{H}_{cub} \\ \mathcal{H}_{noncub} \end{matrix}$$

The strength of crystalline field is defined qualitatively as follows :

if $\mathcal{H}_{el} \gg \mathcal{H}_{CF} \rightarrow$ CF is weak

$\mathcal{H}_{el} > \mathcal{H}_{CF} \rightarrow$ CF is medium

$\mathcal{H}_{el} \approx \mathcal{H}_{CF} \rightarrow$ CF is strong.

In case of 3d electrons, since $\mathcal{H}_{CF} \gg \mathcal{H}_{LS}$, J is no longer a good quantum number and one has to consider first the splittings of the orbital moment by crystalline field, then the additional LS splitting has to be considered. As an

example, the splitting of 2D state under octahedral crystalline field has been described in Fig. 4.

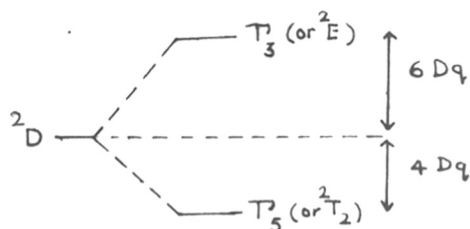


Fig. 4 : The splitting of a 2D free ion state (of $3d^1$ ion) in an octahedral field.

The number and types of components into which an octahedral or tetrahedral field will split a given state L , is the same regardless of the d^n configuration from which it arises and these facts are summarised in Table 5.

Table 5

State of free ion	Mulliken notation	Bethe notation
S	A_1	T_1
P	T_1	T_4
D	$E + T_2$	$T_3 + T_5$
F	$A_2 + T_1 + T_2$	$T_2 + T_4 + T_5$
G	$A_1 + E + T_1 + T_2$	$T_1 + T_3 + T_4 + T_5$
H	$E + 2T_1 + T_2$	$T_3 + 2T_4 + T_5$

Such energy level diagrams are drawn for each electronic configuration and called as Tanabe Sugano diagrams [25].

1.2.3.3 Quenching of the orbital momentum

In case of the 3d ions, the crystal field acts on the orbitals of the electrons so that they continuously change their orientations. This situation in which each component of the orbital momentum is zero on average, is known as the "quenching of the orbital momentum" by the crystal field [13]. It has important consequence in magnetism, greatly reducing the contributions which orbital motion can make to the magnetic effects. Stoner suggested the following explanation for the different behaviour of the rare earth and iron group ions in this respect. In the iron group ions, the paramagnetic 3d electrons are the outermost electrons and these are therefore fully exposed to the crystalline field. Consequently the orbital motion is locked into the field of the neighbours and cannot orient itself in an external magnetic field. On the other hand in case of the rare earth ions, paramagnetic 4f electrons lie relatively deep inside the ions and the outer electrons occupy 5s and 5p levels. The screening of the 4f electrons from the crystalline field thus leaves the orbit of 4f electrons practically the same as in the free ion.

1.2.3.4 Effect of the spin-orbit interaction

The spin angular momentum P_S and orbital angular momentum P_L are associated with magnetic fields and their interaction is given by the 'spin-orbit' Hamiltonian.

$$\mathcal{H}_{LS} = \lambda P_L \cdot P_S \quad \dots (5)$$

where λ is the spin orbit coupling constant. It results in

the polarization or distortion of the orbital wave function by the spin and this reintroduces a small component of orbital momentum inspite of the crystal field quenching. The spin-orbit coupling then removes the orbital degeneracy, one typical case of 2D state being illustrated in the Fig. 5.

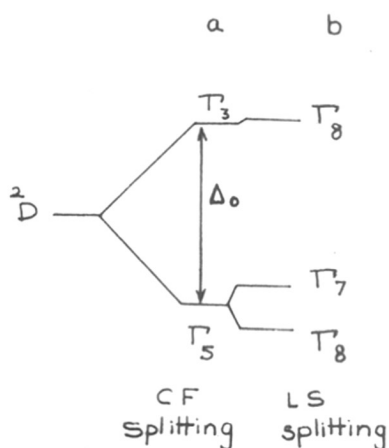


Fig. 5 : Energy levels of 2D free ion (d^1 system) split by
 a) an octahedral crystalline field and
 b) spin-orbit L S splitting

For the Fe group ions, λ ranges from 100 cm^{-1} to 1000 cm^{-1} and so Δ_0 is $\approx 10^4 \text{ cm}^{-1}$.

Table 6 gives the spin-orbit splitting of the various states.

1.2.4 Ions in the magnetic field

The discussion so far was restricted to calculate the states of the ions in the crystalline field, in terms of the spin, orbital and resultant angular momenta of the

Table 6 : Spin - orbit splitting of various electronic states.

	$s = 1/2$	$s = 1$	$s = 3/2$	$s = 2$
Γ_1	Γ_6	Γ_4	Γ_8	$\Gamma_3^+ \Gamma_5$
Γ_2	Γ_7	Γ_5	Γ_8	$\Gamma_3^+ \Gamma_4$
Γ_3	Γ_8	$\Gamma_4^+ \Gamma_5$	$\Gamma_6^+ \Gamma_7^+ \Gamma_8$	$\Gamma_1^+ \Gamma_2^+ \Gamma_3$
Γ_4	$\Gamma_6^+ \Gamma_8$	$\Gamma_1^+ \Gamma_3^+ \Gamma_4^+ \Gamma_5$	$\Gamma_6^+ \Gamma_7^+ 2 \Gamma_8$	$\Gamma_2^+ \Gamma_3^+ 2 \Gamma_4^+ 2 \Gamma_5$
Γ_5	$\Gamma_7^+ \Gamma_8$	$\Gamma_2^+ \Gamma_3^+ \Gamma_4^+ \Gamma_5$	$\Gamma_6^+ \Gamma_7^+ 2 \Gamma_8$	$\Gamma_1^+ \Gamma_3^+ 2 \Gamma_4^+ 2 \Gamma_5$

atom/ion namely P_L , P_S and P_J . With this background, an expression has to be found out for the magnetic responses of the ions when kept in the external magnetic field H , in terms of the above mentioned quantities. It should be noted that effect of the applied magnetic field (upto 30,000 Oe) changes the energy of the ion by a very small amount (few cm^{-1}) compared to that caused by the spin-orbit and crystal field splitting.

In order to calculate the effect of external field H , one has to find the Hamiltonian of a single electron moving in an electric field E and magnetic field H . It is normally derived from its classical energy function and as a first step, we might anticipate the following form of \mathcal{H} which does not contain magnetic field, as it does no work on the electron during its stationary state of motion.

$$\mathcal{H} = [1/2m (mv^2)] - e\phi \quad \dots (6)$$

The first term belongs to the kinetic energy and the second to the potential energy, ϕ being the scalar potential function of the electric field. \mathcal{H} can be expressed in terms of the conjugate momentum coordinate p , given by

$p = mv - (e/c) A$, where A = vector potential of H , therefore

$$\mathcal{H} = 1/2m [p + (e/c) A]^2 - e\phi \quad \dots (7)$$

putting $A = 1/2 H \times r$ for uniform H (r = position vector of electron w.r.t. origin) and $P_L = r \times p$

$$\mathcal{H} = \frac{p^2}{2m} + \frac{\mu_B}{\hbar} H \cdot P_L + \frac{e^2}{8mc^2} (H \times r)^2 - e\phi \quad \dots (8)$$

where μ_B = Bohr magneton

In the second step, this \mathcal{H} is modified by considering interaction between H and μ_S (spin magnetic moment of

electron). Now summing over all the electrons, we get the Hamiltonian for an ion in magnetic field as follows,

$$\mathcal{H} = \left[\sum_i \left(\frac{P_L^2}{2m} - e\phi_i \right) + \sum_{i,j} \frac{e^2}{r_{ij}} + \lambda P_L \cdot P_S \right] + \frac{\mu_B}{\hbar} H \cdot (P_L + 2P_S) + \sum_i \frac{e^2}{8mc^2} (H \times r_i)^2 \quad \dots (9)$$

The part enclosed in the square bracket is the Hamiltonian for the ion in the absence of magnetic field. The scalar potential Φ includes the fields due to the nucleus and to the neighbouring ions. The remaining two terms are perturbation due to H. The magnetic part of the energy is thus

$$E_H = \frac{\mu_B}{\hbar} \langle H \cdot (P_L + 2P_S) \rangle + \frac{e^2}{8mc^2} \langle \sum_i (H \times r_i)^2 \rangle \quad \dots (10)$$

The expectation or mean value is denoted by $\langle \rangle$. If H is in z direction then,

$$E_{H_z} = \frac{\mu_B}{\hbar} H \langle (P_{L_z} + 2P_{S_z}) \rangle + \frac{e^2}{8mc^2} H^2 \langle \sum_i (x_i^2 + y_i^2) \rangle \quad \dots (11)$$

The operator for the magnetic moment of the ions can be derived directly by differentiation of \mathcal{H} w.r.t. H, and the magnetic moment in the z direction is given by

$$\begin{aligned} \mu_z &= - \frac{\mu_B}{\hbar} (P_{L_z} + 2P_{S_z}) - \frac{e^2}{4\pi mc^2} \sum_i (x_i^2 + y_i^2) H \quad \dots (12) \\ &= \mu_z^p + \mu_z^d \quad \text{say.} \end{aligned}$$

If z direction is that of H then equation reduces to

$$E_H = - \langle \mu_z^p \rangle H - \frac{1}{2} \langle \mu_z^d \rangle H$$

If first ordered approximation is involved, then the first term in the equation (11) is linear with H and $\langle \mu_z^p \rangle$ is field independent or "permanent moment". It can be positive or negative depending on the quantum state in question, but when thermal equilibrium distribution of many ions over the accessible states are computed, it is found that this term is

responsible for strong paramagnetism. Similarly, to a first order approximation, the second term in the equation (11) is proportional to H^2 . It is clearly positive (the associated moment μ_z^d is necessarily negative) and the term is responsible for diamagnetism.

Thus the magnetic energy in the z direction of a free ion due to its permanent moment is as follows :

$$\begin{aligned}
 E_H &= -\mu_z H = \frac{\mu_z}{P_{Jz}} \times H \times P_{Jz} \\
 &= g \times \frac{\mu_B}{\hbar} \times P_{Jz} \times H \\
 &= g \mu_B M_J H \quad \dots (15)
 \end{aligned}$$

The relationship between the angular momenta and the magnetic moment can be seen in the Fig. 6.

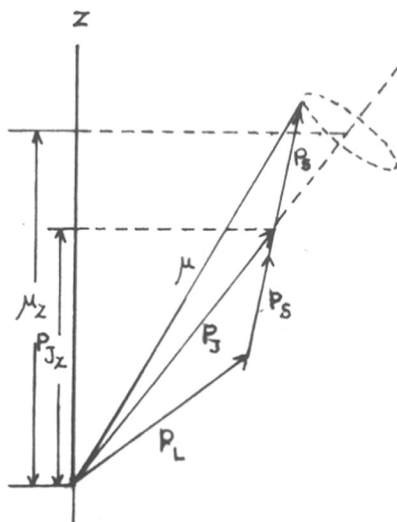


Fig. 6 : The relationships between the angular momenta and the magnetic moment

The final picture of a given electronic level (e.g. 2D) [12] by various perturbations can be seen in Fig. 7.

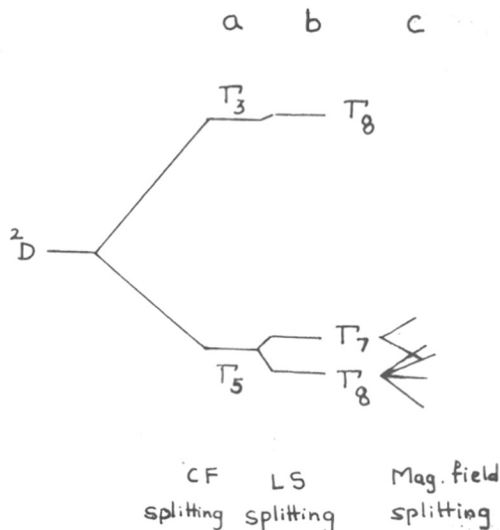


Fig. 7 : Energy levels of 2D free ion (d^1 system) split by
 a) an octahedral crystalline field
 b) spin orbit L S splitting
 c) effect of magnetic field

Iron group ions in the crystal :

For this group, crystal field effects dominate L-S coupling, with the result that the stationary states are not the states of J but in most of the cases can be calculated approximately as states of definite $|P_L|^2$, $|P_S|^2$ and P_{S_z} . When spin-orbit polarization is neglected, E_H is given by

$$E_H = g \mu_B M_S H \quad \dots (16)$$

where $g = 2$ (spin only value).

When the spin-orbit polarization is introduced, the mean value of P_L is no longer zero and the magnetic energy due to interaction between H and the residual orbital moment is of the form $\mu_B H \frac{C\lambda}{\Delta}$ where C is a number between 1 and 10 and of opposite sign for the two spin states, while Δ is the crystal field parameter, equal to 10 Dq in case of 3d ions. The magnetic energy due to the spin moment is unchanged, but the splitting of the levels by the magnetic field is therefore slightly different from the spin only value, due to the spin-orbit polarization. If we want to retain the same expression as above for E_H then

$$E_H = g \mu_B M_S H \quad \text{with } g = 2 \pm \sim \frac{C\lambda}{\Delta}$$

where λ is between 100-1000 cm^{-1} and $\Delta \simeq 10^4 \text{ cm}^{-1}$ for Fe group ions.

1.2.5 Non-cooperative and cooperative phenomena in solids

With the background on origin of magnetism in the atoms/ions in the crystalline fields, it is appropriate to switch over to the magnetic behaviour of solids. This aspect can be divided into two categories.

(A) Non-cooperative phenomenon where individual magnetic dipoles do not interact with each other e.g. (i) diamagnetic solids and (ii) paramagnetic solids.

(B) Cooperative phenomenon where the magnetic dipoles interact with each other giving rise to three main kinds of behaviour namely (i) ferromagnetism, (ii) antiferromagnetism, (iii) ferrimagnetism.

Any solid when placed in the magnetic field H , develops a certain amount of magnetization M defined as the magnetic moment per unit volume and is given by $M = \chi H$ where χ is known as magnetic susceptibility. For isotropic materials, M and H are in the same direction and χ is scalar while for the anisotropic materials M and H are not necessarily in the same direction and χ is a tensor. The magnetic induction B is defined as

$$B = H + 4 \pi M \quad \dots (17)$$

μ , the permeability of the material is given as

$$\mu = B/H = 1 + 4 \pi \chi \quad \dots (18)$$

1.2.5.1 Non-cooperative phenomenon

(A) Diamagnetism : This results from the perturbation of the orbital motion of electrons due to the force which each electron experiences when moving in the magnetic field. The change is negative as it opposes the applied field. As a result the orbital precesses round the field direction. The classical expression for diamagnetic susceptibility is given

by Langevin as follows : $\chi_d = - \frac{Ne^2}{6mc^2} \sum_i \overline{r_i^2}$

where $\overline{r_i^2}$ = mean square distance between electron and nucleus; N = ions/atoms per unit volume; m, e = mass and charge of the electron respectively; c = velocity of light.

The order of χ_d is $\approx 10^6$ emu.

(B) Paramagnetism : Paramagnetic magnetization is in the same direction as the applied field and arises from partial alignment of permanent atomic/electronic dipole moments. Paramagnetism appears only in the solids containing unpaired

electrons. The paramagnetic volume susceptibility χ_p depends strongly on temperature, according to the Curie-Weiss law,

$$\chi_p = \frac{c}{T - \Theta} \quad \dots (20)$$

where c = Curie constant, T = absolute temperature and Θ = Weiss constant. For cases with the iron-group ions in crystals, where $\mathcal{H}_{CF} > \mathcal{H}_{LS}$, χ_p is given as follows,

$$\chi_p = \frac{N \mu_B^2}{3KT} g^2 S'(S'+1) \quad \dots (21)$$

where S' is the ground state value of the quantum number S , $g = 2$ and remaining symbols carry the usual meanings. For cases where $\mathcal{H}_{CF} < \mathcal{H}_{LS}$

$$\chi_p = \frac{N \mu_B^2}{3KT} g^2 J'(J'+1) \quad \dots (22)$$

(J' is ground state value of J).

1.2.5.2 Cooperative phenomenon

Materials belonging to this class have their elementary magnets, spontaneously oriented by some kind of mutual interactions. The spontaneous ordering can be inferred from the observations namely (i) existence of remanent magnetization, (ii) characteristic discontinuities in the variation of specific heat with temperature and (iii) the diffraction patterns formed by the scattering of slow thermal neutrons from single crystal samples. Three main types of ordering namely (A) ferro-magnetism, (B) antiferro-magnetism, (c) ferrimagnetism will be discussed in details. Various kinds of ordering along with their names have been shown in Fig. 8.

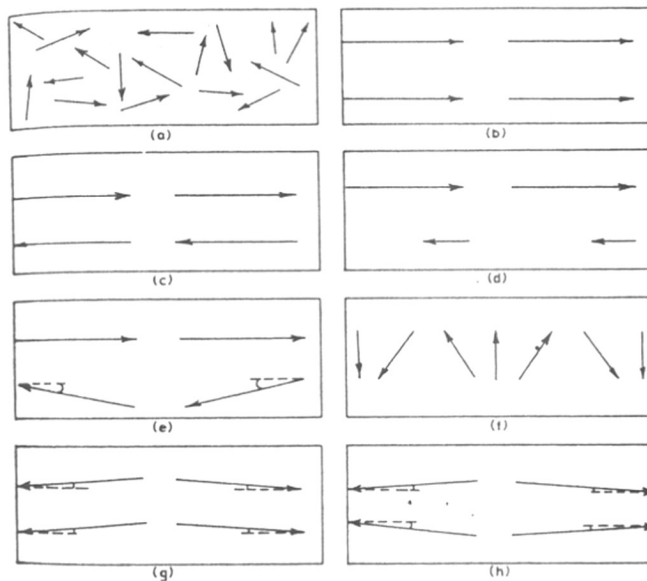


Fig. 8 : Schematic representation of spin arrangements :

- a) disordered paramagnetic state
- b) parallel spins : ferromagnetism
- c) antiparallel spins: Neel type antiferromagnetism
- d) uncompensated antiparallel spins : Neel type ferrimagnetism
- e) triangular antiparallel spins : Yafet-Kittel type ferrimagnetism
- f) helical spiral structures : compensated antiferromagnetic or uncompensated ferrimagnetic
- g) canted spin Dzialoshinskii type weak ferromagnets
- h) canted spins compensated antiferromagnets : hidden canting

Ferromagnetism

The intense response to an applied magnetic field is known as ferromagnetism. The complex behaviour of ferromagnetism is divided into two major directions, (a) the occurrence and magnitude of the spontaneous magnetization M_S existing at every point in the solid and (b) the way in which this spontaneous magnetization is distributed in any

direction, in the form of regions called as domains. The first aspect, attempts to answer questions of the kind "why is metal A ferromagnetic while metal B is not?" The second aspect, i.e. the theory of domains answer the questions of the kind "why is a ferromagnetic metal C, more easily saturated than a ferromagnetic metal D?"

(a) The first aspect tells about (i) the nature of elementary magnetic moments contributing to the order and (ii) the extent to which the order is disturbed by thermal agitation KT .

(i) The nature of elementary magnetic moments has been discussed in details in the previous sections. Basically it is due to the permanent magnetic moments associated with the ions/atoms. The spontaneous character of magnetism is most directly revealed by the existence of permanent magnets and the ease with which (e.g. $H \leq 1$ Oe) they are magnetized to saturation. The simple magnetic force exerted by one atomic dipole on its neighbours can not be taken responsible for the spontaneous ordering because the interaction field is only $\approx 2 \times 10^3$ Oe, while the force causing spontaneous ordering is equivalent to a field of 10^6 Oe. The origin of this force will be discussed later.

(ii) With temperature, the spontaneous magnetization drops down due to thermal agitation and at $T = T_c$ known as the Curie temperature, it falls to zero, because the magnetic dipoles become more and more randomly oriented as temperature is raised. The direction of the spontaneous magnetization

can be changed by the external magnetic field, but its magnitude is only very weakly dependent on the intensity of the applied magnetic field.

(b) The second aspect about the origin and distribution of the spontaneous magnetization leads to the theory of domains.

Weiss model for localised electrons : The first model for ferromagnetism was devised by Weiss (1907) who introduced two hypotheses, namely, (i) each ferromagnetic material is composed of small regions called domains, within which the spins are ordered in parallel below T_c , but the direction of magnetization of different domains need not necessarily be parallel and (ii) a strong internal molecular field H_m called as Weiss field is responsible for the parallel alignment of the individual atomic moments within the domain.

Only an external magnetic field H would align the individual domains within the crystal and yield its full magnetic moment called the saturation moment or M_{sat} . The molecular field H_m may be written in the following form,

$$H_m = H_{ap} + \lambda M \quad \dots (23)$$

where λ = molecular field constant or Weiss constant. The above equation leads further to the existence of a ferromagnetic Curie point and the Curie-Weiss law. An expression for spontaneous magnetization can be derived by using statistical theory of paramagnetism. Two influences, namely, the ordering influence of the molecular field, and the disordering effect of thermal agitation of the magnetic dipoles, have to be considered. For a paramagnetic sample

$$M = M_m B_J (\mu_m H/kT) \quad \dots (24)$$

where M_m is the saturation magnetization that would be attained in an internal field with all dipoles of moment μ_m aligned and $B_J(x)$ is the Brillouin function given by

$$B_J(x) = (2J+1/2J) \coth (2J+1/2J) x - (1/2J) \coth x/2J \quad \dots (25)$$

where J is the total angular momentum quantum number of the ion. M is the magnetization and H is the applied field.

Putting $H = H_{ap} + \lambda M$, we have

$$\frac{M_s}{M_m} = B_J \left(\frac{\mu_m \lambda M_s}{kT} \right) \quad (\because \lambda M \gg H_{ap}) \quad \dots (26)$$

where M_s = spontaneous magnetization due to molecular field.

When both sides of equation (26) are plotted against

$\mu_m \lambda M_s/kT$ in Fig. 9, the two curves intersect at the point 0 corresponding to $M_s = 0$ and at point x.

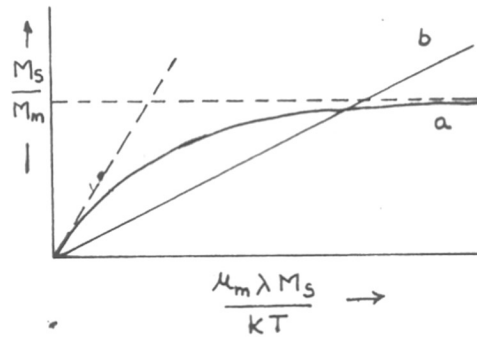


Fig. 9 : Graphical determination of M_s (spontaneous magnetization)

The value of M_s at x represents a stable solution. Since the slope of the line M_s/M_m changes with temperature, we can find a temperature T_c such that the slope of the line is just equal to the slope of the curve for B_J , the only point of

intersection is at the origin and at this and higher temperatures there will be zero spontaneous magnetization.

At temperature T_c slope of line (a) is given by

$$\frac{kT_c}{\mu_m \lambda M_m} = \frac{J+1}{3J}$$

$$\therefore \mu_m = g \mu_B J$$

$$\text{and } M_m = N_g \mu_B J$$

N being the number of dipoles per unit volume.

$$\begin{aligned} T_c &= \frac{J+1}{3J} \frac{\lambda}{k} \mu_m M_m = \frac{J(J+1)}{3k} g^2 \mu_B^2 N \lambda \quad \dots (27) \\ &= \lambda C \quad \left(\because C = N g^2 \mu_B^2 \frac{J(J+1)}{3k} \right) \end{aligned}$$

Equation 26 can be rewritten as,

$$M_s/M_m = B_J \left[(3J/J+1)(T_c/T)(M_s/M_m) \right] \quad \dots (28)$$

For a given choice of J the variation of M_s/M_m with T/T_c depends only on the form of B_J and not upon μ_m , λ or N (i.e. parameters depending on material). This dependence is shown in Fig. 10, for experimental measurements on Fe, Ni and Gd, along with the theoretical curves predicted by Weiss model.

At $T > T_c$, ferromagnetic materials go over to paramagnetic phase, molecular field approach still can be used to derive the Curie-Weiss law, provided we retain H_{ap} along with λM since now they are of same order of magnitude. The Curie-Weiss law, is given as

$$\chi = M/H_{ap} = C/T - T_c \text{ where } C = \frac{N \mu_B^2 g^2 J(J+1)}{3k} \quad \dots (29)$$

and $T_c = \lambda C$

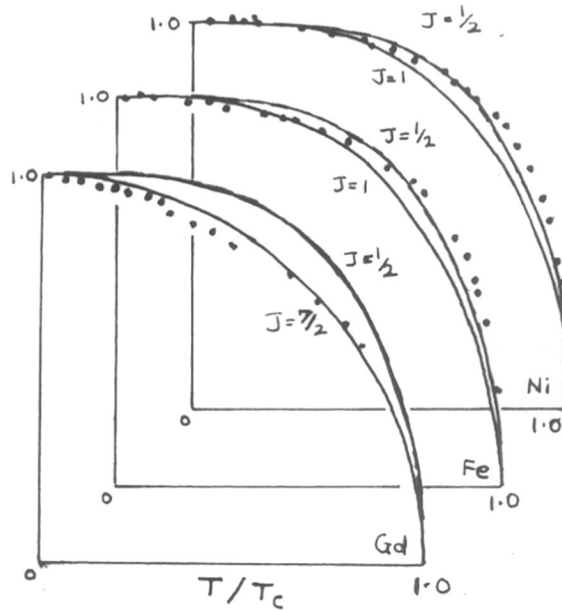


Fig. 10 : Measured variations of M_s/M_m with reduced temperature T/T_c for Ni, Fe and Gd (the points) compared with the theoretical curves (the lines)

Interpretation of Weiss field :

The origin of Weiss field was attributed to the quantum mechanical exchange interaction by Heisenberg, Frenkel and Dirac. The exchange interaction is given by exchange Hamiltonian which expresses the sum of the total interactions between two atoms having spins S_i and S_j as,

$$\mathcal{H}_{ex} = -2 \sum_{i,j} J_{i,j} S_i \cdot S_j$$

where $J_{i,j}$ is the exchange integral which is a measure of the overlap of the electronic charge distribution of two atoms. This Hamiltonian was replaced afterwards by Weiss Hamiltonian which is the sum of many one electron Hamiltonians given by

$$\mathcal{H}_w = -g_J \mu_B H N S_z \quad \dots (30)$$

Limitations of Weiss model :

(i) The values of λ calculated from the observed Curie

temperature from Eq. (27) does not agree with that obtained from the paramagnetic Curie temperature obtained from Eq. (29). On the other hand if λ is assumed to be constant, the measured properties would suggest that the ionic moment is variable. (ii) Moreover the ionic moment is not an integral number of Bohr magnetons for any metals of the transition element.

Specific heat and ferromagnetism :

When a ferromagnetic sample is heated, the thermal energy appears in part as an increase in the exchange energy associated with the decrease in magnetic order. This is therefore a 'magnetic' contribution to the specific heat. In the molecular field approximation, the total exchange energy is the self energy of the sample in the molecular field, so that the contribution of the exchange effects to the internal energy per unit volume is,

$$E_m = -1/2 \lambda M_s^2 \quad \dots (31)$$

The magnetic part of the specific heat C_m at constant volume thus can be derived as

$$C_M = \frac{1}{\rho} \cdot \frac{\partial E}{\partial T} = \frac{\lambda M_s}{\rho} \cdot \frac{\partial M_s}{\partial T} \quad \dots (32)$$

where ρ = density, M_s = saturation magnetization.

The dependence of C_m on temperature can be derived from M_s versus T curve. Dependence of C_m on T/T_C is shown in Fig. 11. A sharp maximum in C_m at $T = T_C$ is characteristic of all ferromagnetic metals.

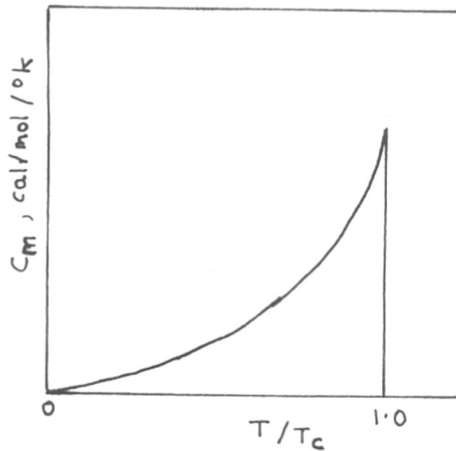


Fig. 11 : The variation of C_m with temperature

(B) Neel's theory for antiferromagnetism and ferrimagnetism :

Neel in 1948 gave a modification of the Weiss model of ferromagnetism. Instead of one ferromagnetic exchange field, the crystal is subdivided into two or more sublattices each possessing uniform magnetism. The molecular exchange field of the individual sublattices may have positive or negative signs and the total field will be written as,

$$H_{ex} = \sum_j \lambda_{ij} M_j \quad \dots (33)$$

The Curie temperature of a set of two sublattices a and b is obtained by solving the values of $M_a(T)$ and $M_b(T)$, as

$$T_c = \frac{1}{2} \left\{ C_a \lambda_{aa} + C_b \lambda_{bb} \pm \left[(C_a \lambda_{aa} - C_b \lambda_{bb})^2 + 4 C_a C_b \lambda_{ab}^2 \right]^{1/2} \right\} \quad \dots (34)$$

for which the positive root is to be chosen since only the higher T_c state can occur.

If $M_a = M_b$ the system is antiferromagnetic,

and $M_a \neq M_b$ the system is ferrimagnetic.

The molecular field coefficient is always negative and in ferrimagnetic case $|\lambda_{ab}|$ is much larger than either $|\lambda_{aa}|$ or $|\lambda_{bb}|$. Above the Curie point, the Brillouin function for $x \leq 1$ gives the following expression for M_a for both, antiferromagnetic and ferrimagnetic cases, as follows :

$$M_a \simeq (C_a/T) (H + H_{ap})$$

Antiferromagnetism :

$$\text{Since } M_a = M_b, M = M_a + M_b \simeq 1/2 \frac{(\lambda_{aa} + \lambda_{bb}) CHM}{T}$$

where M is the total magnetization, C = Curie-Weiss constant

$$\chi = M/H = C/(T+T_c)$$

where $C = C_a + C_b$ and the paramagnetic Curie temperature

$$T_c = 1/2 C (|\lambda_{ab}| - \lambda_{aa})$$

The dependence of $1/\chi$ versus T has been described in Fig. 12, for all three types of behaviour, namely, ferromagnetic, ferrimagnetic and antiferromagnetic in addition to the paramagnetic behaviour.

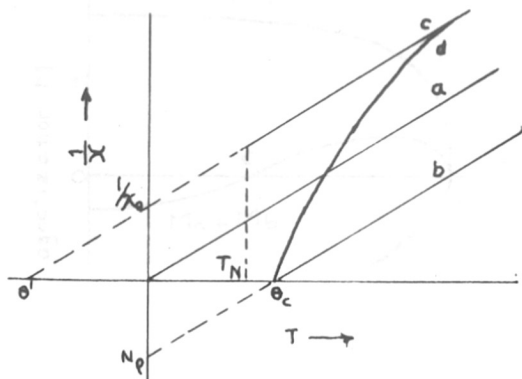


Fig. 12 : Variation of $1/\chi$ as a function of temperature in the paramagnetic region

- no interaction, paramagnetic down to 0°K
- positive interaction, ferromagnetic below $\theta = \theta_c$
- negative interaction, antiferromagnetic below T_N
- negative interaction ferrimagnetic below θ_c

The Curie temperature for an antiferromagnetic substance is called Neel temperature and is given as

$$T_N = 1/2 C (\lambda_{ab} + \lambda_{aa})$$

Measuring the temperature dependence of χ and determining T_N and T_C , one can calculate λ_{ab} and λ_{aa} from the above relationship.

Ferrimagnetism :

Macroscopically ferrimagnetism resemble ferromagnetism. A class of ferrites exemplify this kind of magnetism. For these systems $M_a \neq M_b$ and at $T = 0$ the sublattice magnetic moments will be the algebraic sum of M_a and M_b . Moreover the temperature dependence of M_a and M_b may be different and the resultant magnetization, $M = M_a + M_b$, may pass through zero as shown in Fig. 13. The point of zero magnetization is called the compensation point.

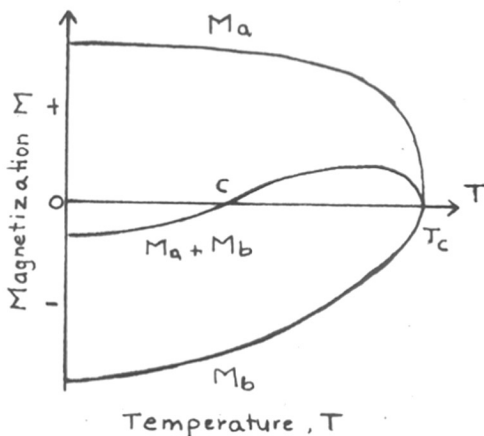


Fig. 13 : Temperature variation of the opposite sublattice magnetizations M_a and M_b
 C = Compensation temperature which lies below
 Curie temperature T_C

1.3 Preparative techniques

The basic materials to be studied are thirty years old, but what is new in this, is the novel approach to processing. For tailor-making of a material so as to cater the needs of present technology, one has to look into (i) the importance of the fine particles, (ii) the principles underlying the preparation and (iii) various approaches tried so far to prepare high-tech ceramics. Section 3 deals with these details.

1.3.1 Importance of fine particles

Generally ceramics were formulated on hit-or-miss basis but now it is based much more on scientific knowledge and theory. Key to the success is in synthesis of highly uniform, submicronic powders and improved processing of them. The production of reliable and reproducible ceramic components requires strict control on the following characteristics of the powder, namely, physical and chemical homogeneities, low impurity level, small particle size, narrow particle size distribution and freedom from agglomeration. Various aspects of the improvements in the processing technology have been reviewed by many authors [26-28]. An elegant solution to the major problems is making superfine particles all uniform in shape and size [26]. If packed in a regular array they result in an extremely uniform product, lowering down the concentration of structural flaws, ultimately suited for high technological applications.

Study of fine particles also has a lot of academic interest [27] since they have many advantages. First, fine particles provide an opportunity for the study of magnetic properties of surfaces. Second, surface area relative to volume can be varied over a relatively wide range. Third, they have only one interface. Fourth, the fine particles may be superparamagnetic, a phenomenon which depends on both the volume and the anisotropy. Fifth, the fine particle may be best suited for some measuring techniques such as the Mossbauer spectroscopy. Last, fine particles can be used in number of applications in which surface properties are important such as magnetic fluids, particulate magnetic recording media and catalysis.

1.3.2 Principles underlying the preparative techniques [15]

Proper material preparation is a combination of scientific principles and practical laboratory techniques. Following are the scientific principles which are important from this aspect.

(A) The kinetics of phase transformation within either the same compound or between different reactants depends on two physical parameters,

(a) the rate of nucleation I , given by the expression

$$I = I_0 \exp(-\Delta G/RT)$$

ΔG = free energy of nucleation, I_0 = constant related to several factors such as (i) the frequency of collisions between the molecules and surfaces, (ii) total number of molecules,

(b) the rate of growth of new phase denoted by U , also has similar exponential temperature dependence as that of l . However U is linear with time if growth proceeds at the interface and is parabolic when it is controlled by diffusion.

(B) The formation of a new compound having a particular crystal structure requires the knowledge of three chemical factors,

(a) electrostatic balance of the chemical valences must be satisfied to control the stoichiometry. Sometimes this balance is achieved by combination of high valence ions and vacancies to substitute the lower valence ion e.g. Fe^{2+} of Fe_3O_4 is balanced in this way in the structure of $\gamma\text{-Fe}_2\text{O}_3$ which can be written as $\text{Fe}_{8/3}^{3+} \square_{1/3} \text{O}_4$

(b) ionic size should be considered to control the possibilities of substitution of certain ions. Ions of similar size may easily be substituted without changing the crystal structure. In this case a different valent ion may be substituted, provided the electrostatic balance can be satisfied.

(c) Coordination preference has to be considered to study the site preferences.

1.3.3 Various preparation methods

A reliable and reproducible preparation process fulfils the following conditions :

(1) Precise control over chemical composition, stoichiometry and impurity level.

- (2) Controlled particle size.
- (3) Low calcination temperatures so as to have reactive and sinterable powder.
- (4) Applicability towards commercialization.

In light of these requirements, various conventional and nonconventional methods will be reviewed.

1.3.3.1 Conventional method

Most commonly used technique is the ceramic technique involving solid state reaction. The method involves four major steps.

In the first step, oxides or carbonates are used as common starting materials. The intimacy of the reactants is achieved by simple mechanical mixing. The mixture is then calcinated at temperatures as high as $T > 1000^{\circ}\text{C}$. Second step involves ball milling or grinding in order to reduce the particle size. Various additives such as SiO_2 , boric acid [29,30] etc. have been commonly used to prohibit the grain growth during sintering. The powder is then mixed with suitable binder and made ready for consolidation. Third step involves consolidation either in wet or dry condition, with or without application of magnetic field resulting in desired size and shape. In the fourth step, the consolidated product is sintered to have a dense and hard product which is further machined to get final shape.

Powders of particle size of the order of 1 micron can be produced by this method. Main disadvantages of this method are as follows :

- (1) Chemical heterogeneity due to inefficient mixing.
- (2) Physical heterogeneity such as lattice strains due to the ball milling [31,32].
- (3) High calcination and sintering temperatures resulting in unwanted grain growth.
- (4) Contamination from the abrasive material.

Besides the above mentioned disadvantages, the ceramic method still has firm feet in the processing technology due to its relatively simple and economical procedure, having less number of variables to be controlled.

1.3.3.2 Nonconventional methods

These methods have been described as soft chemical methods as they involve moderate conditions of processing. Most of the nonconventional methods are solution techniques, having common features described below; which are superior over the ceramic technique,

- (1) Mixing of the constituents on atomic level to achieve homogeneity and uniformity.
- (2) No mechanical milling and consequently no structural flaws and contamination from abrasive material.
- (3) Low temperatures for calcination and sintering thus avoiding the unwanted grain growth.

Various such methods are as follows

(a) Chemical coprecipitation :

The method was first tried by Economos [33] for precipitation of mixed hydroxides from their chlorides by an alkali or ammonium hydroxide. Stocker [34] prepared $Zr_xTi_{1-x}O_2$ at $750^\circ C$ in only five minutes by using this method. Pioneering work has been done by Clabaugh et al. [35] who prepared $BaTiO_3$. In this technique a solution of the desired ions usually in the form of some inorganic salts like chloride, nitrate were mixed together and precipitated simultaneously with a suitable precipitating agent. Generally it is done by introducing a stream of cations' solution into an excess of precipitating solution but sometimes, the opposite way of addition also has been practised. The coprecipitate thus formed is uniform in nature which is then filtered and washed to remove unwanted ions. It is then dried with suitable method to get a reactive powder which is further calcined. The powder is then pressed by using a binder of choice and fired at higher temperature to get a dense product. Following factors play a key role in tailor-making of a particular product and thus make the process much more intricate.

- (1) Consideration about solubility products of various components.
- (2) Effect of concentration of various reactants.
- (3) pH at which precipitation is done.
- (4) Temperature of precipitation.
- (5) Rate and method of mixing.

- (6) Effect of surfactants added during precipitation.
- (7) Washing of the excess precipitant.
- (8) Temperature and method of drying.
- (9) Temperature and rate of calcination.
- (10) Temperature and rate of sintering.
- (11) Effect of any specific atmosphere maintained during heating.
- (12) Any physical or chemical treatment given at any stage of processing.

By judicious choice and careful control of these parameters, one can get a material of desired properties. The method has been popularly used by many researchers [36-39], Haneda [40] being the first one to prepare Ba/Sr ferrite by this method. The main disadvantages of the technique are listed below.

- (1) Precipitates such as hydroxides are gelatinous and difficult to filter and wash.
- (2) Precipitation of hydroxides at different pH may lead to segregation, and there is also a fear of inhomogeneity in the bulk precipitate due to supersaturation effects.
- (3) Use of NaOH/KOH introduces alkali metal impurities which often deteriorate the properties.
- (4) Excessive washing may lead to peptisation of certain hydroxides and loss in the filtrate.

Most of the above mentioned difficulties can be overcome by rectifying some of the process parameters which will be discussed in the later chapters.

(b) Metal-organic precursor method

As early as 1951, Robin and Benard [41] carried out the decomposition of mixed oxalates of iron and cobalt in order to study iron-cobalt-oxygen system. The mixing of constituent ions on atomic scale, facilitates the occurrence and completion of the reactions such as decomposition, oxidation and reduction at reduced temperatures and shorter times. According to Yoldas [42] the term 'metal-organic' introduces the compounds having organic group along with a metal bonded via oxygen. Koppens [43] has investigated the possibility of obtaining ferrite powder by this method. Luchinni et al. [44] reported synthesis of Ba-hexaferrite by this method at 700°C in air in thirty minutes only. The particle size obtained was $<1\mu\text{m}$. Inherent weaknesses of this method are (i) low yield and (ii) association of impurities like carbon.

(c) Glass ceramic method

In this method small and strainfree crystals having desired particle size and shape are produced by controlled crystallization of an appropriate glass [45]. Shirk and Buessem [46] applied this method for $\text{BaFe}_{12}\text{O}_{19}$ and obtained it as fine particles having a single domain size, resulting in high coercive force. Oda et al. [47] report preparation of $\text{SrFe}_{12}\text{O}_{19}$ while Bahadur [48] investigated several magnetic glass-ceramics based on silicate and borate glass systems.

(d) Sol-gel method [49]

As far back as in 1941, Ferenc Korosy in Hungary used this method to produce glasses. Rustum Roy [49] pioneered the use of this technique to make finely divided and exceptionally homogeneous glasses of silica and the oxides of Al, Mg, Ti, Zr, Ge etc. The method involves the conversion of a sol (a fluid colloidal suspension of a solid in a liquid) to a gel (a semirigid colloidal dispersion of a solid in a liquid). In a typical procedure a metal is reacted with an alcohol to form a metal alkoxide, which is then dissolved in an appropriate alcohol. Then water is added to hydrolyse the alkoxide. After the adjustment of pH, the material polymerises to form a gel. The gel is then heated at 200-500°C to remove the liquid, thus converting the gel to finely divided metal oxide powder with particle size in the range 0.003-0.1 μm . Main drawbacks are (i) gelation process is very slow, (ii) facilities used are expensive and not adapted easily to small scale laboratory experiments.

(e) Liquid mix technique [50,51]

It involves following procedure :

(1) Formation of separate solutions of carbonate/nitrates/ammonium salts of the required metal ions which are then converted to a precursor using an organic polyfunctional acid, possessing at least one hydroxy and one carboxylic functional group.

(2) Slow heating of the mixture to remove the solvent is carried out carefully to get a glossy mass which is

homogeneous. Hence the composition can be easily controlled very precisely at the initial stage itself.

(3) The glass is then calcined at relatively low temperature to get the required compound giving the powder of particle size 30-5000 Å depending on the processing conditions. The main advantages are as follows. (i) Relatively simple method requiring no special apparatus, (ii) stoichiometry, purity and composition can be accurately controlled since process involves no washing.

(f) Cryochemical or freeze-dry process [52]

Basic steps are (i) preparation of water solution of constituent salts, (ii) freezing in the form of small spheres, (iii) sublimation of water vapour, (iv) decomposition of the salts to oxide.

Quick freezing provides extensive nucleation and uniform crystal growth with little segregation. Uniform heating of the solid spheres results in the narrow size distribution. The scope of application of this method is rather small, as all salts of interest are not water soluble and particles obtained are in the form of voluminous hollow shells which do not give dense mass after compaction.

(g) Vapour phase method [1]

In recent years, various scientists have explored ways to make superfine powders in the vapour phase rather than in liquid phase. They have vapourised materials by using laser beam, plasma arc and other techniques. Haggerty et al. at MIT have used CO₂ laser as a heat source to

convert gases to high purity powders of Si, SiN, SiC etc. The particles are submicronic by nature as the reactants are exposed to high temperatures only briefly so that the solid nuclei have little time to grow. In addition the powders are essentially free from agglomerates.

REFERENCES

1. H.J. Sanders,
Chemical and Engineering News, 62:28 (1984) 26.
2. R.R. Hirwani,
Chemical Business, 1:8 (1987) 45.
3. B.K. Das,
Report on Advanced Ceramics - An Perspective, Mar. 1988,
NPL (India).
4. NMAB Report on Magnetic Materials, Mar. 1985. National
Research Council, U.S.A.
5. E.C. Stoner and E.P. Wohlfarth,
Philos.Trans.R.Soc., A240 (1948) 599.
6. A.K. Jain and S.L. Sarnot,
Electronics Information and Planning, 8:4 (1982) 175.
7. N. Ichinose,
Am.Ceram.Soc.Bull., 64:12 (1985) 1581.
8. A.P.B. Sinha in "Solid State Chemistry" edited by C.N.R.
Rao (1974), Marcel Dekker, Inc., New York.
9. C.D. Sabane,
Ph.D. Thesis, University of Poona, (1960).
10. G.I. Finch, A.P.B. Sinha and K.P. Sinha,
Proc.Roy.Soc.(London), A242 (1957) 28.
11. M.N.S. Murthy, C.E. Deshpande, P.P. Bakare and
Mrs. J.J. Shrotri,
Bull.Chem.Soc.Japan, 52:2 (1979) 571.
12. D.H. Martin,
Magnetism in Solids (1967), Iliffe Books Ltd., London.
13. A.J. Dekker,
Solid State Physics, (1952), McMillan and Co.Ltd. London.
14. J.Smit and H.P.J. Wijn,
Ferrites (1959), N.V. Philips' Gloeilampenfabrieken.
15. M.M. Schieber,
Experimental Magnetochemistry (1967), North Holland
Publishing Company, Amsterdam.
16. Ing.C. Heck.
Magnetic Materials and their Applications (1974)
Butterworth and Co. (Publishers) Ltd.

17. G.T. Rado and H. Suhl,
Magnetism (1963-1966), Academic Press, New York.
18. J.B. Goodenough,
Magnetism and Chemical Bond (1963), Interscience,
New York.
19. C.P. Poole, Jr. and H.A. Farach,
The Theory of Magnetic Resonance (1972), John Wiley and
Sons Inc., New York.
20. A.S. Chakravarty,
Introduction to the magnetic Properties of Solids (1980),
A Wiley-Interscience Publication, New York.
21. J.S. Griffith,
The Theory of Transition Metal Ions (1961), Cambridge
University Press, London.
22. D. Hadfield, Permanent Magnets and Magnetism (1962),
Iliffe Books Ltd., London.
23. D.J. Craik, Magnetic Oxides (1975), John Wiley and Sons
Ltd., New York.
24. G.I. Epifnov,
Solid State Physics (1979), Mir Publishers, Moscow.
25. F.A. Cotton and G. Wilkinson,
Advanced Inorganic Chemistry (1962), Wiley Eastern
Pvt.Ltd. New Delhi.
26. D.W. Johnson Jr. and B.B. Ghate,
Advances in Ceramics, IVth Int.Conf. on Ferrites,
Part I, 15 (1986) 27.
27. A. Roosen, H. Hausner,
Adv.Ceram.Mat., 3:2 (1988) 131.
28. F.F. Lange,
J.Am.Ceram.Soc., 72:1 (1989) 3.
29. H. Harada,
Ferrites : Proc. of Int.Conf., Japan, Sept.-Oct. (1980)
354.
30. F. Haberey and F. Kools,
Ferrites : Proc. of Int.Conf., Japan, Sept.-Oct. (1980)
356.
31. R.C. Tenzer,
J.Appl.Phys., 34 (1963) 1267.
32. G. Heimke,
Z.Angew.Phys., 15 (1963) 271.

33. G. Economos,
J. Am. Ceram. Soc., 38 (1955) 241.
34. J. Stocker and R. Collongues,
Compt. Rend., 245 (1957) 431.
35. W.S. Clabaugh, E.M. Swiggard and R. Gilchrist,
J. Res. of NBS, 56 (1956) 289.
36. C.D. Mee and J.C. Jeschke,
J. Appl. Phys., 34:4 (1963) 1271.
37. P.K. Gallagher and J. Thomson, Jr.,
J. Am. Ceram. Soc., 48 (1965) 644.
38. K. Haneda and H. Kojima,
J. Appl. Phys., 44:8 (1973) 3760.
39. W. Roos,
J. Am. Ceram. Soc., 63 (1980) 601.
40. K. Haneda, C. Miyakawa and H. Kojima,
J. Am. Ceram. Soc., 57:8 (1974) 354.
41. J. Robin and J. Benard,
C.R. Acad. Sci. Paris, 232 (1951) 1830.
42. B.E. Yoldas,
J. Mater. Sci., 12 (1977) 1203.
43. L.J. Koppens,
IEEE Trans. Magn., MAG-8 (1972) 303.
44. E. Luchini, S. Meriani, F. Delben and S. Paoletti,
J. Mater. Sci., 19 (1984) 121.
45. P.W. McMillan,
Glass Ceramics (1979), Academic Press, London.
46. B.T. Shirk and W.R. Buessem,
J. Amer. Ceram. Soc., 53 (1970) 192.
47. K. Oda, T. Yoshio, K.O. Oka and F. Kanamaru,
J. Mat. Sci. Lett., 3 (1984) 1007.
48. D. Bahadur, D. Chakravorty, D. Chattopadhyay, S. Datta,
S.K. Khan, S. Mitra, S. Ram, D. Roy and K. Sengupta,
J. Mater. Sci., 21 (1986) 2793.
49. R. Roy,
J. Am. Ceram. Soc., 52[1-6] (1969) 344.
50. A. Srivastava,
Ph.D. Thesis, University of Poona, (1985).

51. C. Marcilly, P. Courty and B. Delmon,
J.Am.Ceram.Soc., 83:1 (1970) 56.
52. F.J. Schnettler, F.R. Monforte and W.W. Rhodes,
Fourth Int.Conf.on Ceramics (1967).

CHAPTER 2

EXPERIMENTAL

2.1 SYNTHESIS

2.1.1 Preparation in general

In the present work, we have selected ceramic method as the conventional route, while coprecipitation method as the nonconventional route for the synthesis of both, strontium hexaferrite ($\text{SrFe}_{12}\text{O}_{19}$) as well as copper manganite (CuMn_2O_4). Fig. 1 illustrates both these techniques with the help of a block diagram.

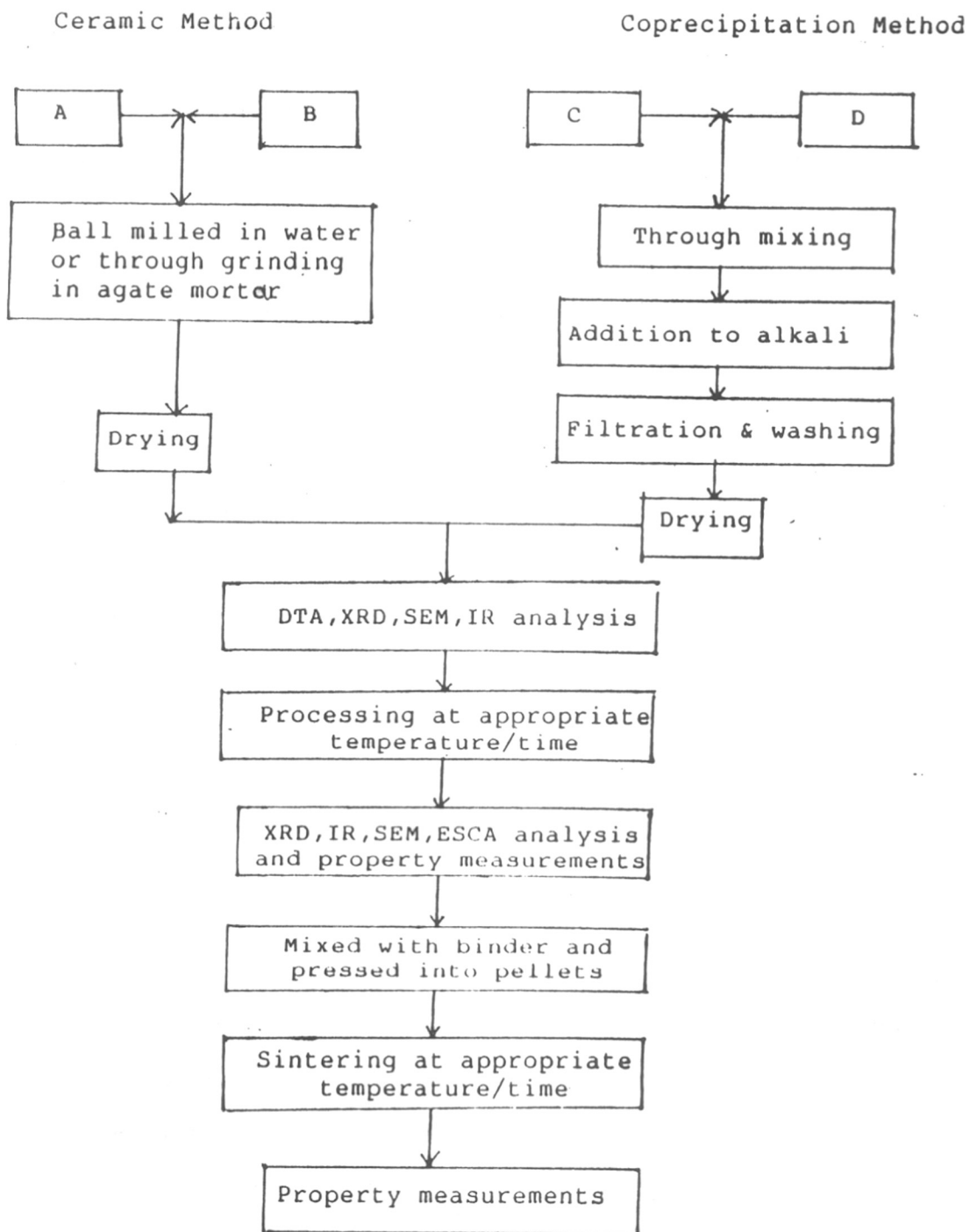
(1) For the experiments on synthesis of strontium hexaferrite, A, B represent $\alpha\text{-Fe}_2\text{O}_3$ and SrCO_3 and C, D represent solutions of $\text{FeCl}_3/\text{Fe}(\text{NO}_3)_3$ and $\text{SrCl}_2/\text{Sr}(\text{NO}_3)_2$ respectively.

(2) For the experiments on synthesis of copper manganite A, B represent CuO and Mn_2O_3 while C, D represent solutions of CuSO_4 and MnSO_4 respectively.

Chemicals used for both the preparations are as follows :

- (1) $\alpha\text{-Fe}_2\text{O}_3$ - commercial grade, NMDC, India;
 - $\text{FeCl}_3 \cdot 6\text{H}_2\text{O}$ - AR grade, SD Fine Chemicals, India;
 - $\text{FeCl}_3 \cdot 6\text{H}_2\text{O}$ - LR grade, SD Fine Chemicals, India;
 - $\text{Fe}(\text{NO}_3)_3 \cdot 9\text{H}_2\text{O}$ - LR grade, BDH, India.
- (2) SrCO_3 - commercial grade, R. Johnson, India;
 - $\text{SrCl}_2 \cdot 6\text{H}_2\text{O}$ - AR grade, Loba Chemicals, India;
 - $\text{SrCl}_2 \cdot 6\text{H}_2\text{O}$ - LR grade, Ranbaxy, India;
 - $\text{Sr}(\text{NO}_3)_2$ - LR grade SrCO_3 dissolved in HNO_3 .

Fig. 1 : Flow chart illustrating preparation methods for Sr-ferrite and Cu-manganite.



- (3) NaOH - AR grade, Loba Chemicals, India;
 NaOH - LR grade, SD Fine Chemicals, India;
 Na₂CO₃ - AR grade, SD Fine Chemicals, India.
- (4) CuO - AR grade, BDH, UK;
 CuSO₄.5H₂O - AR grade, BDH, India.
- (5) Mn₂O₃ - prepared from MnO₂ (Loba Chemicals, India) at
 850°C/5 h;
 MnSO₄.H₂O - AR grade, Loba Chemicals, India.

2.1.2 Preparation of strontium hexaferrite : Important features

(a) Ceramic method : Reactants in the oxide form were mixed in the required ratio, wet milled in a steel ball mill for two hours, and then dried in the oven at 100°C. The mixture was then calcined in powder form at proper temperature between 1250-1300°C/30 min. The calcined product was again ball milled for \approx 90 hours to reduce the particle size upto 1 μ m. At this stage boric acid (0.2% by weight of initial mixture) was added during ball milling, to prevent the grain growth [1]. After milling in the ball mill, the powder was mixed with polyvinyl alcohol (PVA, 1% by weight of the powder) which acts as a binder. Pellets were pressed using 'Carver Laboratory Press' under a pressure of 2.2 tones/cm² for one minute and further sintered at the appropriate temperature/time.

(b) Coprecipitation method : For the experiments done by this route, we followed the method given by Haneda et al .[2], with some suitable modifications. The reactants were

dissolved in distilled water so as to have required molarity. The solutions are then filtered through sintered glass funnel (G-2) to remove the undissolved matter. Solutions of chlorides/nitrates of iron and strontium were thoroughly stirred so as to have a uniform mixture. The mixture is then added, directly or dropwise with the help of a separating funnel to the solution of alkali ($\text{NaOH} + \text{Na}_2\text{CO}_3$ or NaOH only), with vigorous mechanical stirring ensuring uniform mixing of the ingredients at the atomic level. The temperature and pH at which this precipitation was done, also plays very important role in affecting the properties of the final product. We did all the experiments at room temperature between $25^\circ\text{--}35^\circ\text{C}$ and the pH was > 13 . The precipitate thus formed has to be filtered and washed till it was free from alkali. This was done with the help of centrifuge machine till the pH of the supernatant liquid was between 8-9. When the sample was prepared on 100 g batch scale, the washing was done simply by allowing the precipitate to settle down for sometime and then siphoning out the supernatant liquid. To avoid unnecessary loss of strontium during washing, the amount of water used for washing and the number of washings were kept constant for every 100 g batch. The pH of the final slurry was between 10-11. The precipitate was then dried in oven at $\approx 100^\circ\text{C}$ and further calcined at the temperature ranging between $700\text{--}950^\circ\text{C}$ for 2 to 5 hours. The samples calcined at $T \geq 900^\circ\text{C}$, became too hard to grind with the help of ordinary agate

pestle and mortar. So they were ball milled with boric acid (0.2% by weight) in order to break the lumps. The powder was then mixed with polyvinyl alcohol (PVA) as a binder and pressed into pellets using 'Carver Laboratory Press'. The pressure and time was the same as in the case of ceramic method. The pellets were sintered at appropriate temperature for the required time. It was observed that the sintering conditions have to be optimized separately for every set of experiments.

Table 1(a,b) describes the details of preparation and processing conditions for six basic samples, namely, A-1 by ceramic method and B-1 to B-5 by coprecipitation method. The history of these samples vary mainly with respect to their precipitating agent, grade of the reactants, mode of washing the precipitate etc. On these six samples rigorous experimentation was carried out in order to study the effect of various processing parameters; as described in Tables 2 and 3.

Samples A-11 to A-19 were prepared from the sample A-1 while B-11 to B-16 were prepared from B-1, B-21 to B-27 from B-2, B-311 to B-337 from B-3, B-41 to B-43 from B-4 and B-51 to B-53 from the sample B-5.

2.1.3 Preparation of copper manganite : Important features

Ceramic method : The reactants in the oxide form were mixed together and thoroughly ground in an agate mortar in

Table 1(a) : Preparation details for ceramic method
(SrFe₁₂O₁₉)

Sample No.	Chemicals	Ratio of Fe/Sr	Mixing/Grinding
A-1	α -Fe ₂ O ₃ SrCO	11.0	ball milled/ water/2h

Table 1(b) : Preparation details for coprecipitation method (SrFe₁₂O₁₉)

Sample No.	Chemicals	Precipitating agent	Fe/Sr ratio	Temperature of precipitation °C	pH	Rate of addition of mixture of Fe and Sr salts ml·min ⁻¹	Washing	Drying
B-1	AR FeCl ₃ ·6H ₂ O (2.64 M), AR SrCl ₂ ·6H ₂ O (1.2 M)	* AR NaOH + AR Na ₂ CO ₃	11.0	25-35	> 13	3-4	centrifuge/ distilled water	oven/ 100°C
B-2	LR FeCl ₃ ·6H ₂ O (2.64 M) AR SrCl ₂ ·6H ₂ O (1.2 M)	* AR NaOH + AR Na ₂ CO ₃	11.0	25-35	> 13	fast addition	centrifuge/ distilled water	oven/ 100°C
B-3	AR FeCl ₃ ·6H ₂ O (2.64 M) AR SrCl ₂ ·6H ₂ O (1.2 M)	AR NaOH (5.3 M)	10.4- 12.0	25-35	> 13	3-4	siphon/ distilled water	oven/ 100°C
B-4	LR FeCl ₃ ·6H ₂ O (2.64 M) LR SrCl ₂ ·6H ₂ O (1.2 M)	AR NaOH (5.3 M)	11.0	25-35	> 13	3-4	siphon/ distilled water	oven/ 100°C
B-5	LR Fe(NO ₃) ₃ ·9H ₂ O (2.64 M) LR Sr(NO ₃) ₂ (1.2 M)	AR NaOH (5.3 M)	10.8	25-35	> 13	3-4	siphon/ distilled water	oven/ 100°C

* For 100 g (ferrite) batch, 440 g NaOH + 110 g Na₂CO₃ in 2.5 lit. distilled water.

Table 2 : Various processing parameters for ceramic method
(samples A-11 to A-19)

Parent sample	Sample No.	Fe/Sr ratio	Dopant	Calcination temp/time °C/min ⁻¹	Binder
	A-11	12.0	-	1280/30	PVA
	A-12	11.0	-	1280/30	PVA
	A-13	10.2	-	1280/30	PVA
	A-14	11.0	-	1300/30	Lignin
A-1	A-15	11.0	-	1300/30	Hydroxy-ethyl cellulose
	A-16	11.0	-	1300/30	PVA
	A-17	11.0	Al as $Al_2(SO_4)_3 \cdot 16H_2O$	1300/30	PVA
	A-18	11.0	Co as $CoSO_4$	1300/30	PVA
	A-19	11.0	Ca as $CaSO_4$	1300/30	PVA

Table 3 : Various preparation parameters for coprecipitation method

Parent sample	Sample No.	Fe/Sr ratio	Other variables	Rate of addition of metal salts to alkali ml/min	Dopant/surfactant	Calcination temp/time °C/h	Chemical/physical treatment
B-1	B-11	11.0	-	3-4	-	750/5	-
	B-12	11.0	-	3-4	-	750/5	1:1 HCl
	B-13	11.0	-	fast addition	-	800/3	-
	B-14	11.0	-	3-4	-	800/3	-
	B-15	11.0	dilute solution*	3-4	-	750/5	-
	B-16	11.0	saturated solution**	3-4	-	750/5	-
	B-17	11.0	-	3-4	ethylene glycol	800/3	-
	B-18	11.0	-	3-4	glycerol trioleate	800/3	-
B-2	B-21	11.0	-	3-4	Al as $Al_2(SO_4)_3 \cdot 16H_2O$	925/2	ball milling/16 h
	B-22	11.0	-	3-4	Cr as $CrSO_4$	925/2	-
	B-23	11.0	-	3-4	Co as $CoSO_4$	925/2	-
	B-24	11.0	-	3-4	Bi as $(BiO)_2CO_3$	925/2	-
	B-25	11.0	-	3-4	Pb as PbO	925/2	-

Table 3 (contd.)

Parent sample	Sample No.	Fe/Sr ratio	Other variables	Rate of addition of metal salts to alkali ml/min	Dopant/surfactant	Calcination temp/time °C/h	Chemical/physical treatment
B-2	B-26	11.0	-	3-4	-	925/2	-
	B-27	11.0	-	3-4	-	925/2	ball milling/16 h/1:1 HCl
B-3	B-311	10.4	-	3-4	-	750/5	-
	B-312	10.6	-	3-4	-	750/5	-
	B-313	10.8	-	3-4	-	750/5	-
	B-314	11.0	-	3-4	-	750/5	-
	B-315	11.4	-	3-4	-	750/5	-
	B-316	11.8	-	3-4	-	750/5	-
	B-317	12.0	-	3-4	-	750/5	-
	B-321	10.4	-	3-4	-	925/2	-
	B-322	10.6	-	3-4	-	925/2	-
	B-323	10.8	-	3-4	-	925/2	-
B-324	11.0	-	3-4	-	925/2	-	
B-325	11.0	-	3-4	-	925/2	-	
B-326	11.8	-	3-4	-	925/2	-	
B-327	12.0	-	3-4	-	925/2	-	

Table 3 (contd.)

Parent sample No.	Sample No.	Fe/Sr ratio	Other variable	Rate of addition of metal salts to alkali ml/min	Dopant surfactant	Calcination temp/time	Chemical/physical treatment
						°C/h	
B-4	B-41	11.0	-	3-4	-	750/5	-
	B-42	11.0	-	3-4	-	925/2	-
	B-43	11.0	-	3-4	-	925/2	1:1 HCl

B-5	B-51	10.8	-	3-4	-	750/5	-
	B-52	10.8	-	3-4	-	925/2	-
	B-53	10.8	minimum pH variation	3-4	-	750/5	-

* $\text{FeCl}_3 \cdot 6\text{H}_2\text{O}$ (0.825 M), $\text{SrCl}_2 \cdot 6\text{H}_2\text{O}$ (0.375 M),

NaOH (440 g) + Na_2CO_3 (110 g) in 3.52 lit. dist. water
(for 100 g ferrite batch).

** $\text{FeCl}_3 \cdot 6\text{H}_2\text{O}$ (2.6 M), $\text{SrCl}_2 \cdot 6\text{H}_2\text{O}$ (1.2 M)

NaOH (440 g) + Na_2CO_3 (110 g) in 2.5 lit. dist. water
(for 100 g ferrite batch).

alcohol/acetone; so as to have a uniform mixture. The mixture is then dried and heated/calced in a silica tube furnace at various temperatures in the range 600-950°C. Homogeneity of the mixture was achieved by taking the sample out of the furnace and regrinding it intermitantly during the heating cycle. The formation of the manganite phase was checked by X-ray diffractograms of the polycrystalline samples.

Coprecipitation method : Solutions of sulphates of copper and manganese were prepared in distilled water. Stoichiometric amounts of the reactants i.e. Cu and Mn sulphates were then mixed together in a solution form. This mixture was then added dropwise (\approx 400-500 c.c. of the mixture per minute) to NaOH solution with vigorous mechanical stirring. Bluish gray coloured precipitate was obtained which turned black on exposure to atmosphere. The precipitate thus formed was filtered through sintered glass funnel (G-4) and washed with distilled water till free from SO_4^{--} and OH^- ions. The first filtrate was tested for the presence of Cu^{2+} and Mn^{3+} ions. The tests were negative indicating the completion of precipitation. The pH of the final solution was between 11 to 11.5. The precipitate was then dried at room temperature under vacuum. The coprecipitate was then calcined at various temperatures/time in the range 200-950°C in a silica tube furnace. Tables 4 and 5 give the details of preparation of copper manganite by both the methods.

Table 4 : Preparation details for ceramic method
(CuMn_2O_4)

Sample No.	Reactants	Ratio of Cu:Mn	Calcination conditions °C/h
C-1	CuO and Mn_2O_3	1:2	(1) 600/24
			(2) 700/24
			(3) 750/24
			(4) 800/24
			(5) 750/120+850/24
			(6) 750/120+850/24+880/24
			(7) 750/120+850/24+880/24+950/24

Table 5 : Preparation details for coprecipitation method (CuMn_2O_4)

Sample No.	Chemicals	Ratio of Cu:Mn	pH of final solution	Temperature of precipitation	Rate of Addition	Filteration and washing	Drying	Calcination conditions
D-1	CuSO_4 (0.025 M) MnSO_4 (0.017 M) NaOH (0.03 M)	1:2	11.0 to 11.5	Room temp. between 25-30 C	400-500 cc of mixture of Cu+Mn sulphates per min.	On sintered glass funnel G-4	at RT in vacuum	Various temperatures between 200 - 950°C with a step of 100°C

2.2 CHARACTERIZATION TECHNIQUES

As described in Fig. 1., the samples were characterized at different stages of the synthesis, with the help of the following techniques.

(1) Thermal analysis, DTA/DTG/TG : A Netzsch STA 409 differential thermal analyser was used to locate the reaction temperatures, energy changes and weight changes taking place in the sample during heating. A calibrated Pt/Pt-10 to Rh thermocouple was used for sensing the temperature accurately. The samples were heated in dynamic air, at the heating rate of $10^{\circ}\text{C min}^{-1}$ and a chart speed of 120 mm h^{-1} during the full scan ($20\text{--}1400^{\circ}\text{C}$). Three types of thermal scans were taken.

(a) A normal DTA/DTG/TG scan for samples A-1, B-1 to B-5.

(b) DTA/DTG/TG scans for the coprecipitate with various heating rates between $2^{\circ}\text{C min}^{-1}$ and $50^{\circ}\text{C min}^{-1}$ for sample B-4.

(c) An isothermal DTA scan for sample A-1.

(2) X-ray diffraction (XRD) analysis : A Philips PW 1730 X-ray diffractometer using $\text{Cu-K}\alpha$ radiation ($\lambda = 1.542 \text{ \AA}$) was used to record the powder spectra of the samples prepared by the two techniques. Different phases in a sample were identified by comparing a set of 'd' values and the corresponding intensities with the standards from ASTM data file.

(3) Infrared (IR) analysis : IR spectra of the samples were recorded in Nujol on a Pye-Unicam IR Spectrometer (SP3-300).

(4) Scanning electron microscopic (SEM) analysis : Microstructural studies were made with a Cambridge Stereoscan 150

Scanning Electron Microscope. The particle size and its distribution and the morphology of the samples, prepared by both the methods were studied.

(5) Mossbauer spectroscopic analysis : Fe^{57} Mossbauer spectra were recorded for ferrite samples with a conventional constant acceleration electromechanical drive, coupled to ND 100 multichannel analyser operating in time mode. A 10 mCi Rh : Co^{57} source was used to record the spectra at room temperature.

(6) Electron spectroscopy for chemical analysis (ESCA) : In case of copper manganite samples, the oxidation states of various species present on the surface have been identified with the help of X-ray photoelectron spectroscopy on VG Scientific ESCA-3 Mark II Spectrometer using Al K_{α} and Mg K_{α} radiation.

(7) Low angle XRD analysis : Copper manganite samples were characterised by small angle X-ray diffraction measurements performed on Rigaku machine, (mode Rotaflex RV 200B) using Cu K_{α} radiation.

(8) Magnetic measurements : To measure various magnetic parameters, hysteresis loops were traced with the help of Walker Scientific Inc., USA model No. MH-1020. Various parameters such as remanence (B_r), coercivity (H_c), intrinsic coercivity (iH_c), maximum energy product $(BH)_{\max}$ etc. have been computed from hysteresis loop.

REFERENCES

1. H. Harada,
Ferrites : Proc.Int.Conf., Japan (1980), 354.
2. K. Haneda, C. Miyakawa and H. Kojima,
J.Am.Ceram.Soc., 57:8 (1974) 354.

CHAPTER 3

STRONTIUM HEXAFERRITE

Generally, ferrites are classified as hard ferrites (difficult to magnetize and demagnetize) and soft ferrites (easy to magnetize and demagnetize). Among the hard ferrites Ba/Sr based magnets having magnetoplumbite structure are of specific importance due to their superior magnetic properties. Chapter 3 gives elaborate discussion on strontium hexaferrite ($\text{SrFe}_{12}\text{O}_{19}$) in terms of its x-ray and magnetic structure, its working as permanent magnet and the results and discussion on the present work.

3.1 INTRODUCTION

3.1.1 X-Ray and magnetic structure of M-type hexagonal ferrites

A class of ferrites having composition $\text{MO.6Fe}_2\text{O}_3$ with magnetoplumbite structure is known as M-type hexagonal ferrites. The term magnetoplumbite was coined by a group of Swedish investigators [1,2] particularly Adelskold who was the first one to identify the crystal structure of these ferrites correctly. Obradors [3] gave an accurate analysis of the crystal structure of strontium hexaferrite which is isomorphous with the magnetoplumbite structure.

Magnetoplumbite structure : The unit cell is hexagonal and contains two molecules of $\text{Me}_2\text{Fe}_{12}\text{O}_{19}$ ($\text{Me} = \text{Ba}^{2+}/\text{Sr}^{2+}/\text{Pb}^{2+}$). Fig. 1 describes the structure in terms of two blocks namely R and S blocks. The S block is a spinel block with its cubic $\langle 111 \rangle$ axis oriented parallel to the C axis of the hexagonal cell. One such block consists of two oxygen layers, each layer containing four oxygen ions. The corresponding six Fe^{3+} ions are distributed over two tetrahedral and four

octahedral sites. The R block is made up of three oxygen layers. The two terminal layers contain four oxygen ions each, while the central layer has three oxygen ions and one Me ion. In this block five metal ions are at octahedral site and one is at trigonal bipyramidal site. The complete unit cell is built up of alternate stacking of R and S units in the sequence R S R* S* where * indicates that these blocks are rotated by 180° around the C axis with respect to the R and S blocks. The unit cell thus contains the four oxygen layers with the Me ion replacing an O^{2-} ion every fifth layer.

Magnetic structure : The model for the magnetic structure was first suggested by Gorter [4] from the application of the Kramers-Anderson indirect exchange theory. All the magnetic moments are aligned along the hexagonal C axis, according to the scheme given in Table 1 [5,6]. The distribution of Fe^{3+} ions and their spin orientations are depicted in Fig. 2. The net magnetic moment is $4 \times 5 \mu_B = 20 \mu_B$, per formula unit. Exchange interactions amongst the ferric ions occupying different lattice positions arise from the superexchange mechanism for all intersublattice and intrasublattice, except the Fe 4 intrasublattice interaction where, besides the superexchange, some direct exchange contributions also exist [3,4,7].

3.1.2 Working of a permanent magnet

Hysteresis loop gives an elegant perspective of working of a permanent magnet. If one plots a graph of

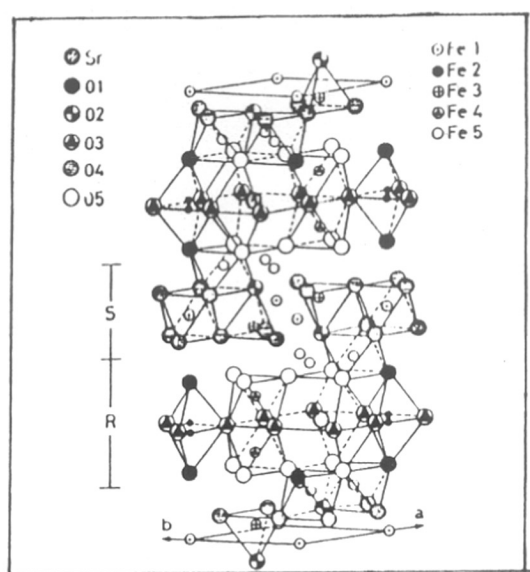


FIG.1: Crystallographic structure $\text{SrFe}_{12}\text{O}_{19}$ [3]

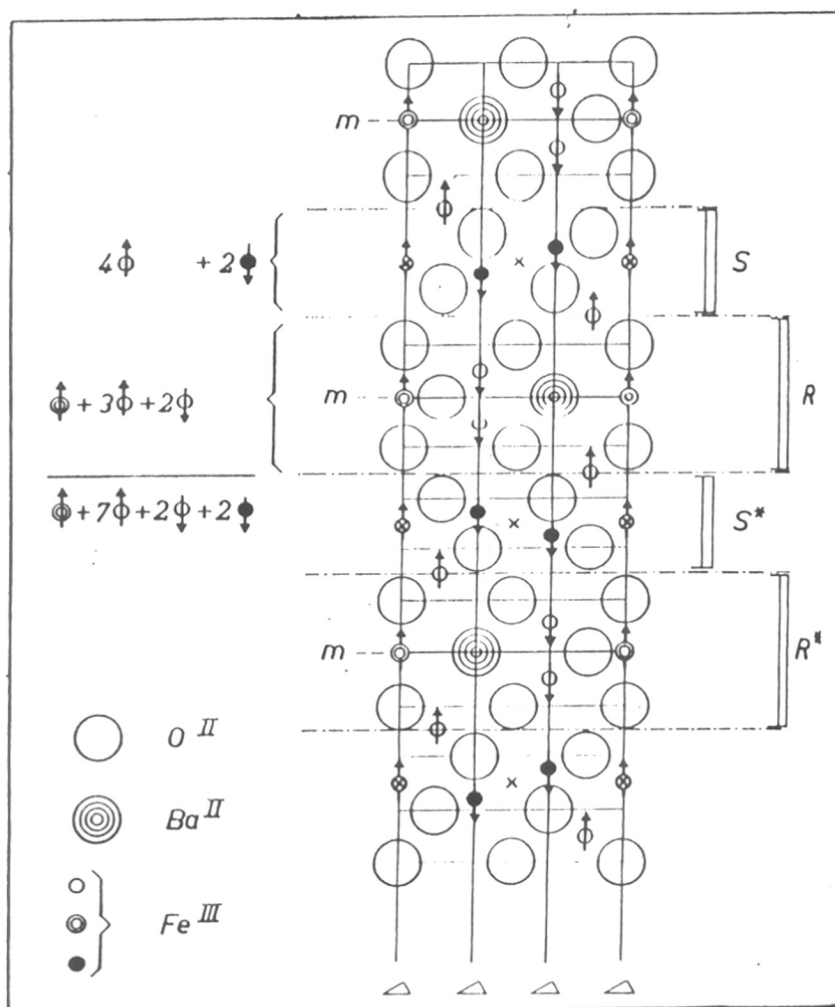


FIG.2: Cross section of the magnetoplumbite structure M.

The arrows indicate the spin orientations [44]

Table 1 : Crystallographic and magnetic characteristics of various Fe^{3+} ions in M type structure

Fe^{3+} ion	Coordination	Block	Spin	Number of ions per formula unit	Sublattice position
Fe 1	octahedral	S	↑	1	2a
Fe 2	five fold	R	↑	1	2b or 4e (1/2)
Fe 3	tetrahedral	S	↓	2	4f ₁
Fe 4	octahedral	R	↓	2	4f ₂
Fe 5	octahedral	S	↑	6	12 k

magnetic induction B versus the applied magnetic field H , one obtains a characteristic curve resembling a thick S, known as hysteresis loop; shown in Fig. 3. The curve OABC represents the magnetization of a virgin specimen. As H increases, B increases and if at point C, H is reversed B decreases to a nonzero value B_r called as remanence. Field $H = H_c$ in the negative direction, called as coercivity, is required to make B equal to zero. Similar plot is obtained for magnetisation M versus applied field H . Field required to bring M to zero is known as the intrinsic coercivity iH_c . The plot of B versus H is of special technical importance, since B includes M as well as H , and is more directly related to the performance of many electrical devices. The working point of a magnet lies in the second quadrant. Each point in the loop represents some value of B times H . The maximum of this value is known as $(BH)_{max}$. It is the index of quality of the permanent magnet. For a good magnet high B_r , high H_c and high fullness factor $\{(BH)_{max}/B_r H_c\}$ are required. $(BH)_{max}$ can be expressed as [8]

$$(BH)_{max} = (4 \pi M_s)^2 A^2 P^2 / 4 \quad \dots (1)$$

where A = alignment factor, P = packing density, M_s = saturation magnetization.

Magnetocrystalline anisotropy : It is found that in the absence of the applied magnetic field, the magnetization vector tends to align parallel to a certain preferred direction. This results from the coupling between the electron spin momentum and the orbital angular momentum.

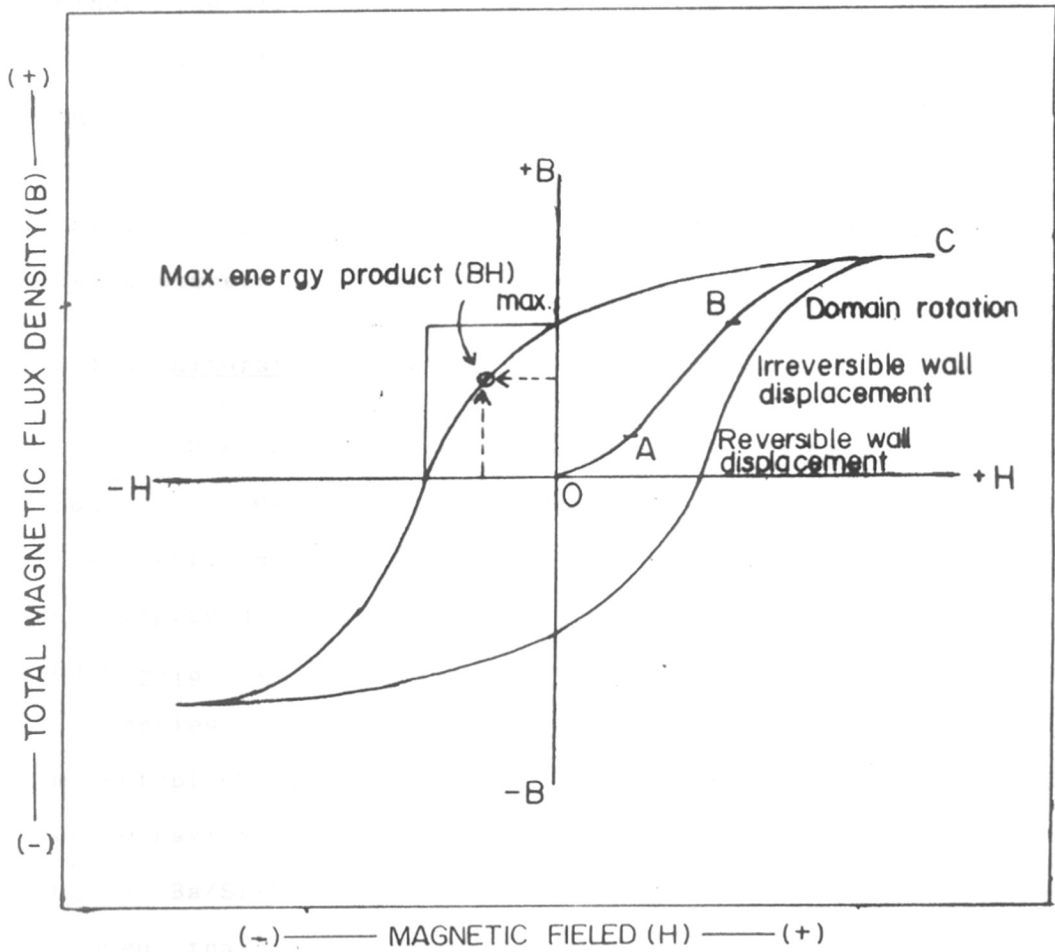


FIG.3 : Hysteresis loop of a permanent magnet. OABC is typical magnetisation curve of a virgin specimen, indicating the predominant processes taking place in the different regions [45]

Since the directional properties of the orbitals are highly oriented with respect to the crystal lattice, the effect of the applied magnetic field on the spin moments, depends on the spin orientations with respect to the crystalline lattice. The anisotropy constants depend strongly on the temperature.

3.1.3 Literature survey

Use of ferrites as permanent magnet, was first reported by Kota and Takei [9], but it was only in 1952 that the ferrites became technically popular when their $(BH)_{\max}$ was improved to 1 MGOe. From 1962 onwards $\text{SrFe}_{12}\text{O}_{19}$ replaced $\text{BaFe}_{12}\text{O}_{19}$ in many applications due to their superior properties [10,11]. Some 20,000 different anisotropic magnetoplumbite magnets have been prepared with a principal phase having composition $(\text{M}_1\text{O})_{1-x} (\text{M}_2\text{O})_x : n \text{Fe}_2\text{O}_3$ where $\text{M}_1, \text{M}_2 = \text{Ba/Sr/Pb or Ca}$ and n was between 3 and 8. The data showed that the highest values were all obtained for strontium ferrite based magnets as shown in Fig. 4. Approximately 30% higher iH_c values at the same level of remanence were explained on the basis of higher anisotropy constant K . When relation $iH_c = 2K/M_s$ is used then the coercive force of $\text{SrFe}_{12}\text{O}_{19}$ should be higher than that of $\text{BaFe}_{12}\text{O}_{19}$. Various properties of Ba and Sr ferrite are listed in Table 2.

Table 3 gives the standard data for d lines obtained for a commercial grade $\text{SrFe}_{12}\text{O}_{19}$ (Polymag, USA). More

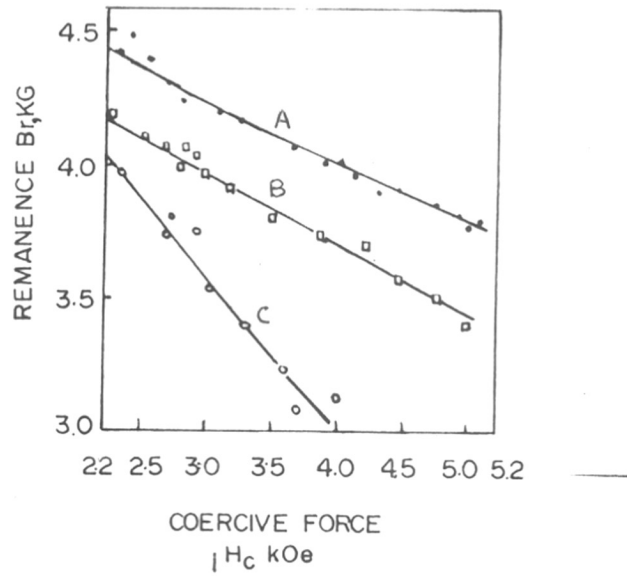


FIG. 4 : Summary of loop tests on strontium ferrite base (curve A), barium-ferrite -base (curve B) and lead-ferrite -base (curve C) magnets

Table 2 : Various properties of Ba/Sr ferrite

		*	*	*	*	*	*	*	*	*	*
	Ionic radius of Ba and Sr A^0	Anisotropy constant K_1 at 300 K erg/cm^3	Curie temp. T_C K	Bohr magneton number $N\beta$	Spontaneous magnetization at absolute zero, $M_S(0)$, G	X-Ray densities g/cm^3	Lattice parameters c a A^b A^c	Anisotropy field 2K/Ms Oe	Radius of single domain particle r_c , μm		
Ba-ferrite	1.61	3.25×10^6	740	19.3	515	5.28	23.18 5.889	16,000	≈ 1		
Sr-ferrite	1.44	3.57×10^6	750	19.7	525	5.21	23.03 5.864	-	≈ 1		
Reference	3	11	11	11	11	11	57 57	57	57		

* Single crystal data.

Table 3 : X-Ray data for a commercial grade $\text{SrFe}_{12}\text{O}_{19}$ (Polymag, USA), compared with that given in Ref. 12
 S = strong, MS = medium strong, W = weak,
 MW = medium weak, VW = very weak.

hkl	d	$d^{[12]}$	I/I ₀
006	3.8300	3.86	MW
105	3.0660	—	W
110	2.9378	2.94	MS
008	2.8823	2.89	MS
112	2.8464	2.85	VW
107	2.7608	2.77	S
114	2.6195	2.62	S
200	2.5471	2.55	MW
108	2.5265	2.52	MW
203	2.4149	2.42	MS
205	2.2254	2.23	MS
206	2.1204	2.13	MW

accurate structural analysis of strontium hexaferrite has been done by Obradors [3]. He discussed the consequences of the structural modifications observed in the case of $\text{SrFe}_{12}\text{O}_{19}$ compared to $\text{BaFe}_{12}\text{O}_{19}$ on the magnetic and crystallographic properties.

Fe^{57} Mossbauer spectroscopy has been used to determine the degree of orientation and magnetic hyperfine fields in $\text{SrFe}_{12}\text{O}_{19}$ ceramic compact. Evans et al. [13] gives the assignment of the spectrum to the different sites with the corresponding hyperfine fields. Compared to the simple spinel ferrites, the bulk spontaneous magnetization of M-type ferrites exhibit an unusually large negative temperature coefficient, which places significant limitations on their applications. Therefore an understanding of how it is related to the sublattice magnetizations and hyperfine fields is desirable. In the case of substituted ferrites, the site occupancies can be determined by either saturation magnetization measurements [14] or Mossbauer spectroscopy [15]. Kreber and Gonser [16] studied the Mossbauer spectrum of arsenic and antimony substituted ferrite and found that As/Sb ions occupy preferentially the bipyramidal lattice site. Pankhurst et al. [5] found that cobalt and titanium appear to preferentially occupy sites 12 k, 4f₂ and 2b in the R block of M type ferrite. In barium ferrite 12 k and 2b sublattice Fe^{3+} ions are known to have major contribution to the overall uniaxial anisotropy. Therefore substitutions at these sites generally reduce the coercivity

in case of $\text{BaFe}_{12-2x}\text{Co}_x\text{Ti}_x\text{O}_{19}$. Turilli [17] found similar effects in the case of Mn-Ti substituted $\text{BaFe}_{12}\text{O}_{19}$ accompanying by large perturbation to the collinear magnetic order particularly in the regions of 12 k sublattice. Such disruptions to the magnetic order would also contribute to a reduced coercivity.

Study of bulk magnetic properties and their temperature dependence was carried out by many researchers [18,19]. Shirk and Buessem [11] studied the dependence of spontaneous magnetization M_s , anisotropy field H_a , anisotropy constant K_1 , intrinsic coercive force iH_c , against temperature. Electrical properties such as seebeck coefficient [20], electrical conductivity [21], activation energy [22] etc. also have been studied.

It is well established that the magnetic properties are altered by selective additives. In case of $\text{SrAl}_x\text{Fe}_{12-x}\text{O}_{19}$, transition from M structure to W structure has been observed by Esper [23] with increasing x. Al is known to increase the iH_c upto 11,000 Oe [24]. Addition of B_2O_3 has increased the magnetization σ_s upto 77 emu/g compared to $\sigma_s = 68.5$ emu/g for pure $\text{BaFe}_{12}\text{O}_{19}$ [25] at the same time decreasing the coercive force due to the increase in particle size. Addition of La^{3+} increased the coercive force for an optimized composition of $\text{Ba}_{0.85}\text{La}_{0.15}\text{Fe}_{12}\text{O}_{19}$ [26]. Variation of σ_s , K_1 with the substitution of Co^{2+} and Ti^{4+} have been studied by Chou et al. [27]. Haneda et al. [28] observed that Al

increased the anisotropy field H_a and consequently iH_c , while Cr and Ca also increased iH_c . SrO_2 plays a role in grain growth inhibition [29]. Effect of number of impurity ions on ϵ , B_r , H_c etc. of a sintered polycrystalline $BaFe_{12}O_{19}$ and sodium lanthanum ferrite has been studied by Sinha [30].

The phenomenon of magnetization reversal has been extensively dealt with by Hempel, Roos and Haneda. ^[36-38] Stoner and Wohlfarth [31] calculated the theoretical intrinsic coercivity for an unoriented assembly of noninteracting uniaxial single domain particles in which magnetization reversal occurred through uniform rotation (rotation in unison). However the theoretical value of iH_c for $BaFe_{12}O_{19}$ far exceeds the experimental value. Several reasons [32-36] are attributed to this phenomenon, one being the presence of large grains ($>1 \mu m$) which reduce the iH_c by domain nucleation and from reverse domain nucleation at the sites of imperfections. Roos [37] observed that demagnetization curve of $BaFe_{12}O_{19}$ was determined by nucleation. Domain wall motion has not been observed. Grohs and Hempel [38] showed that in the case of magnetically diluted samples prepared by coprecipitation method, (particle size $< 0.2 \mu m$), magnetization reversal can be nearly perfectly by coherent rotation of the magnetization vector.

For the isotropic samples the $(BH)_{max}$ was only $\approx 15\%$ of the estimated maximum for the 100% (001) particle orientation [39], but in 1954 powders were pressed in a

magnetic field, orienting the individual crystallites and increasing the energy product by a factor of four [40], Saito [41] has shown that, orientation without magnetic field is possible. He called it as the magnetic field free processing of ferrites. He studied (a) the effect of the organic binder on the degree of orientation in a green compact and (b) the change of this degree during sintering. Another method to make anisotropic magnet is the hot pressing method [42].

To improve the magnetic properties of an isotropic ferrite, there is no alternative but to have ultrafine, uniform and monosized particles. If ferromagnetic particles are made small enough, there would be no room for domain boundaries. Coercive force might be very high because reversal of magnetization would have to take place by rotation of magnetization of the entire particle, which would be more difficult than the displacement of domain boundaries. Ideally the particle should be elongated one, to make rotation still more difficult. The expression for the critical radius for the single domain particle is as follows [43];

$$r_c = \frac{9 \times \sigma_w}{4\pi I_s^2} \quad \dots (2)$$

where σ_w = surface energy per unit area, I_s = magnetic saturation moment. The expression for iH_C is as follows :

$$iH_C = 0.48 (2k/M_s - 4 M_s) - 1.7 p \times M_s \quad \dots (3)$$

where k = anisotropy constant and p = volumetric packing

factor.

This radius r_c is 10% larger for strontium ferrite than for barium ferrite. The larger particle size means less size reduction, fast wet pressing, less pore volume, wider sintering range etc. for strontium ferrite than for barium ferrite [10].

In the present work, chemical coprecipitation method has been adopted, in order to reduce to particle size. Section 3.2 discusses about the consequences of the precipitation method in terms of the reduction in particle size and improvement in magnetic properties.

3.2 RESULTS AND DISCUSSION

This section discusses the outcome of the experimental work done on both the methods, namely, ceramic and coprecipitation, so as to highlight some of their inherent features. From the extensive work and its subsequent analysis through various characterization techniques, important processing parameters have been identified. These parameters are, quality of the starting raw materials, their concentration, choice of the precipitating agent, rate and method of addition, ratio of Fe to Sr, pH of the final solution, temperature of precipitation, mode of filtration and washing of the precipitate, temperature of drying, addition of dopants, surfactants, any physical/chemical treatment given at any stage, temperature/time of calcination

and sintering, rate of heating, etc. Judicious choice and careful control of these parameters resulted in improving the properties of isotropic $\text{SrFe}_{12}\text{O}_{19}$. Table 4 gives the magnetic properties of Ba/Sr ferrite obtained in various other laboratories [25, 46-49] while Table 5 is the manifestation of the results of a series of well documented experiments, done in order to have a ferrite with the desired properties. A few typical experimental runs culminating in good properties have been rigorously analysed with the help of the instrumental methods and are discussed later. History of these six representative samples namely A-1, B-1, B-2, B-3, B-4 and B-5 and their subsamples may be referred to in the Chapter 2.

3.2.1 Thermochemical studies

Thermal studies were carried out to understand the ferritization reaction leading to the formation of hexagonal strontium ferrite. DTA/DTG/TG measurements were done on the samples A-1 and B-1 to B-5.

Ceramic method : For the sample A-1 which is the mixture of $\alpha\text{-Fe}_2\text{O}_3$ and SrCO_3 , TG (Fig. 5) shows a continuous slow rise upto 640°C due to the buoyancy effect and may be considered to be negligible. The main decomposition starts from 710°C onwards upto 1070°C which is evident from the two small peaks in DTG at 810° and 970°C with a total weight loss of 3.11%. Phase change of SrCO_3 and its decomposition in air are known to overlap each other with an endothermic energy change [50]. The weight loss starts at $\approx 860^\circ\text{C}$. But in our case, such a

Table 4 : Summary of magnetic properties of Ba/Sr ferrite reported so far

Processing condition	B _r G	H _c Oe	H _c Oe	(BH) _{max} MGDe	D g/cm	σ emu/g	Reference
Sintered	2200-	1500-	2100-	1.05-	4.60-	54.0-	[25,46-49]
	3000	2200	4000	1.70	5.00	77.0	

Table 5 : Summary of magnetic properties of various samples prepared by ceramic and coprecipitation methods

Method	Processing condition	Br G	H _c Oe	iH _c Oe	(BH) _{max} MGOe	D ₃ g/cm ³	σ emu/g
Ceramic	green	1400	700	1000	0.28	3.20	52.0
	sintered	1900- 2400	1000- 1800	1700- 3400	0.60- 1.14	4.30- 4.80	42.0- 55.0
Coprecipitation	green	750- 1300	600- 1000	4000- 6750	0.10 0.30	-	-
	sintered	2200- 3300	1100- 2000	1500- 4300	1.10- 1.60	4.30- 4.69	44.0 71.0

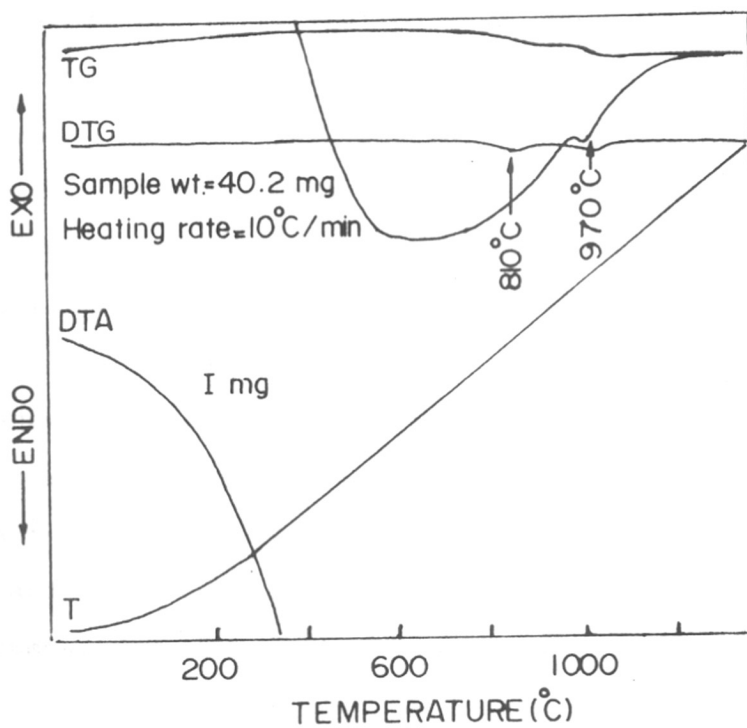


FIG.5: Simultaneous DTA/DTG/TG curves (Sample A-1)

sharp energy change was not observed in the presence of Fe_2O_3 . Instead, the DTA curve shows a broad endotherm upto 1200°C with a small hump at $\approx 960^\circ$. No energy change is observed in the temperature range $1000\text{-}1380^\circ\text{C}$.

In the case of ceramic powders, the rate of reaction may be slow due to the larger and less active particles. In which case the energy change associated with the chemical reaction such as ferritization can be detected if the reaction is carried out for longer time at appropriate temperature. To study this possibility, an isothermal scan was recorded at 900°C on 48.8 mg of the sample A-1, for 6 hours. However no energy change was detected.

Coprecipitation method : Thermochemical studies were carried out on the samples B-1, B-2, B-3, B-4 and B-5. All of them show a large endotherm at $\approx 100^\circ\text{C}$ due to the loss of the water molecules and an exothermic change occurs around 700°C . A typical DTA/DTG/TG graph of sample B-4 is shown in Fig. 6 and is discussed in details in the next paragraph. Table 6 summarizes the results of all the five samples.

Table 6

Sample number	Weight of sample g	Heating rate $^\circ\text{C}/\text{min}$	Exothermic peak temp. $^\circ\text{C}$	Peak temp. $^\circ\text{C}$
B-1	47.15	10	680-770	705
B-2	49.05	10	683-770	712
B-3	40.00	10	669-768	722
B-4	100.00	10	659-763	730
B-5	49.90	10	683-757	712

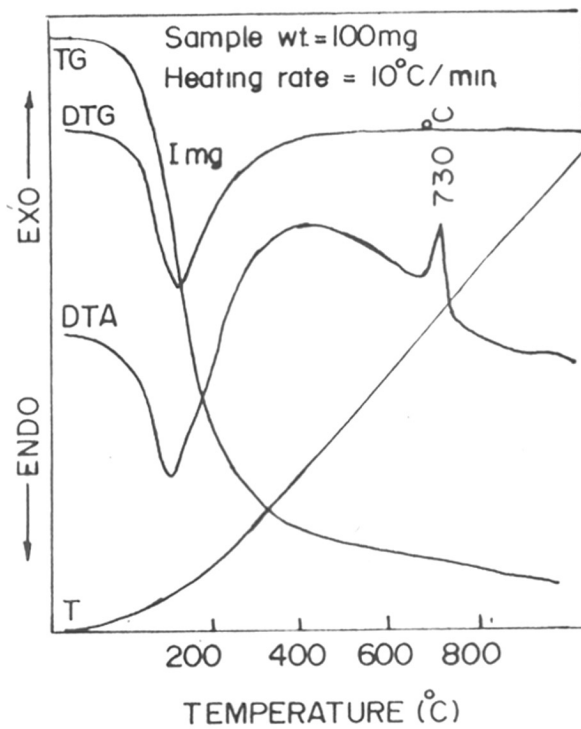


FIG.6 : Simultaneous DTA/DTG/TG curves
for sample B-4

Sample B-4 has a weight loss of $\approx 16.4\%$ upto 568°C due to the loss of water molecules. Corresponding to this loss, the DTA plot shows an endothermic peak at 126°C . With the increase in temperature, an exothermic peak appears at 730°C indicating some chemical change; leading to the ferrite formation. Table 7 summarizes the thermal decomposition data for the samples A-1 and B-4.

In order to calculate the activation energy of the ferritization reaction, DTA scans of 100 mg of the sample B-4 were taken at various heating rates, namely, 2, 5, 10, 20 and $50^{\circ}\text{C Min}^{-1}$. As the heating rate was increased the exothermic peak appeared on higher temperature side. Fig. 7 shows the plot of logarithm of the heating rate against the inverse peak temperature. To calculate the activation energy the following equation is used [51].

$$\log_{10}h = -[(E/4.57) \times 1/T_m] + \text{constant}$$

where E is the activation energy, h is the heating rate and T_m is the peak temperature. From the slope of the straight line, the activation energy was calculated to be $43.873 \text{ kcal mole}^{-1}$.

3.2.2 X-ray diffraction studies

Detection of various phases at different stages of preparation for both the ceramic as well as the coprecipitation method is done with the help of the powder X-ray diffractograms.

Table 7 : Thermal decomposition data for ceramic and coprecipitation methods

Method	DTA		DTG		TG % wt. loss	Associated change
	Peak temp. °C	Temp. range °C	Peak temp. °C	Temp. range °C		
Ceramic (A-1)			810	710- 910	3.11	decomp. of SrCO ₃
	960	910- 990	970	910- 990		
Coprecipitation (B-4)	126	RT- 450	126	RT- 568	16.40	loss of H ₂ O
	730	660- 763				ferritiza- tion reaction

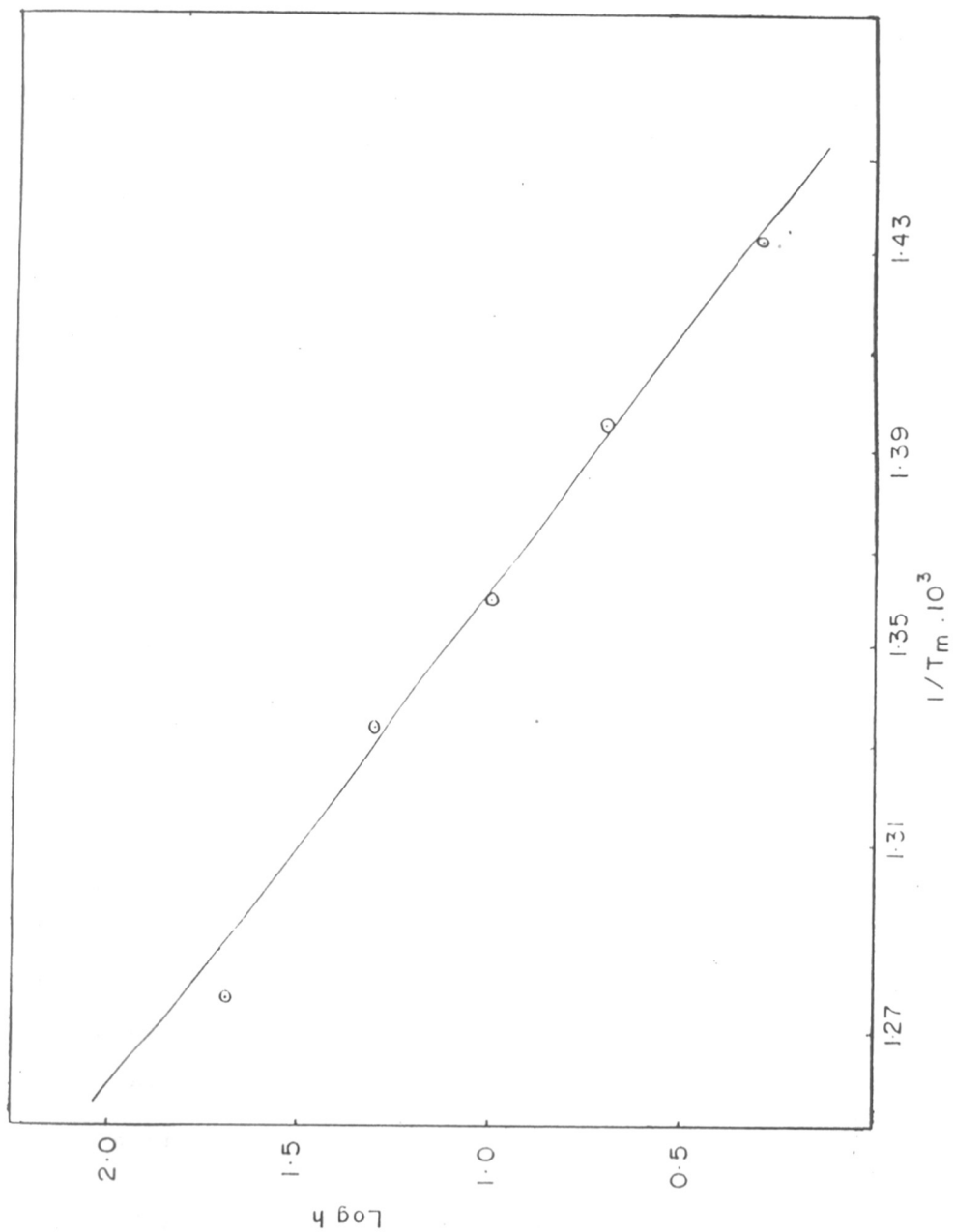


FIG.7: Plot of $\log_{10} h$ v/s $1/T_m$ (The values of T_m are read on DTA curves recorded at diff. heating rates h) for the coprecipitated sample.

Ceramic method : Sample A-1 : The physical mixture of α - Fe_2O_3 and SrCO_3 was heated in air at various temperatures, ranging from 600-1300 $^{\circ}\text{C}$ for 5 hours, with a step of 100 $^{\circ}\text{C}$ and cooled to room temperature. Fig. 8 depicts the change in the XRD patterns of the reactants with the increase in temperature. It clearly exhibits strontium hexaferrite peaks at around 900 $^{\circ}\text{C}$ along with the peaks of the unreacted compounds; α - Fe_2O_3 being identified by the corresponding diffraction lines while strontium carbonate and/or oxide is not evident owing to its low concentration. A small amount of SrFe_2O_4 spinel phase is also observed at 900 $^{\circ}\text{C}$ which decreases with increasing temperature and finally a single phase strontium hexaferrite is formed at 1300 $^{\circ}\text{C}$. The XRD lines match well with the reported values, given in Table 3.

Coprecipitation method : Sample B-1 : Fig. 9 shows the XRD of the coprecipitate which indicates the sample to be more or less amorphous in nature with a few peaks of SrCO_3 . When heated at 730 $^{\circ}/2$ h, strontium hexaferrite peaks are seen along with those of unreacted oxides. Small peak corresponding to SrFe_2O_4 is also present; which decreases as the calcination temperature is increased. The unreacted oxides exist even after heating at 750 $^{\circ}/5$ h, but the main phase is $\text{SrFe}_{12}\text{O}_{19}$.

Sample B-2 : The X-ray diffraction pattern of the plain coprecipitate as shown in Fig. 10 clearly indicates peaks of SrCO_3 and α - $\text{Fe}_2\text{O}_3 \cdot \text{H}_2\text{O}$; but the pattern is not well defined. When heated at 650 $^{\circ}\text{C}$ for 15 minutes, the pattern indicates

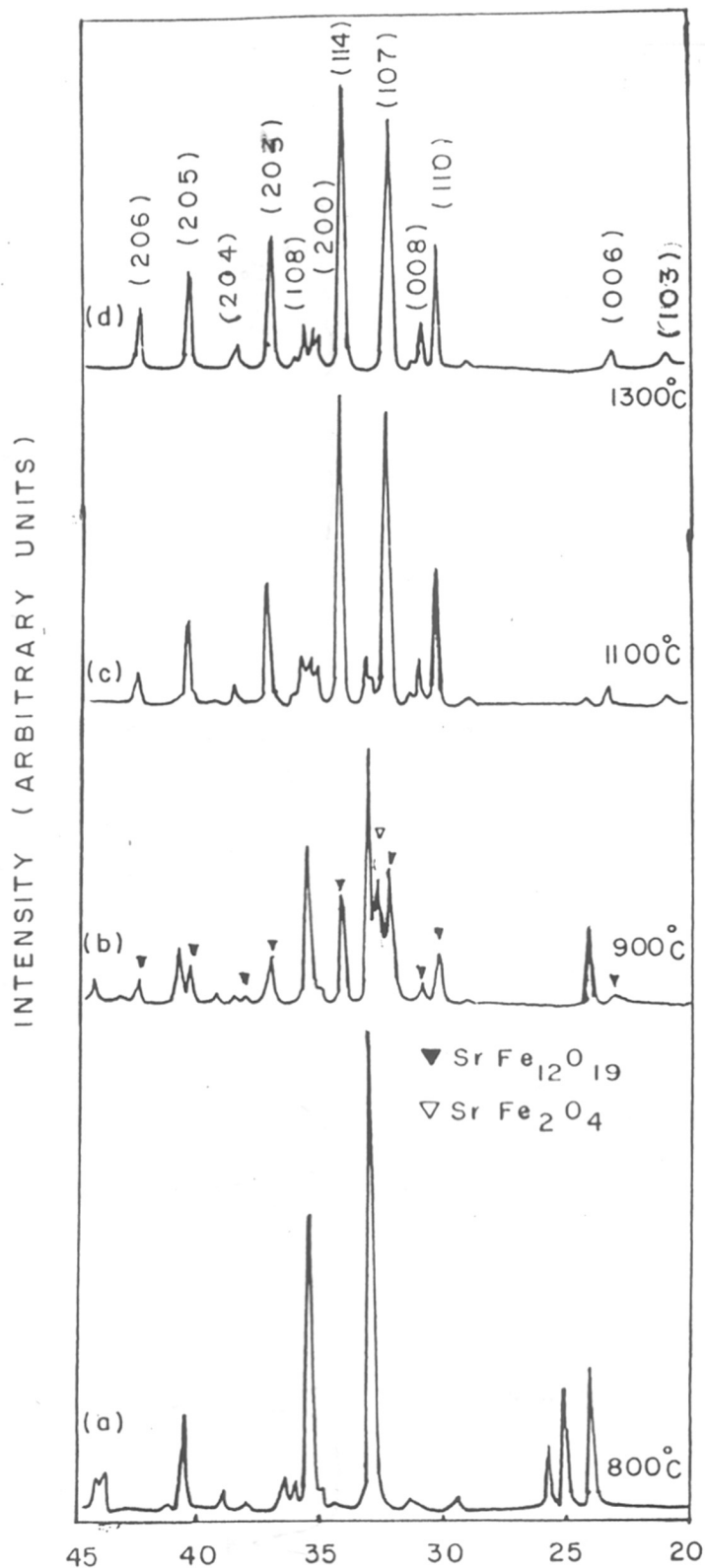


Fig.8: X-ray Diffraction patterns of sample A-1 heated at various temperatures between 800-1300°C

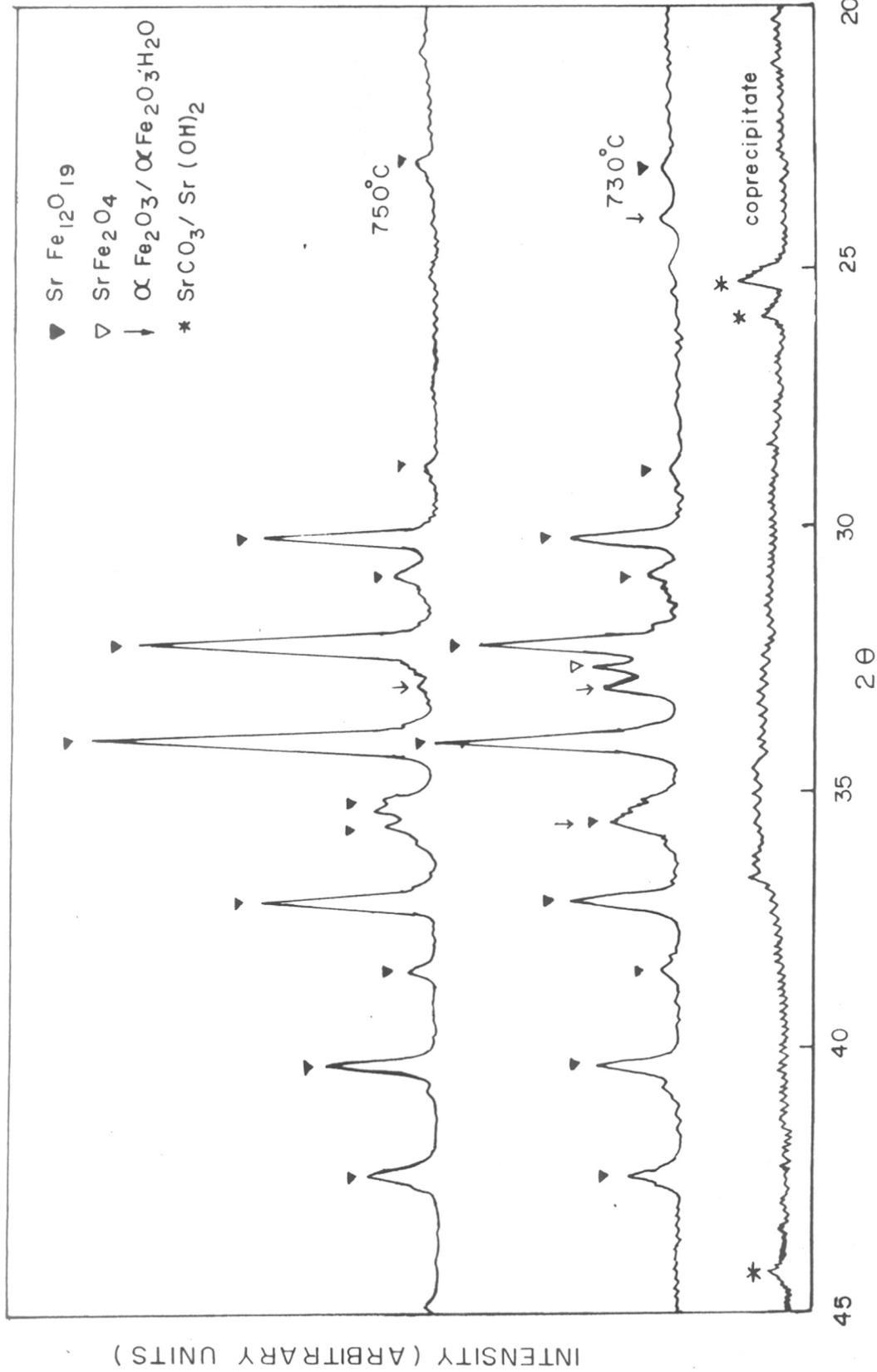


Fig. 9: X-ray powder diffraction patterns of sample B-1, heated at 730° and 750°C

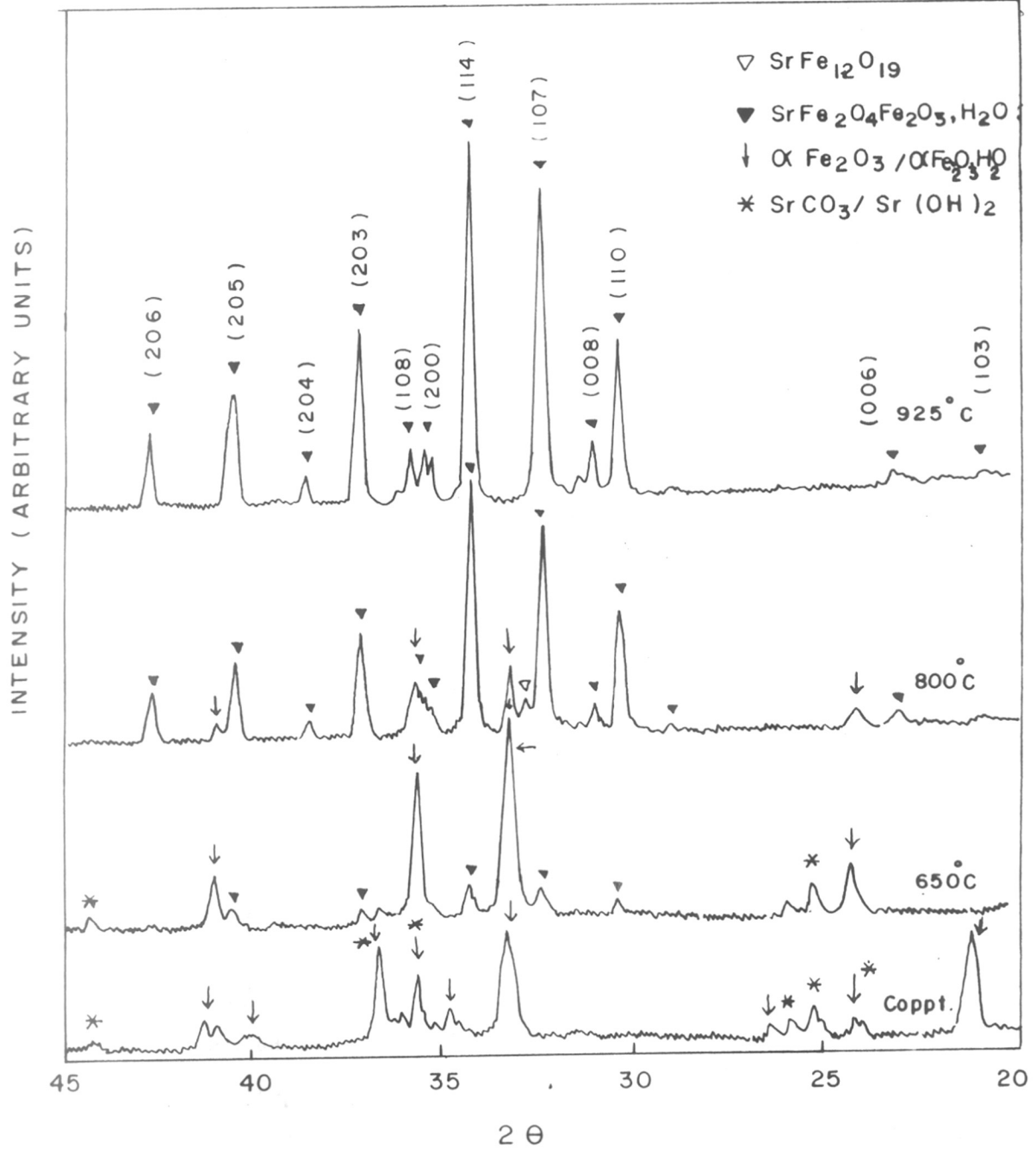


Fig.10: X-ray diffraction patterns of sample B-2 when heated at various temperatures, 650°, 800°, 925°C

the formation of strontium hexaferrite along with the substantial amount of the unreacted phases. Further the formation of ferrite seems to be incomplete even after heating at 800°C. Formation of SrFe_2O_4 spinel is clearly indicated with the characteristic peak at $2\theta = 32.8^\circ$. At $T = 925^\circ\text{C}$ most of the additional peaks vanish leaving behind a single phase strontium hexaferrite. The lines match well with those of the sample A-1.

Sample B-3 : Samples B-311 to B-317 (made from B-3) differ in their Fe/Sr ratio. When samples are calcined at 750°C the XRD patterns show that they are similar indicating main phase to be $\text{SrFe}_{12}\text{O}_{19}$ in all the ratios. A representative XRD pattern has been shown in Fig. 11 for the sample B-315 with Fe/Sr ratio = 11.0. When the samples are calcined at 925°C/2h (samples B-321 to B-327), the peaks of unreacted $\alpha\text{-Fe}_2\text{O}_3$ decrease in intensity and indication of SrFe_2O_4 spinel phase becomes more prominent. Same samples when treated with 1:1 HCl for 15 minutes, and washed with water till free from Cl^- ions, the peaks of SrFe_2O_4 disappear, as seen in Fig. 11.

Sample B-4 : This sample is heated at various temperatures from 600°C upto 1300°C with a step of 100°C successively, then cooled to room temperature. The subtle changes occurred in the structure are shown in Fig. 12. It is clear from the intensity analysis that the plain coprecipitate consists of $\text{Sr}(\text{OH})_2/\text{SrCO}_3$. Though the precipitation in case of this sample was done only by NaOH, the $\text{Sr}(\text{OH})_2$ formed during precipitation gets converted into SrCO_3 due to atmospheric

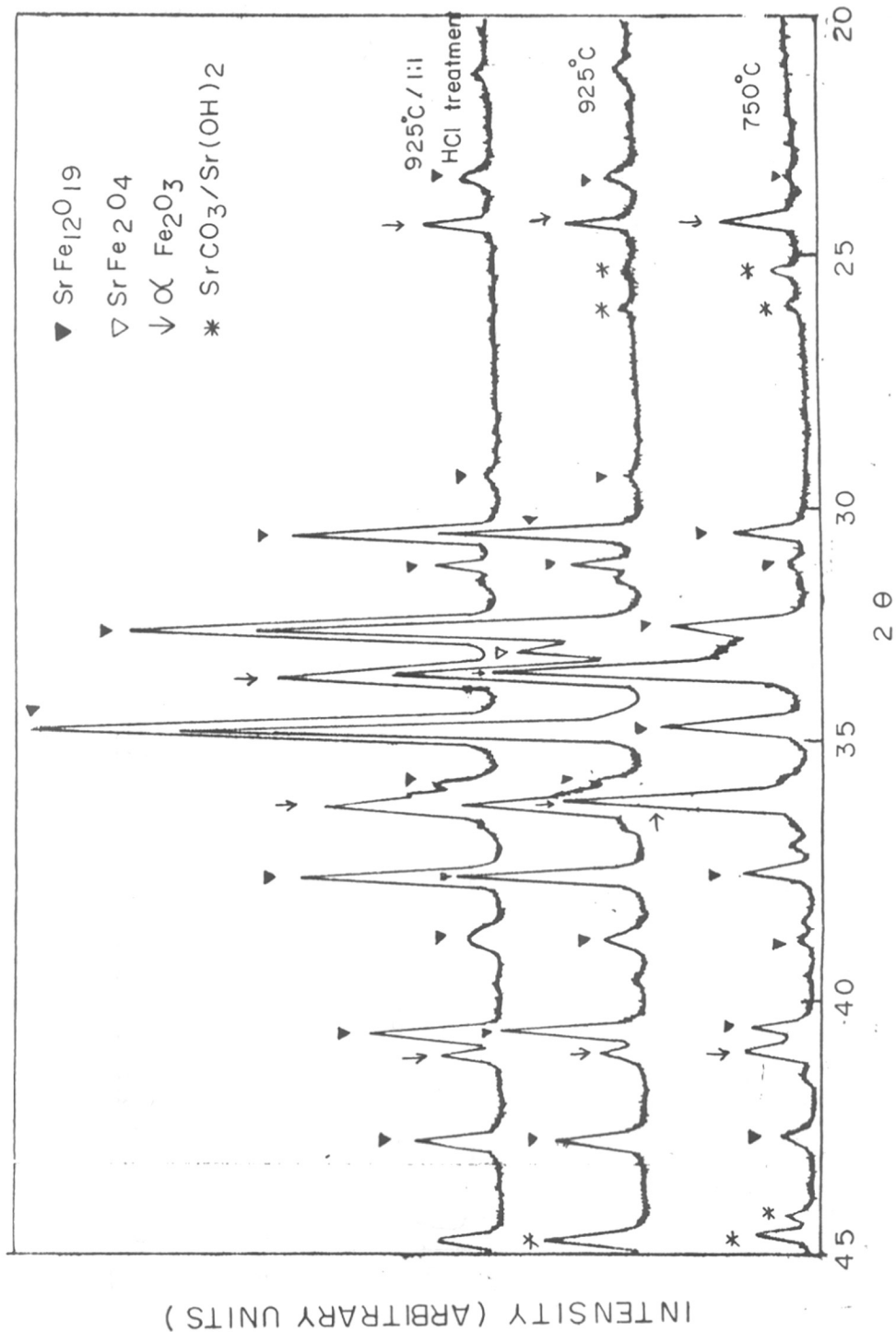


FIG. 11 : X-ray diffraction patterns of sample B-3, heated at 750°C and 925°C

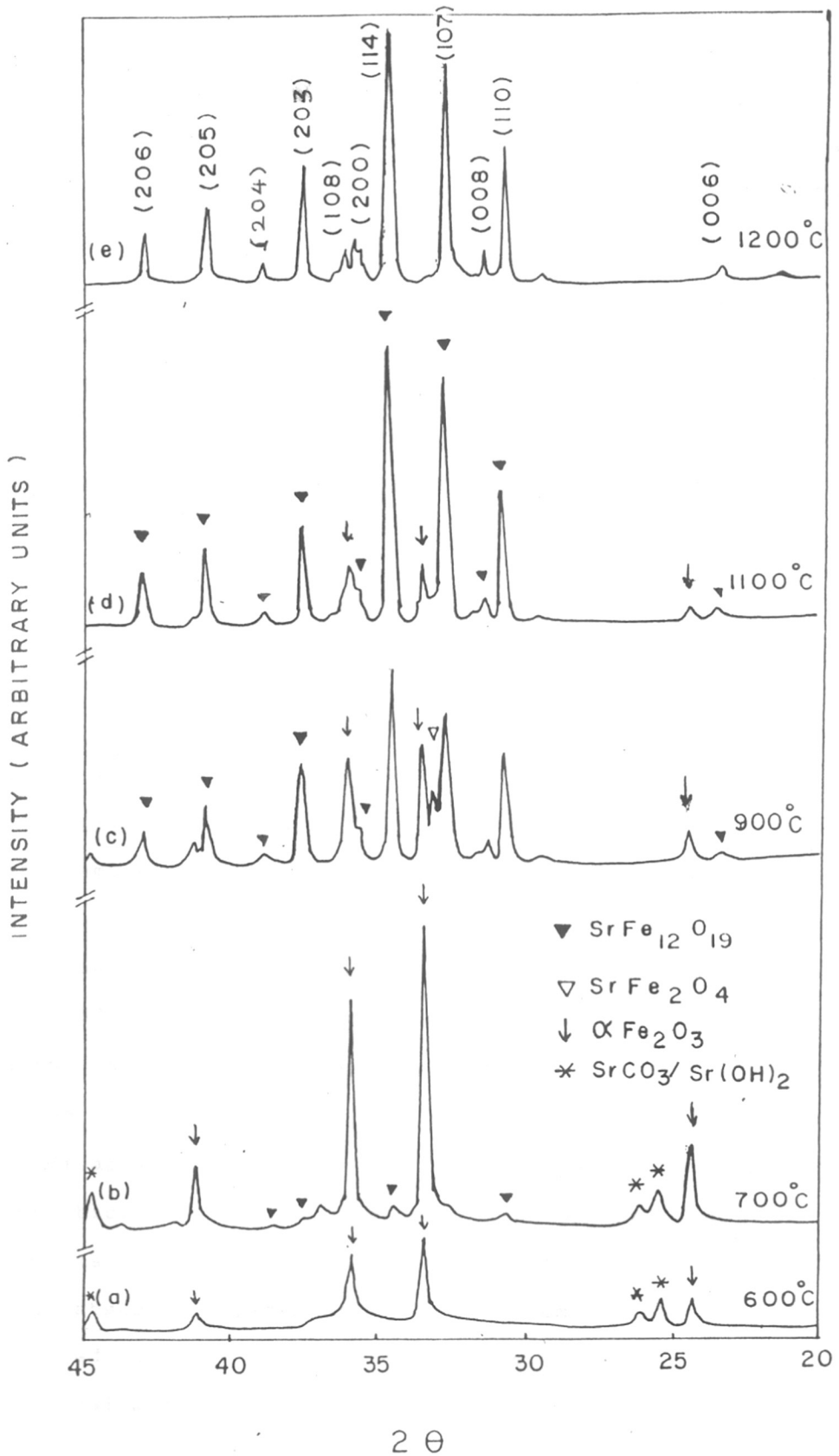


Fig.12: X-ray diffraction patterns of sample B-4, heated at various temperatures between 600°-1200°C

CO₂. As the temperature increases, ferritization starts at $\approx 700^{\circ}\text{C}$ and the reaction is complete at $T = 1200^{\circ}\text{C}$. The indication of SrFe₂O₄ spinel phase is clear at about 900°C , which goes on decreasing with increase in temperature and at 1200°C single phase strontium hexaferrite is formed.

Sample B-5 : This sample mainly differs from the others in the respect of the original reactants i.e. nitrates of Fe and Sr are used instead of chlorides. Fig. 13 shows that the XRD of this sample is almost the same as those of the other samples.

3.2.3 Infrared studies (IR)

To throw some more light on the formation of ferrite, infrared studies were made on samples A-1 and B-4.

Ceramic method : Sample A-1 : Fig. 14 shows the IR spectra of the sample, heated at various temperatures between 600 and 1300°C . In the $800\text{-}300\text{ cm}^{-1}$ region, the samples heated at $T \leq 800^{\circ}\text{C}$ show $\alpha\text{-Fe}_2\text{O}_3$ with its characteristic bands at ≈ 545 , 470 and 330 cm^{-1} , while that of SrCO₃ is at 860 cm^{-1} . These patterns changed successively above 900°C indicating chemical reaction between Fe₂O₃ and SrO/SrCO₃. The band at 860 cm^{-1} also disappeared and other peaks in the region $600\text{-}300\text{ cm}^{-1}$ became broad and split. The completion of the reaction at 1300°C as indicated by XRD was also confirmed by IR showing double absorption peaks at 600 and 450 cm^{-1} . These may be attributed to two kinds of Fe³⁺ sites, namely, [FeO₄] in tetrahedral and [FeO₆] in octahedral coordination [26].

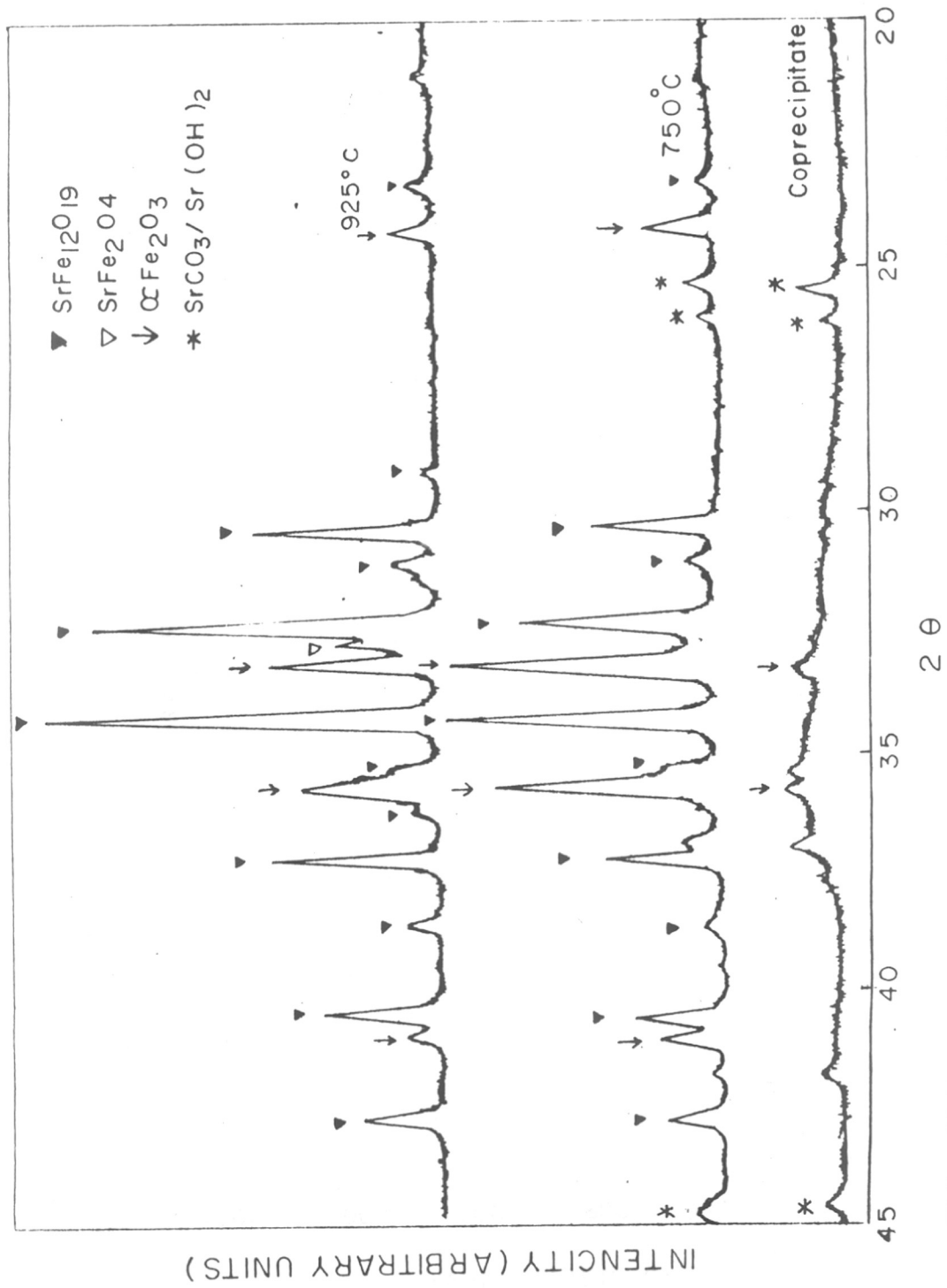


FIG. 13: X-ray diffraction patterns of sample B-5, heated at 750° and 925° C.

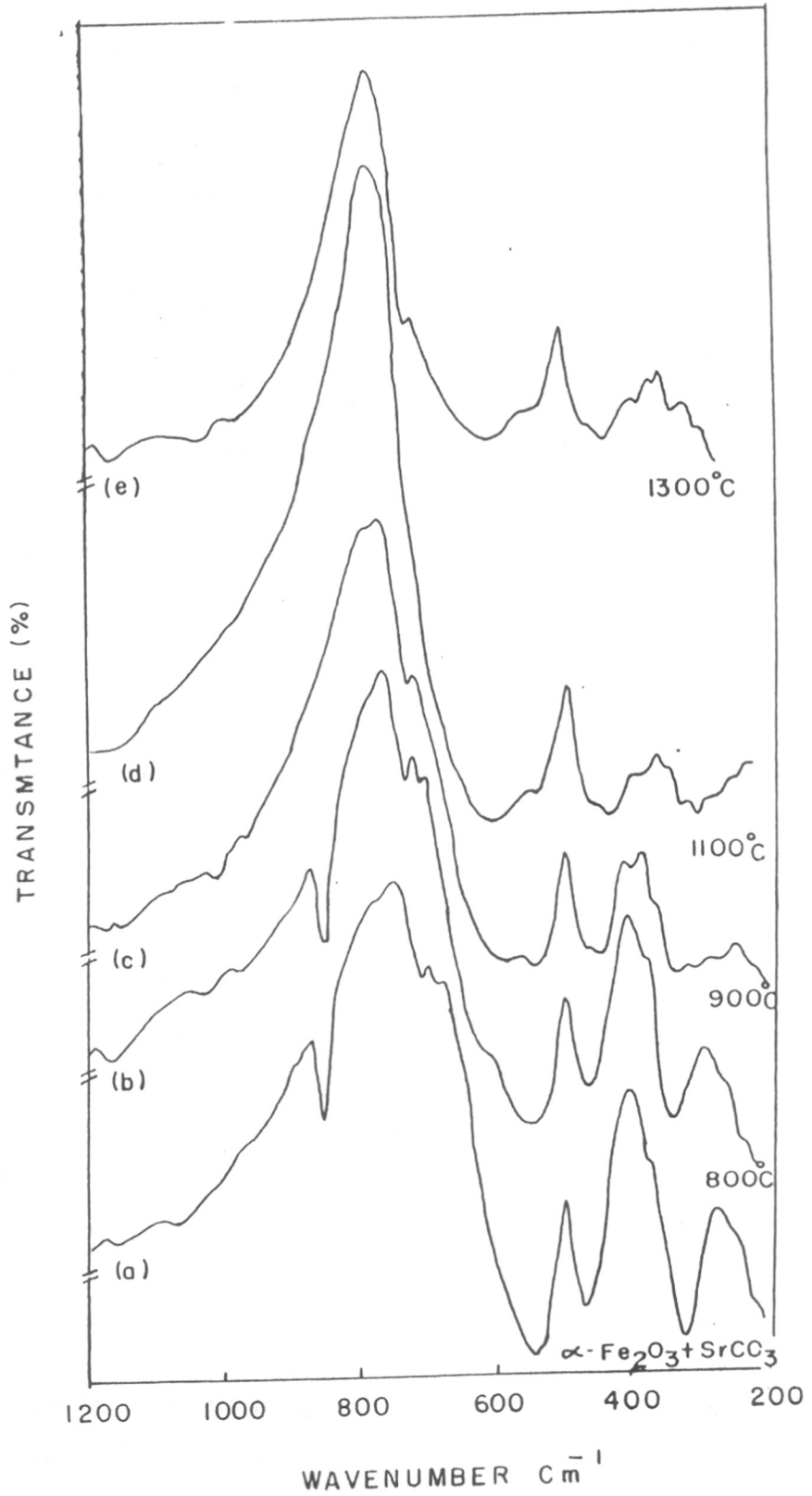
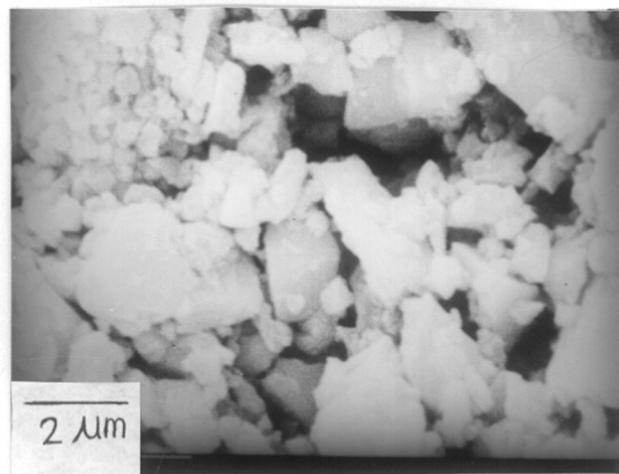


Fig.14: IR Spectra of sample A-1 heated at various temperatures between 800° to 1300 °C.

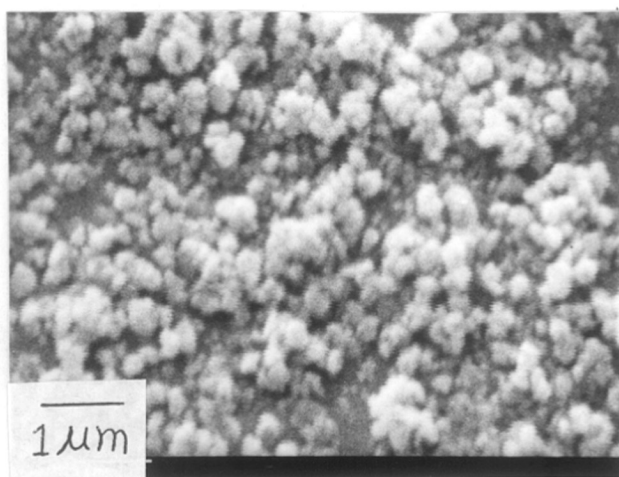
Coprecipitation method : Sample B-4 : Fig. 15 describes the changes in the IR spectra of the sample B-4. The inset of the figure shows that the fresh coprecipitate has bands at 3400 and 1610 cm^{-1} due to the stretching and bending vibration modes of water and structural hydroxyl groups [52]. Presence of SrCO_3 is indicated at $\approx 860 \text{ cm}^{-1}$. The hydroxyl bands disappear for the sample heated at 600°C due to the loss of water molecules while the band at 860 cm^{-1} goes on decreasing with the increase in temperature. In the region between 800 and 300 cm^{-1} , strong absorption bands due to the iron-oxygen lattice vibrations are observed at around 570 and 435 cm^{-1} indicating the presence of a hexagonal closed-packed arrangement of the oxygen sublattice, similar to that present in $\alpha\text{-Fe}_2\text{O}_3$ and $\alpha\text{-FeO.OH}$ [53]. IR spectra for the samples heated at $T \geq 800^\circ\text{C}$, exhibit broad and split bands. Ultimately two bands at 590 and 450 cm^{-1} are observed for the sample heated at 1200°C where strontium hexaferrite is fully formed as indicated by XRD pattern. The spectrum matches well with that obtained using the ceramic method.

3.2.4 Scanning electron micrograph studies (SEM)

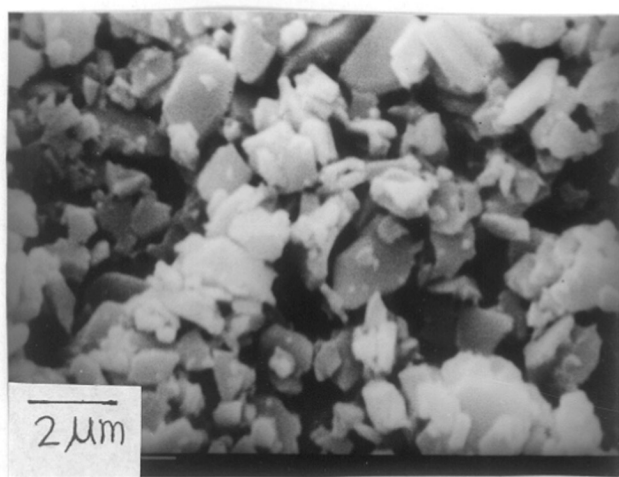
Particle size of the calcined powder is one of the key factors, affecting the magnetic properties. SEM technique provides the insight of the microstructure of the calcined powder. Fig. 16 gives an overview of the particle size and its distribution in samples A-1, B-1, B-2, B-3, B-4 and B-5. While Table 8 gives the summary of the SEM studies.



Sample
A-1
(cal. 1300^oc)

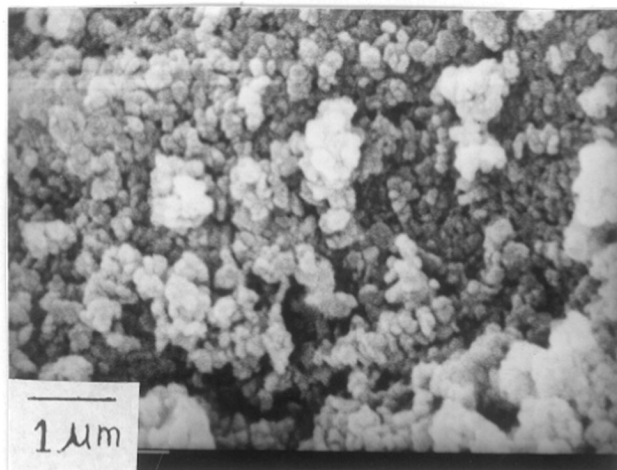


Sample
B-1
(cal 750^oc)

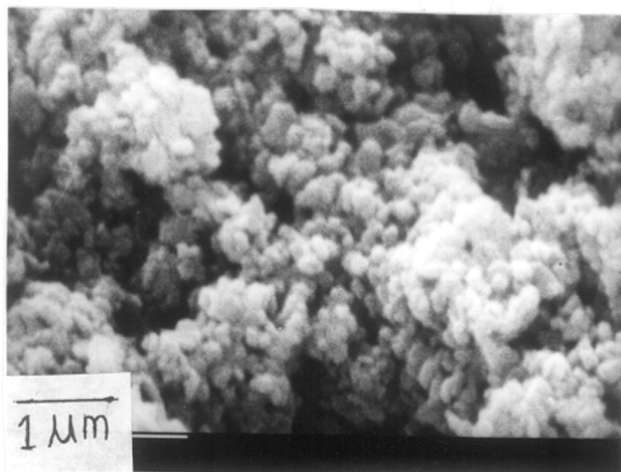


Sample
B-2
(cal 925^oc)

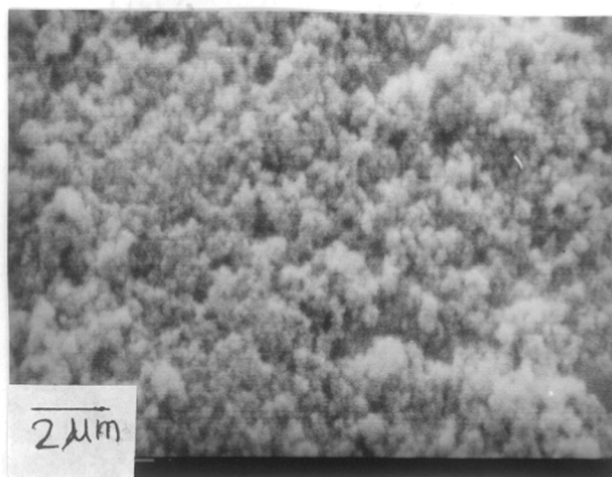
FIG.16: Scanning electron micrographs of
Sample A-1, B-1, and B-2



Sample
B-3
(cal 750 $^{\circ}\text{C}$)



Sample
B-4
(cal 750 $^{\circ}\text{C}$)



Sample
B-5
(cal 750 $^{\circ}\text{C}$)

FIG.16: Scanning electron micrographs of
Sample B-3, B-4 and B-5

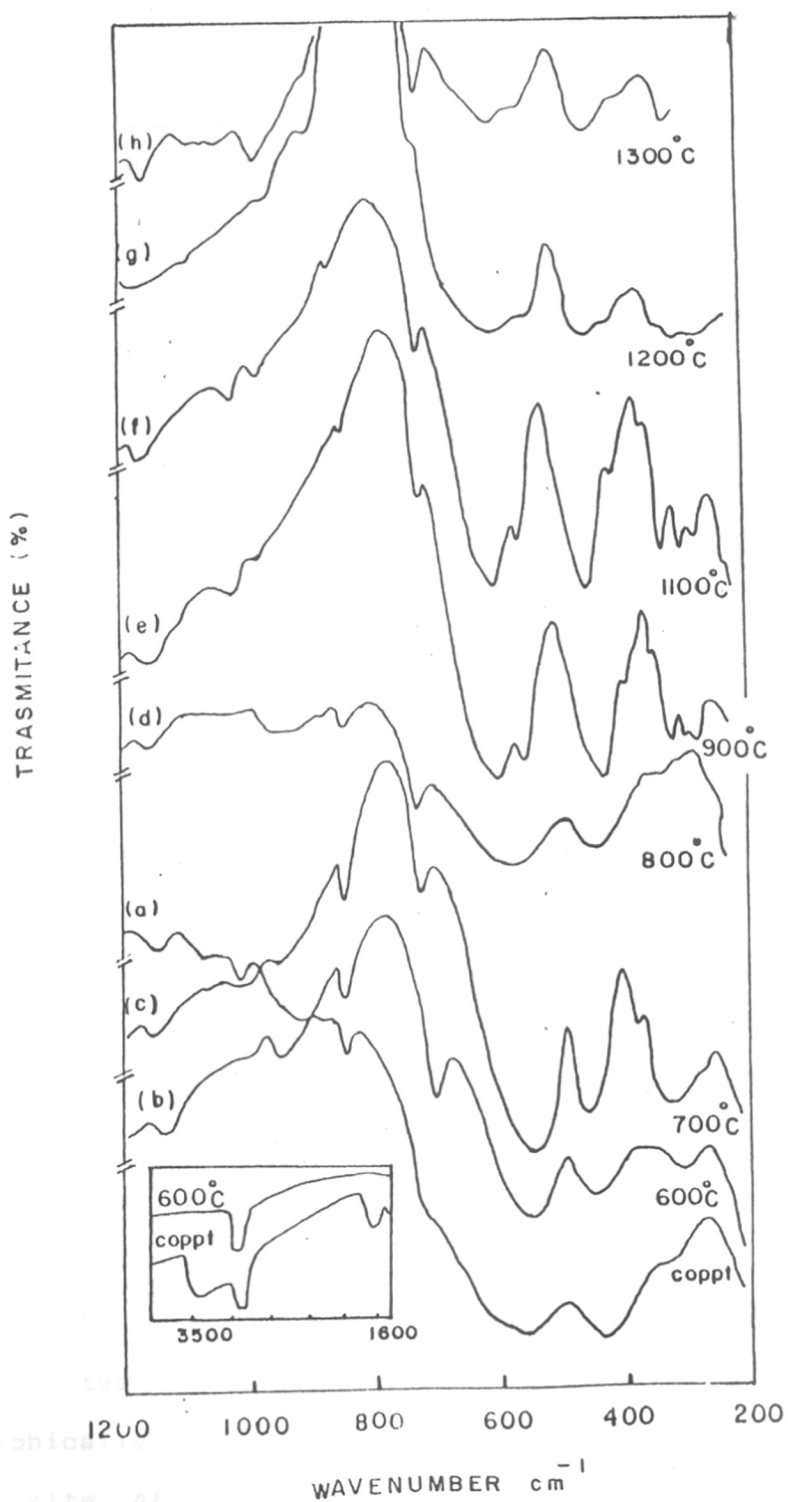


Fig. 15: IR Spectra of the sample B-4, heated at various temperatures between 600-1300°C. Inset-of the figure shows changes in the IR spectra of the wpreecipilate between 3600-1600 cm^{-1} .

Table 9 : Mossbauer parameters of strontium-ferrite prepared by two techniques

	Coprecipitation technique				Ceramic technique			
Mossbauer parameter	12k	4f ₂	4f ₁ + 2a	2b	12k	4f ₂	4f ₁ + 2a	2b
Isomershift $\delta \pm 0.02$ mm sec ⁻¹ w.r.t. Fe	0.37	0.43	0.24	0.42	0.34	0.35	0.31	0.28
Quadrupole splitting $\Delta E \pm 0.02$ mm sec ⁻¹	-0.41	-0.20	-0.13	-2.39	-0.41	-0.25	-0.13	-2.38
Hyperfine field H _n ± 5 kOe	414.0	517.0	496.0	419.0	414.0	517.0	496.0	419.0

3.2.6 Magnetic properties

The five basic samples, namely, A-1 and B-1 to B-5 were subjected to rigorous experiments in order to have a broad picture of the influence of the various processing parameters in terms of the magnetic properties, such as B_r , H_c , iH_c , $(BH)_{max}$, σ etc. Out of the large number of experiments done, a few illustrative ones are summarised in Table 10 (ceramic method), Table 11(a) (green samples, coprecipitation method) and Table 11(b) (sintered samples, coprecipitation method). Typical hysteresis loops of green as well as sintered samples for both the methods are given in Fig. 17(a,b).

Ceramic method : Set 1 Effect of Fe/Sr ratio : Taking into consideration the contamination from stainless steel ball-mill, the ratio of Fe/Sr was varied from 12.0 to 10.2 in the samples A-11 to A-13. The magnetic properties in Table 10 indicate that the ratio Fe/Sr = 11 to be the good one. Moreover the presence of the excess phase of SrO/BaO is known to help in preventing the grain growth during sintering, thereby increasing the coercive force [55].

Set 2 : Effect of binder : Various binders such as lignin, hydroxy ethyl cellulose and polyvinyl alcohol were tried in samples A-14, A-15, A-16. All the three show more or less similar properties.

Set 3 : Effect of sintering temperature : Sample A-16 was sintered at various temperatures ranging from 950-1280°C for

Table 10 : Magnetic properties of samples prepared by ceramic method

Parent sample No.	Sample No.	Pellet No.	Sintering temp/ °C/min	B _r G	H _c Oe	iH _c Oe	(BH) _{max} MG0e	D g/cm ³	σ emu/g
A-1	A-16	44	green	1400	700	1000	0.28	3.20	52.0
A-1	A-11	X-1	1280/90	2300	1650	2500	1.02	4.70	54.1
	A-12	X-2	1280/90	2400	1550	2050	1.17	4.80	54.4
	A-13	X-3	1280/90	2350	1300	1700	1.01	4.80	54.7
A-1	A-14	186	1250/15	2200	1650	2900	1.01	4.33	47.3
	A-15	196	1250/15	2200	1600	2760	0.98	4.48	42.6
	A-16	44	1250/15	2200	1650	2800	0.97	4.43	48.4
		59	1280/15	2200	1600	2700	0.92	4.54	49.1
A-1	A-17	432	1280/15	2300	1850	3300	1.09	4.60	51.9
		437	1280/15	2000	1700	3400	0.85	4.65	41.9
		442	1280/15	1900	1600	3400	0.73	4.57	47.0
		447	1280/15	2100	1800	3300	1.04	4.66	41.8
A-1	A-18	452	1280/15	2250	1700	2850	1.03	4.65	49.6
		457	1280/15	2150	1500	2700	0.90	4.56	45.8
		462	1280/15	1900	1050	1700	0.55	4.60	46.7
		467	1280/15	1900	1100	2000	0.60	4.70	48.2
A-1	A-19	472	1280/15	2300	1700	2450	1.08	4.70	55.4
		477	1280/15	2300	1800	2700	1.09	4.64	54.0
		482	1280/15	2200	1700	2050	0.99	4.58	53.0
		487	1280/15	2300	1800	3000	1.14	4.57	44.8

Table 11(a) : Magnetic properties of green samples prepared by coprecipitation method

Parent sample No.	Sample No.	Pellet No.	Calcination Temp/time °C/h	B _r G	H _c Oe	H _c Oe	(BH) _{max} MGDe	D g/cm ³	δ emu/g
B-1	B-11	C-252	750/5	1100	1000	6100	0.27	2.19	47.7
	B-12	C-261	750/5	1100	1000	6300	0.27	2.41	51.0
	B-13	C-12	800/3	1000	850	6250	0.20	2.60	42.8
	B-14	C-13	800/3	1100	950	6300	0.30	3.87	30.9
	B-15	C-27	750/5	1100	1000	6450	0.27	2.50	46.8
	B-16	C-22	750/5	1150	1050	6400	0.33	2.50	49.7
	B-17	C-E1	800/3	900	850	6500	0.20	2.76	38.9
	B-18	C-G1	800/3	900	850	6750	0.18	2.63	37.8
B-3	B-33	A-11	750/5	750	600	6250	0.10	-	-
B-4	B-41	L-281	750/5	800	550	3350	0.12	2.20	-
	B-42	L-248	925/2	1200	800	3900	0.27	-	-
	B-43	L-262	925/2	1300	900	4000	0.26	-	-
B-5	B-51	L-301	750/5	900	500	6150	0.15	-	-
	B-52	L-316	925/5	1100	750	6200	0.28	-	-
	B-53	L-347	750/5	800	550	6000	0.10	-	-

Table 11(b) : Magnetic properties of sintered samples prepared by coprecipitation method

Parent sample No.	Sample No.	Pellet No.	Sintering temp/time C/min	B _r G	H _c Oe	iH _c Oe	(BH) _{max} MGOe	D g/cm ³	δ emu/g
B-1	B-11	C-273	1150/15	2300	1300	1550	0.97	4.48	53.3
	B-12	C-272	1180/15	2400	1300	1500	1.09	4.66	44.4
		C-263	1150/15	2300	1800	3050	1.03	4.16	52.6
	B-13	C-261	1180/15	2350	1550	2550	0.96	4.60	47.6
		C-12	1150/15	2100	1400	2350	0.86	4.45	48.4
	B-14	C-13	1150/15	2650	1150	1300	1.24	4.36	57.5
B-15	C-26	1200/15	2500	1050	1200	0.97	4.54	52.1	
B-16	C-38	1200/15	2500	1700	2000	1.33	4.54	56.1	
B-2	B-21	204	1200/15	2350	1900	3700	1.14	4.61	46.6
		214	1200/15	1900	1300	2400	0.70	4.46	34.8
	B-22	224	1200/15	1700	1200	2550	0.51	4.38	30.9
		234	1200/15	1850	1300	2700	0.65	4.46	43.7
	B-23	284	1200/15	2300	1900	3500	1.09	4.52	45.8
		293	1200/15	2250	1900	4300	1.09	4.31	42.5
	B-24	303	1200/15	2250	1900	4300	1.04	4.34	49.5
		313	1200/15	2200	1850	4400	1.04	4.32	55.2
	B-25	243	1200/15	2300	1900	3500	1.09	4.51	43.2
		253	1200/15	2100	1750	4700	0.94	4.53	43.0
	B-26	264	1200/15	2100	1750	4400	0.98	4.49	34.5
274		1200/15	2150	1700	4150	0.99	4.49	46.1	
B-27	381	1100/15	2100	1800	4150	1.00	4.76	43.5	
	383	1200/15	2050	1600	3550	0.84	4.93	50.0	
B-28	391	1100/15	2100	1800	3900	1.00	4.53	43.9	
	393	1200/15	2250	1800	3700	1.04	4.77	46.7	
B-29	C-7	1200/15	2300	1900	4050	1.15	4.61	45.7	
B-30	LR-11	1200/2	2750	2000	2300	1.65	4.75	53.0	

Table 11(b) (contd.)

Parent sample No.	Sample No.	Pellet No.	Sintering temp/time C/min	B _r G	H _c		iH _c Oe	(BH) _{max} MGOe	D g/cm ³	ε emu/g
					H _c Oe	H _c Oe				
B-3	B-311	A-124	1150/120	2900	1800	3000	1.42	4.53	61.5	
		A-122	1200/60	3000	1750	2600	1.44	4.66	49.8	
	B-312	A-131	1150/240	3000	1800	2550	1.42	4.58	62.5	
		A-132	1200/60	3200	1750	2400	1.53	4.60	65.7	
	B-313	A-12	1150/120	2950	1850	3350	1.51	4.48	67.5	
		A-11	1300/15	3300	1850	2550	1.61	4.56	68.9	
	B-314	A-22	1200/60	2800	1800	3900	1.35	4.34	60.4	
		A-24	1150/120	2500	1700	4350	1.26	4.08	58.5	
	B-315	A-33	1150/240	2700	1700	3700	1.20	4.02	67.3	
		A-31	1280/15	2850	1400	1850	1.28	4.44	71.7	
	B-316	A-43	1150/240	2200	1450	4000	0.90	3.59	62.0	
		A-41	1280/15	2400	1400	2450	0.91	3.96	68.3	
	B-317	A-51	1150/240	2500	1500	3400	0.96	4.11	65.8	
		A-54	1150/120	2200	1450	4200	0.92	3.85	63.0	
	B-321	A-144	1150/15	2500	1750	3900	1.08	4.29	57.5	
	A-145	1240/15	2800	1600	2550	1.20	4.69	59.3		
B-322	A-155	1240/15	2700	1550	2450	1.20	4.62	68.9		
B-323	B-323	A-75	1220/15	2800	1700	2850	1.27	4.57	57.5	
		A-77	1240/15	2900	1650	2500	1.35	4.66	66.6	
		A-72	1200/60	2900	1750	2750	1.42	4.64	63.4	
	B-324	A-81	1250/240	2600	1750	4150	1.10	4.17	68.7	
		A-82	1200/60	2700	1700	3800	1.19	4.28	61.3	
	B-325	A-95	1220/15	2500	1600	3550	1.04	3.98	58.0	
		A-91	1150/240	2200	1450	4300	0.82	3.60	59.7	
	B-326	A-102	1150/240	2000	1400	4250	1.00	3.32	55.1	
		A-104	1280/15	2300	1400	2700	0.84	3.87	57.5	
	B-327	A-112	1200/15	2100	1400	4350	0.82	3.71	55.8	

Table 11(b) (contd.)

Parent sample No.	Sample No.	Pellet No.	Sintering temp/time C/min	B _r G	H _c Oe		iH _c Oe	(BH) _{max} MGDe	D g/cm ³	σ emu/g
					H _c Oe	H _c Oe				
B-4	B-41	L-289	1200/15	2400	1250	2000	0.81	4.17	63.0	
	B-42	L-259	1240/15	2150	1150	2000	0.66	4.11	61.0	
	B-43	L-257	1240/5	2100	1150	2050	0.66	4.00	53.7	
		L-272	1240/15	2300	1150	1850	0.72	4.30	60.1	
		L-270	1240/5	2400	1200	2050	0.81	4.10	65.0	
B-5	B-51	L-302	1150/15	2800	1600	2350	1.20	4.35	64.0	
	B-52	L-304	1150/30	2900	1400	1900	1.36	4.43	68.3	
		L-317	1150/15	2400	1450	2500	0.97	4.09	66.1	
		L-318	1150/30	2500	1400	2250	0.97	4.16	57.4	
	B-53	L-346	1150/240	3200	1800	2700	1.60	4.54	64.8	
		L-326	1150/240	3300	1800	3400	1.53	4.37	69.2	

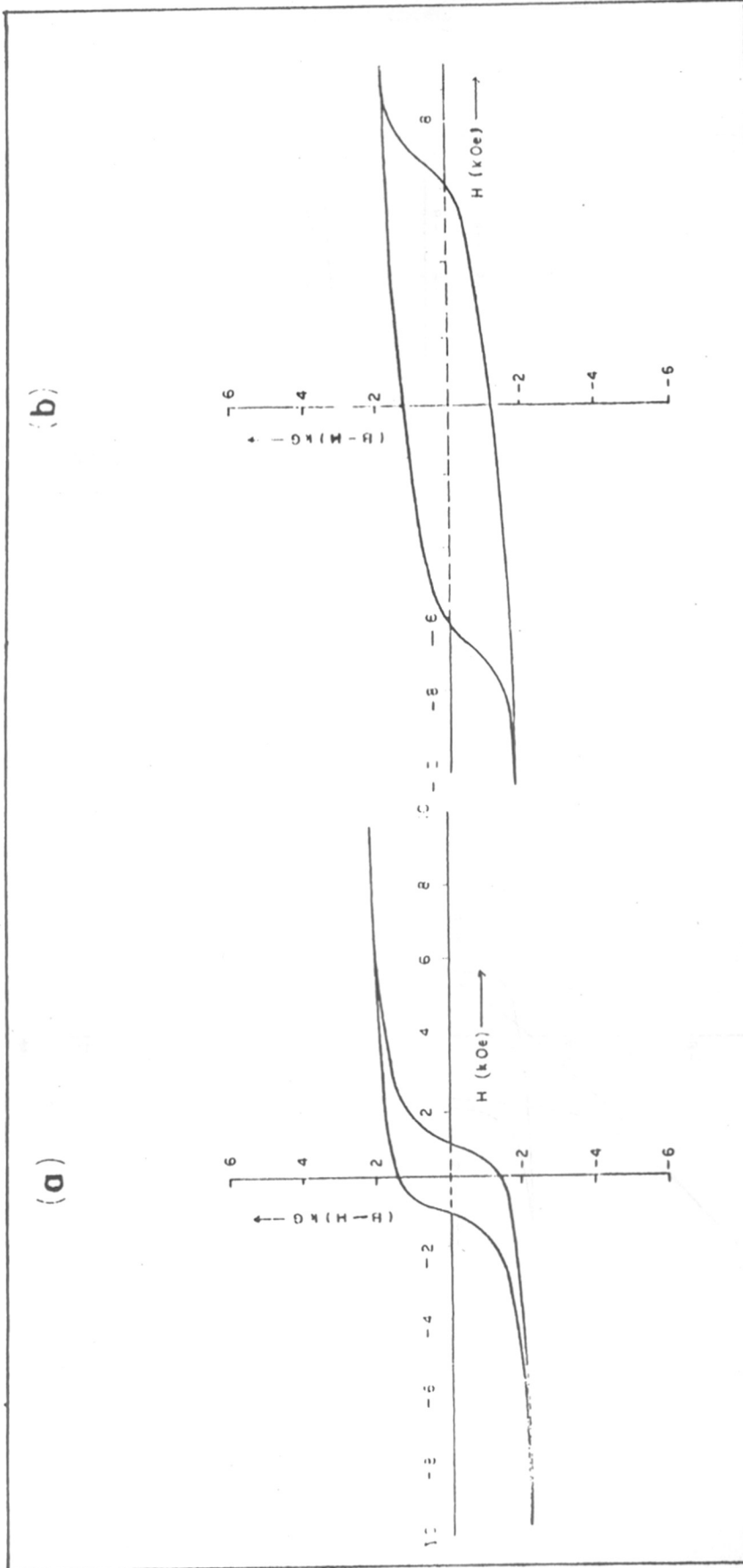


FIG. 17 (a) : Typical hysteresis loops of green samples prepared by (a) ceramic method,
 b) coprecipitation method .

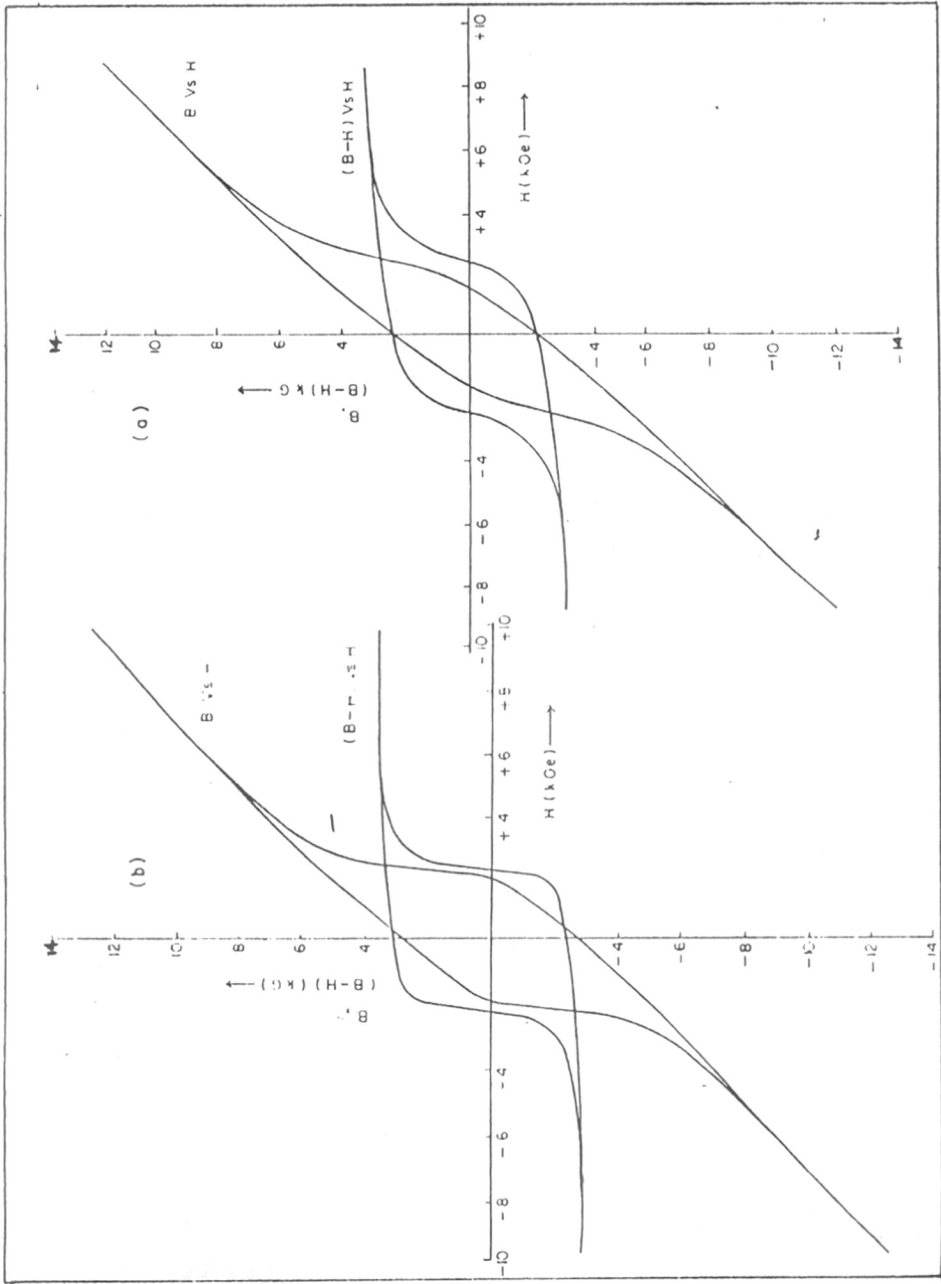


Fig. 17 (b) : Typical hysteresis loops of sintered samples prepared by (a) Ceramic method, (b) Coprecipitation method.

15 minutes. Fig. 18 depicts the trend in various magnetic properties. As the temperature increases, B_r , H_c $(BH)_{max}$ and D increase and maximize in the range between 1200° to $1300^{\circ}C$, while iH_c drops down due to the growth of the particles. Sintering temperature should be selected so as to have optimum values for all the magnetic properties.

Set 4 : Effect of dopants : Dopants are known to alter the magnetic properties in various ways. We tried aluminium (Al), cobalt (Co) and calcium (Ca) (samples A-17, A-18 and A-19) and varied their amounts from 0.5 to 2.0% by weight of the ferrite. Fig. 19 gives the perspective of the effect of dopants on H_c , iH_c , B_r and $(BH)_{max}$ as compared with those of the undoped sample (A-16). We observed that out of the three dopants, Ca affects B_r more while Al affects iH_c more. Co does not seem to have any favourable effect except at the composition 0.5% by weight. $(BH)_{max}$ and H_c also increase with Al and Ca while decrease with Co. Improvement observed in various properties is as follows : $iH_c \simeq 25\%$, $H_c \simeq 12\%$, $B_r \simeq 4-5\%$ and $(BH)_{max} \simeq 20\%$.

Coprecipitation method : Set I : Effect of chemical treatment
 Sample B-1, after calcination at $750^{\circ}C/5$ h was divided into two parts, namely, B-11 and B-12. B-11 was mixed with a binder PVA, and pressed into pellets while B-12 (20 g) was soaked in 1:1 HCl (200 ml) for 15 minutes. It was washed with distilled water till free from chloride ions. The feel of this material was very soft. It was then mixed with PVA and pressed into pellets. Table 11(a) shows that, at the

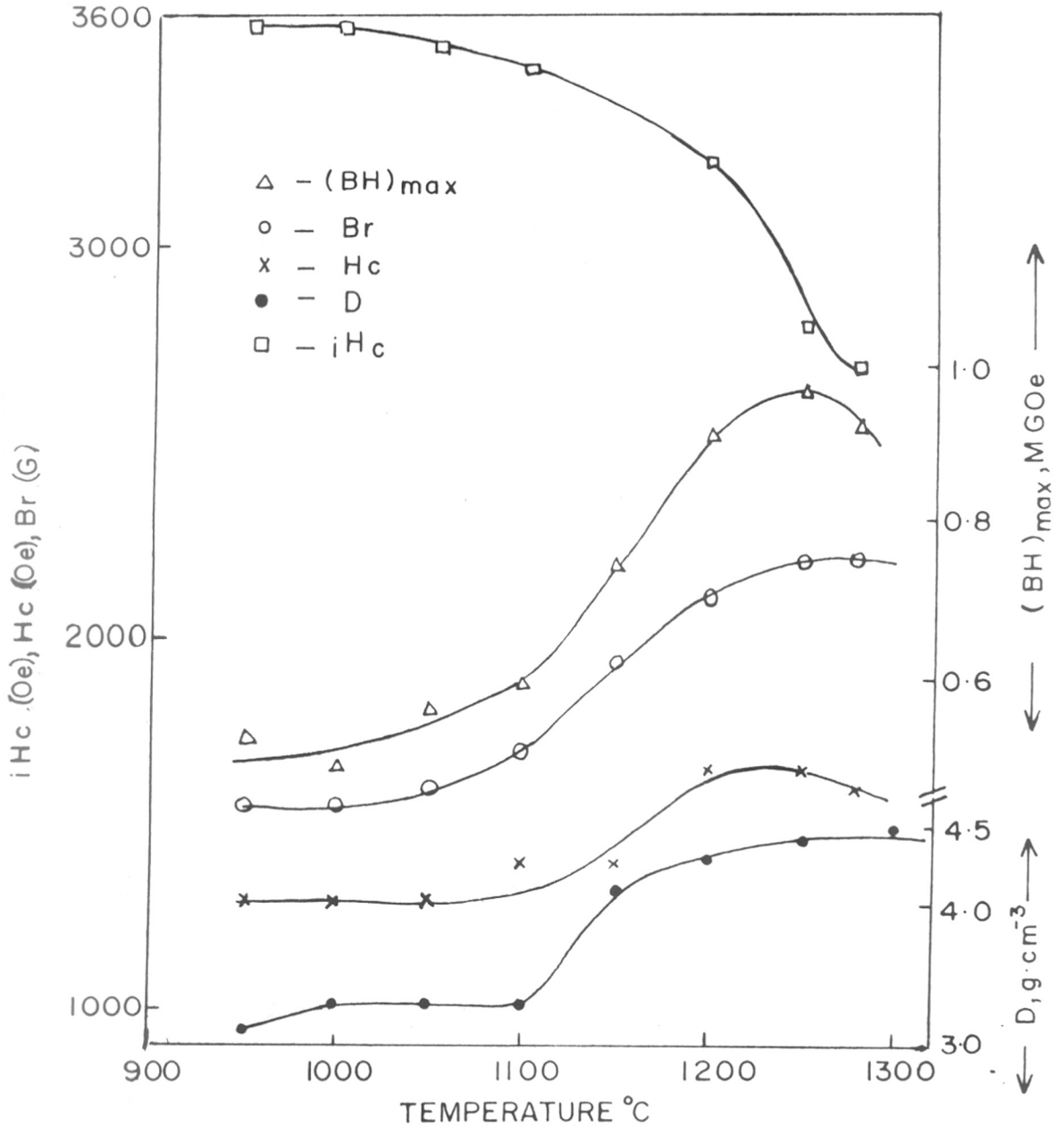


FIG.18 : Effect of sintering temperature on magnetic properties of samples prepared by ceramic method.

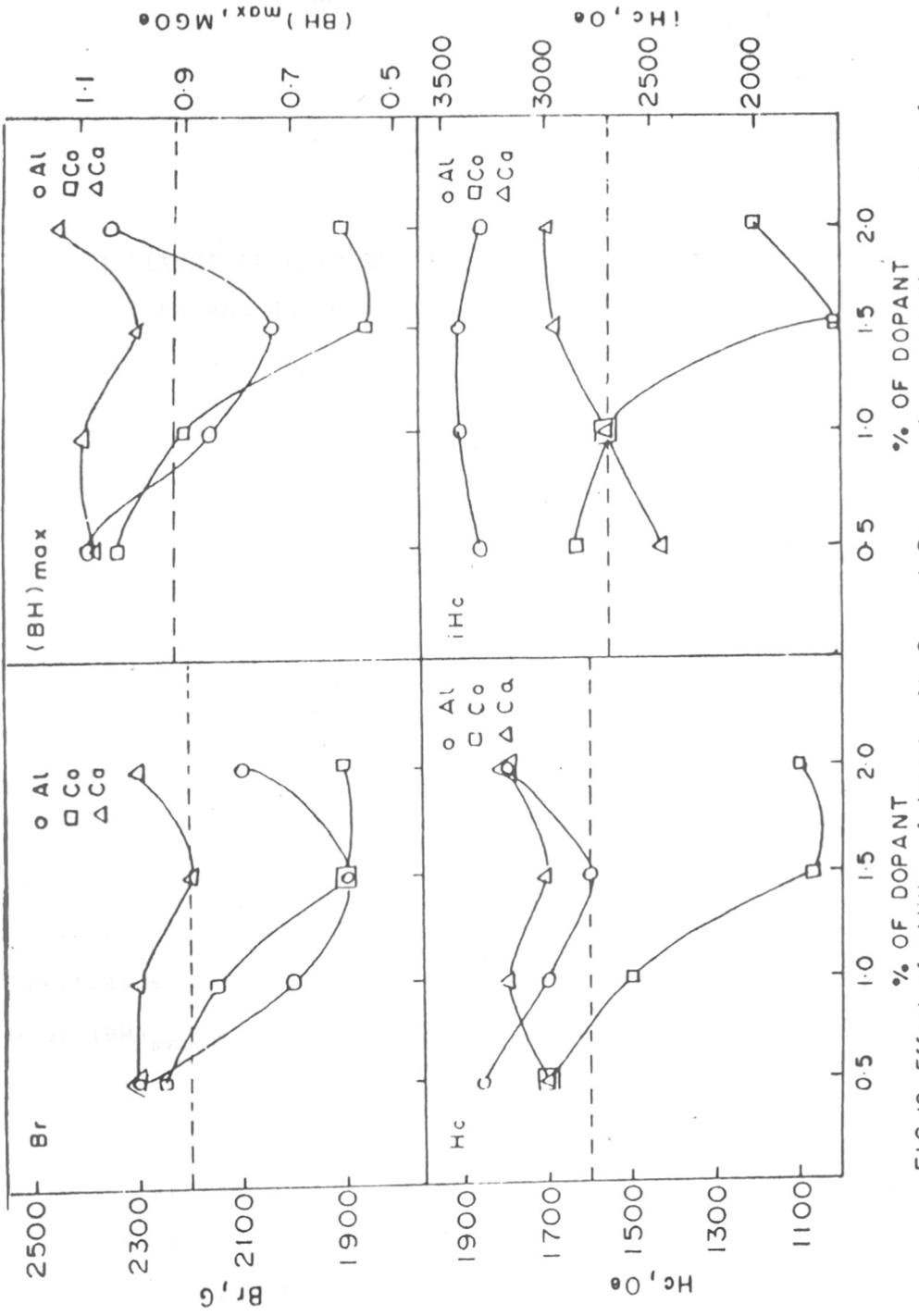


FIG 19 Effect of addition of dopants Al, Co and Ca on various magnetic properties of samples prepared by ceramic method. Dashed lines indicate undoped sample.

green stage, iH_C increases by ≈ 200 Oe while at the sintered stage iH_C increases by 1000 to 1500 Oe. HCl is known to dissolve the unreacted phases more easily than the hexaferrite phase. The mechanical stresses are also reduced [56].

Set 2 : Effect of rate of addition : In sample B-13 the mixture of Fe and Sr chlorides was added directly into the solution of NaOH/Na₂CO₃ with vigorous stirring, while in sample B-14 the mixture was added dropwise with a rate of 3-4 ml min⁻¹, into the solution of alkali. Afterwards both the precipitates were processed in identical way upto the sintering stage. The results in the Table 11(b) indicate that under optimum conditions of sintering, slow/dropwise addition ultimately resulted in better magnetic properties, with high $(BH)_{max} = 1.24$ MGOe compared to the value = 0.86 MGOe obtained for fast addition.

Set 3 : Effect of concentration of reactants : Sample B-15 used dilute solutions of all the reactants while in sample B-16 almost saturated solutions were used. The magnetic properties show that the sample with saturated solution gave higher $(BH)_{max}$ with higher iH_C value.

Set 4 : Effect of surfactants : Ethylene glycol (sample B-17) and glycerol trioleate (sample B-18) (1% by weight of the coprecipitate) were tried to see their effect on dispersion of the coprecipitate. They were added during coprecipitation, into the solution of alkali. The coprecipitated slurry, in both the cases was settled with difficulty even with centrifugation, thereby indicating the

fine nature of the coprecipitate. In magnetic properties iH_C value shows increase but $(BH)_{\max}$ is observed to have decreased.

Set 5 : Effect of dopants : In samples B-21 to B-25, dopants, namely, Al, Cr, Co, Bi and Pb were added to the coprecipitate, before calcination. Percentage of Al, Cr, Co was varied from 0.5 to 2.0, while Bi and Pb were added 5% by weight of the coprecipitate. Fig. 20 shows the effect of addition of Al, Co, Cr on various magnetic properties which indicate that Al has adverse effect on all the properties except when the percentage added is 0.5. Co seems to increase iH_C , while other parameters are rather decreased. For the dopant Cr, magnetic properties are more or less the same as those of the undoped sample. Dopants Bi and Pb are effective in increasing the density of the coprecipitated sample upto 4.9 , but the magnetic properties are not improved.

Set 6 : Effect of Fe/Sr ratio : The solubility of $Sr(OH)_2/SrCO_3$ is greater than $FeO.OH/Fe_2O_3.H_2O$, which may result in more loss of Sr, than that of Fe. This loss can be taken care of by adjusting the initial Fe/Sr ratio. In samples B-311 to B-317 the ratio was varied from 10.4 to 12.0 in steps of 0.2. Rigorous sintering cycles were carried out at various temperatures and for different time periods. Fig. 21 gives the dependence of $(BH)_{\max}$ on sintering temperature for various Fe/Sr ratios. It shows that for the ratios higher than 11, the $(BH)_{\max}$ is very poor, while it increases

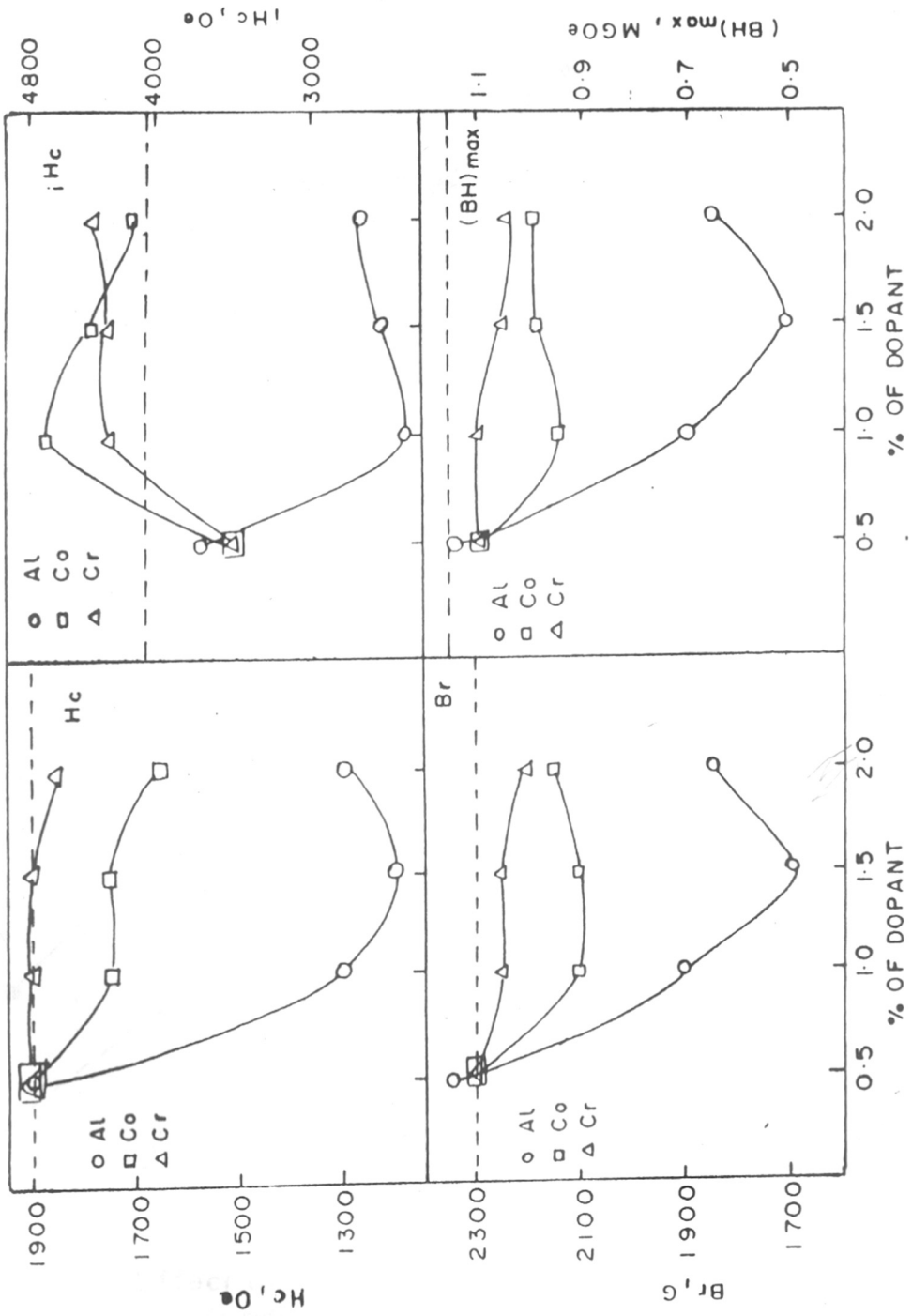


FIG. 20 : Effect of addition of dopants, Al, Co, and Cr on various magnetic properties of samples prepared by coprecipitation method. Dashed lines represent undoped sample

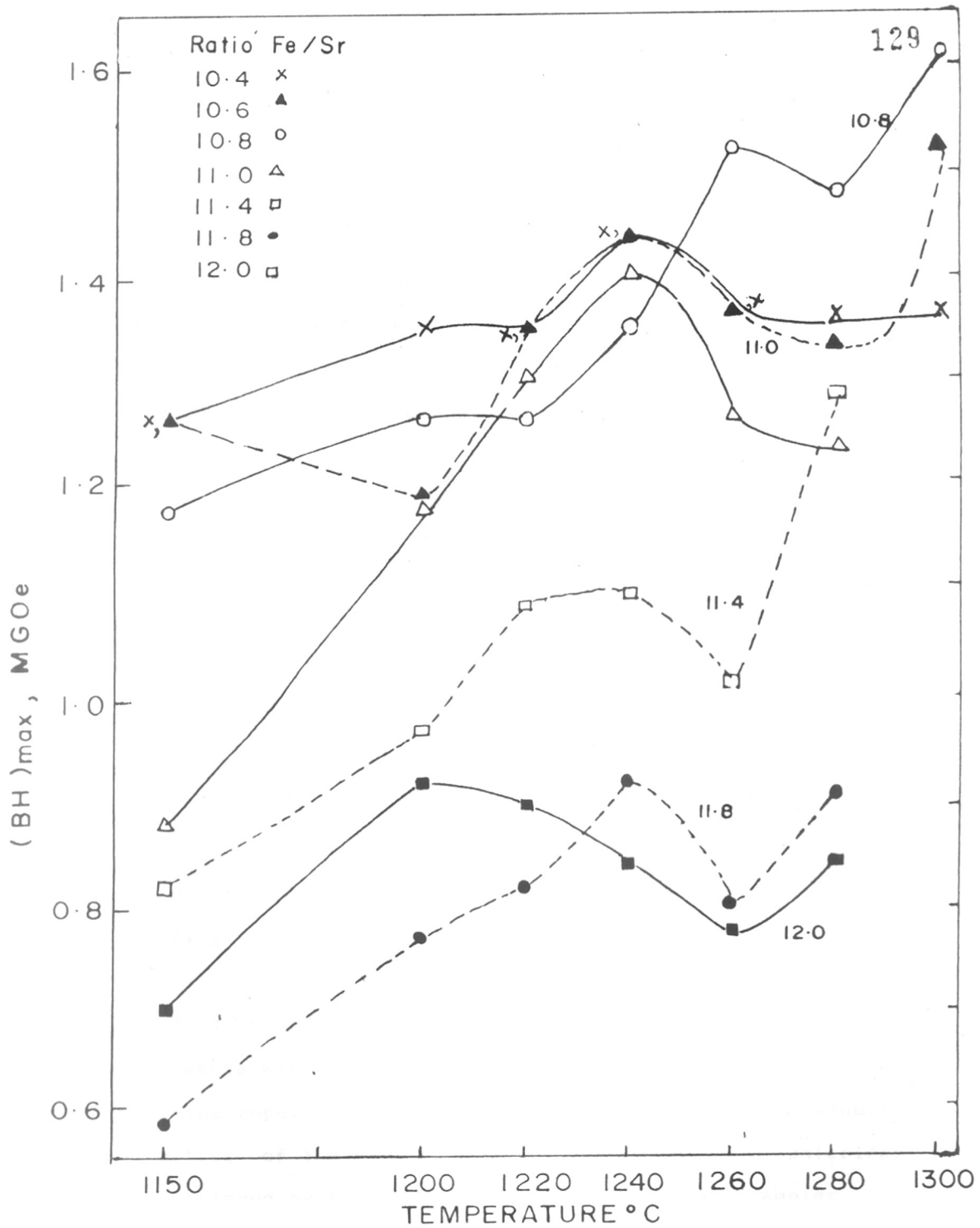


FIG. 21 : Effect of sintering temp on $(BH)_{max}$ for various Fe/Sr ratios.

as the ratio is decreased. For the ratios ≤ 11.0 , $(BH)_{\max}$ is 1.2 even at lower sintering temperatures. For the ratios other than 11.0 and 10.4, $(BH)_{\max}$ does not maximize even upto 1300°C , which is not admissible since particle size grows at such a high temperature. Sintering conditions were optimized separately for each ratio. Table 12 gives the optimized sintering conditions along with the magnetic properties obtained under those conditions. Fig. 22 pictures the behaviour of various magnetic properties at the optimized sintering conditions against the Fe/Sr ratio. The figure indicates that ratio ≤ 11.0 is better, where $(BH)_{\max} \approx 1.4 \pm 0.1$ can be obtained. The ratio Fe/Sr = 10.8, specifically seems to be the best at which all the magnetic parameters have good values. Table 13 gives the summary of the best results for B_r , iH_c and $(BH)_{\max}$. For the samples B-321 to B-327, the calcination was done at $925^{\circ}\text{C}/2$ h and the sintering was optimized for each sample. At the green stage the results were better than those calcined at 750°C , but the sintering results went upto $(BH)_{\max} = 1.4$ for the ratio 10.8 only.

Set 7 : Effect of quality of reagent : When we tried experiments with laboratory grade chlorides of Fe and Sr, we found the results to be poor as can be seen from the magnetic properties of the samples B-41 to B-43. But when chlorides were replaced by nitrates, the results improved (samples B-51 to 53). Precipitation of the sample B-53 was done in conditions of minimum pH variation during the

Table 12 : Magnetic properties at optimized sintering conditions, for different Fe/Sr ratios

Fe/Sr ratio	Sintering conditions °C/h	B _r G	H _c Oe	H _c Oe	(BH) _{max} MGDe	D g/cm ³	σ emu/g
10.4	1150/2	2900	1800	3000	1.42	4.53	61.5
10.6	1150/4	3000	1800	2550	1.42	4.58	62.5
10.8	1150/2	2950	1850	3350	1.51	4.48	67.5
11.0	1200/1	2800	1800	3900	1.35	4.34	60.4
11.4	1150/4	2700	1700	3700	1.20	4.02	67.3
11.8	1150/4	2200	1450	4000	0.90	3.59	62.0
12.0	1150/4	2500	1500	3400	0.90	4.11	65.8

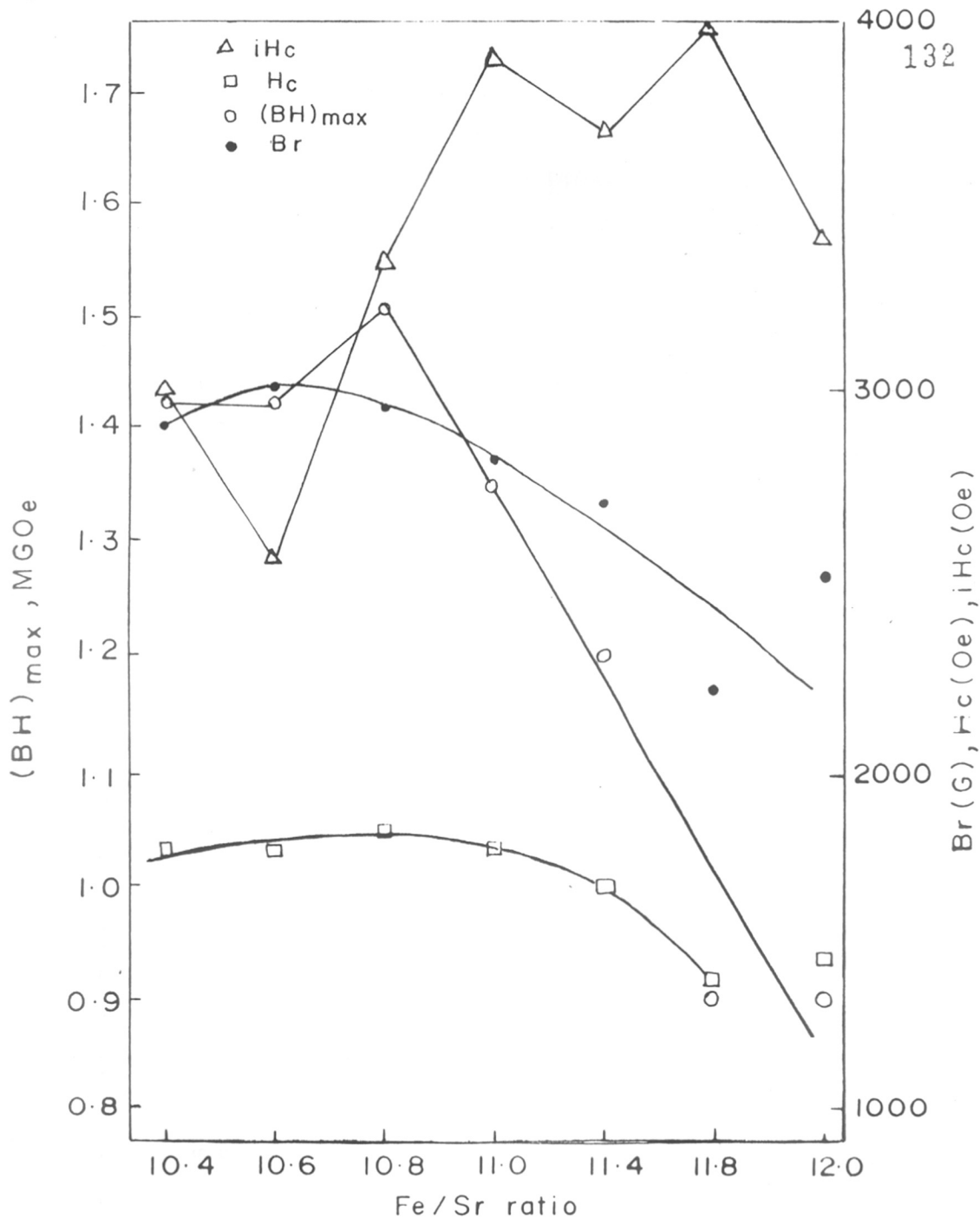


FIG. 22: Effect of Fe/Sr ratio on various magnetic properties at optimized sintering conditions for samples prepared by coprecipitation method.

Table 13 : Summary of the best results for B_r , i_{H_c} and $(BH)_{max}$

Sintering condition $^{\circ}C/h$	Fe/Sr ratio for highest B_r	Fe/Sr ratio for highest i_{H_c}	Fe/Sr ratio for highest $(BH)_{max}$
1150/2	10.8	11.0	10.8
1150/4	10.6	11.0	10.4
1200/ $\frac{1}{4}$	10.4	11.8 11.0	10.4
1200/1	10.6	11.0	10.6
1220/ $\frac{1}{4}$	10.4 10.6	11.8 12.0	10.4 10.6
1220/ $\frac{1}{2}$	10.8	11.0	10.8

coprecipitation. Amounts of Fe + Sr nitrates and NaOH, close to the stoichiometry were added dropwise to the remaining solution of alkali, so that throughout the precipitation, the change in pH will be as small as possible. Magnetic properties of this sample turned out to be very good.

3.3 SUMMARY

An attempt is made to understand and evaluate both the conventional ceramic method and nonconventional coprecipitation method. The results obtained from the various trials show that coprecipitation method is superior over the ceramic method. Particle size and its distribution is the critical key factor and is affected by the nature of preparation method. Following are the observations regarding the merits and demerits of both the methods.

(1) The DTA/DTG/TG studies indicate that the thermochemical behaviour of $\text{SrFe}_{12}\text{O}_{19}$ formation reaction is quite different in both the methods. Exothermic energy change is observed only for the coprecipitation method.

(2) (a) It is observed from the XRD studies that, in the case of the coprecipitation method, formation of the ferrite initiates at $\approx 600\text{-}700^\circ\text{C}$ and completes between $900\text{-}1200^\circ\text{C}$ while for the ceramic method, it initiates at higher temperature at $\approx 900^\circ\text{C}$ and completes at $\approx 1300^\circ\text{C}$. Thus, calcination at lower temperatures to initiate the formation of the hexagonal ferrite, becomes possible for the coprecipitation method.

(b) In the coprecipitation method, when the samples are washed with the help of centrifugal filtration, (refer samples B-1 and B-2), the reaction is complete between 800-950°C, while those washed by siphoning (refer B-3, B-4, B-5), require higher temperature for complete conversion of the coprecipitate to ferrite. In the case of washing with the help of centrifuge, the coprecipitate becomes more compact due to the centrifugal force and thus drying also is done in the lump form. This helps in having intimate contact required for solid state reaction. In the case of washing by siphon action, the precipitate remains in the slurry form during washing and drying and ultimately results in loose/fluffy powder. The colour of this powder is also light brown compared to that washed with the help of centrifuge.

(c) Formation of a spinel ferrite phase (SrFe_2O_4) is observed in all the samples at the early stage of preparation, irrespective of the method of preparation. The exact role of this phase is not known.

(3) IR studies indicate that both the methods proceed in a similar fashion during the formation of ferrite. IR spectra of the final products from the two methods match well.

(4) As observed from the SEM studies, the coprecipitated ferrite is more uniform and submicronic in size, with a narrow distribution in particle size. Thus the polycrystalline $\text{SrFe}_{12}\text{O}_{19}$ differs in the microstructure, if formed by the two different methods.

(5) The finer and more reactive nature of the powder results in lowering the calcination temperature upto 750-950°C as

compared to 1250-1300°C followed in the ceramic method.

(6) For lower calcination temperature, the feel of the sample is more soft and uniform. It needs no additional ball milling. The powder is then free from contamination and contains less mechanical strains.

(7) The fine/fluffy powder prepared by coprecipitation method is difficult to press and results in lower green densities.

(8) Due to lower calcination temperature required in the coprecipitation method, the final sintering also can be achieved in the range between 1100-1200°C compared to $T \geq 1300^\circ\text{C}$ required in the ceramic technique. Consequently the energy consumption is reduced.

(9) In the case of coprecipitation method, the magnetic properties at the sintered stage are always better for the samples calcined at $\approx 750^\circ\text{C}$ than those calcined at higher temperatures like 925°C . It is felt that, though most of the ferrite is formed at 925°C , in the sintering cycle, the grains grow unnecessarily, thereby deteriorating the magnetic properties. Thus according to the needs of application e.g. rubber magnet or permanent magnet, one has to concentrate on improving the results at the green stage or the sintered stage respectively.

(10) Chemical treatments like HCl or addition of surfactant improve the results at various stages. HCl treatment dissolves the phases other than the hexaferrite (refer XRD of B-3), thereby making the powder more pure, while the surfactants help to disperse the coprecipitate more

efficiently and thus reduce the agglomeration of particles.

(11) In case of ceramic as well as the coprecipitation method, addition of dopants result in varied and rather contradictory observations.

(12) When we compare the results of the samples B-1 to B-5 in view of the differences in precipitation procedures, following are the observations :

(a) When the precipitating agent NaOH only, was used instead of NaOH + Na₂CO₃, it was with the expectation that Sr(OH)₂ will be precipitated instead of SrCO₃ and the calcination temperature can be lowered because Sr(OH)₂ decomposes at much lower temperature than SrCO₃. But the Sr(OH)₂ converts into SrCO₃ due to atmospheric CO₂ and thus further lowering of the calcination temperature was not possible.

(b) Though the number of washings and amount of water was maintained the same, the pH of the final washing is different in centrifuge washed and siphon washed precipitate, due to mode of washing. Thus the final precipitate differs in sodium as well as strontium content, which affect the ultimate properties. The systematic study in this regard is under progress.

(c) When we change the raw materials from chlorides to nitrates, the results improve. One of the possible reasons may be that the chlorides are difficult to wash off completely than nitrates and therefore contaminate the precipitate.

(13) Coprecipitation method has inherent drawback, that the composition of the final product cannot be controlled very

precisely and accurately, because the loss of strontium during washing is greater than that of iron due to the difference in their solubilities. Efforts were made to overcome this difficulty by adjusting the initial Fe/Sr ratio. But the exact loss could not be anticipated or estimated. The powder has been analysed chemically at various stages, but due to lack of facilities to estimate strontium, exact chemical analysis could not be done. Iron was estimated volumetrically which gave satisfactory results. (14) In spite of various advantages observed in case of the coprecipitation method, it seems rather difficult to commercialize the process; due to large number of variables required to be controlled [27] to have reproducible results. Thus the rejection ratio is very high.

Attempts are being made to identify and control a few of the processing parameters and work is under progress to see the effect of the identified as well as the unidentified parameters in a more detailed way, in order to exploit the method to the full possible extent.

REFERENCES

1. G. Aminoff,
Geol.Foren.Stockholm, Forth, 47 (1925) 283.
2. V. Adelskold,
Arkiv.Kemi Mineral Geol., 12-A (1938) 1.
3. X. Obradors, X. Solans, A. Collomb, D. Samaras,
J. Rodriguez, M. Pernel and M. Font-Altaba,
J.of Solid State Chemistry, 72 (1988) 218.
4. E.W. Gorter, ~~75 (1959) 27~~
Philips Research Report, 9 (1954) 321;
Proc.IEEE, 104:B (1957) 225.
5. Q.A. Pankhurst, D.H. Jones, A.H. Morrish and X.Z. Zhou,
Advances in Ferrites : Proc.Fifth Int.Conf. on Ferrites,
India, (1989) 323.
6. G. Abanese, M. Carbuicchio and A. Deriu,
Phys.Stat.Sol. (a), 23 (1974) 351.
7. C. Zener,
Phys.Rev., 81 (1951) 440.
Phys.Rev. 82 (1951) 403.
8. NMAB Report on Magnetic Materials, Mar. 1985, National
Research Council, U.S.A.
9. Y. Kato and T. Takei,
U.S. Patents, 1,976,230 and 1,997,193.
10. A. Cochardt,
J.Appl.Phys., 37:3 (1966) 1112.
11. B.T. Shirk and W.R. Buessem,
J.Appl.Phys., 40:3 (1969) 1294.
12. ASTM File Numbers (i) 7-276 and (ii) 33-1340.
13. B.J. Evans, F. Grandjean, A.P. Lilot,
R.H. Vogel and A. Gerard,
J.Magn.Magn.Mat., 67 (1987) 123.
14. D.J. De Bitetto,
J.Appl.Phys., 35 (1965) 3482.
15. H. Yamada, M. Takano, M. Kiyama, T. Takada, T. Shinjo
and K. Watanabe,
Proc.Fourth Int.Conf. on Ferrites, San Francisco, (1984)
169.

16. E. Kreber and U. Gonser,
Appl.Phys., 1 (1973) 339.
17. G. Turilli, F. Licci, S. Rinaldi and A. Deriu,
J.Magn.Magn.Mat., 59 (1986) 127.
18. Landolt-Bornstein New Series, Edited by K.H. Hellwege,
Group III/12-C (1982), Springer-Verlag Berlin-Heidelberg.
19. V. Florescu, M. Popescu and C. Ghizdeanu,
Int.J.Magn., 5 (1973) 257.
20. P. Dullenkopf and H.P.J. Wijn,
Z.Angew Phys., 26 (1969) 22.
21. V.A. Gorbaryuk and G.V. Samsonov,
Sov.Powder Metall.Met.Ceram., 10 (1971) 471.
22. V.P. Cheparin and A.P. Cherkasov,
Bull.Acad.Sci., USSR, Inorg.Mater., 8 (1972) 174.
23. F.J. Esper and G. Kaiser,
Int.J.Magn., 3 (1972) 189.
24. K. Friess,
Z.Angew.Phys., 21 (1966) 90.
25. S. Ram., D. Bahadur and D. Chakravorty,
J.Magn.Magn.Mat., 71 (1988) 359.
26. K. Higuchi, S. Naka and S. Hirano,
Adv.Ceram.Mat., 1:1 (1986) 104.
27. F. Chou, X. Feng, J. Li and Y. Liu,
J.Appl.Phys., 61:8 (1987) 3881.
28. K. Haneda and H. Kojima,
Jap.J.Appl.Phys., 12:3 (1973) 355.
29. F. Haberey,
Ferrites : Proc.Int.Conf., Japan, Sept.Oct. (1980) 356.
30. K.K. Laroia and A.P.B. Sinha,
Ind.J.Pure and Appl.Phys., 2 (1965) 48.
31. E.C. Stoner and E.P. Wohlforth,
Philos.Trans.R.Soc., A-240 (1948) 599.
32. G.W. Rathenau,
Rev.Mod.Phys., 25:1 (1953) 297.
33. K.J. Sixtus, K.J. Kronenberg and R.K. Tenzer
J.Appl.Phys., 27:9 (1956) 1051.

34. K. Haneda and H. Kojima,
Phys. Stat. Sol. A, 6:1 (1971) 259.
35. D.V. Ratnam and W.R. Buessem,
J. Appl. Phys., 43:3 (1972) 1291.
36. K. Haneda and H. Kojima,
J. Appl. Phys., 44:8 (1973) 3760.
37. W. Roos, C. Voigt, H. Dederichs and K.A. Hempel,
J. Magn. Magn. Mat., 15:18 (1980) 1455.
38. P. Grohs,
IEEE Trans. Magn., MAG-20:5 (1984) 1633.
39. M.H. Hodge, W.R. Bitler and R.C. Bradt,
J. Am. Ceram. Soc., 56:1 (1973) 497.
40. A.L. Stuijts,
Trans. Brit. Ceram. Soc., 55:1 (1956) 57.
41. K. Saito, F. Hashimoto, M. Okuda and M. Torii,
IEEE Trans. Magn., MAG-17:6 (1981) 2656.
42. H.B. Von Basel,
IEEE Trans. Magn., MAG-17:6 (1981) 2654.
43. K. Haneda and H. Kojima,
Jap. J. Appl. Phys., 12:3 (1973) 355.
44. J. Smit and H.P.J. Wijn,
Ferrites, (1959), N.V. Philips' Gloeilampenfabrieken,
Eindhoven, Holland.
45. A.J. Dekker,
Solid State Physics, (1952), Macmillan and Co. Ltd.,
London.
46. Li Yi and Z. Long,
IEEF, Trans. Magn., 25:5 (1989) 4105.
47. K. Haneda, C. Miyakawa and H. Kojima,
J. Am. Cer. Soc. Bull., 57:8 (1974) 354.
48. H. Kojima, K. Goto and C. Miyakawa,
Ferrites : Proc. Int. Conf. Japan, Sept.-Oct., (1980) 335.
49. Z. Zong-yu, G. Bi-jun and M. Xue-Ming,
J. Magn. Magn. Mat., 78 (1989) 73.
50. W.W. Wendlandt,
Thermal Methods of Analysis (1974), John Wiley and Sons,
Inc., New York.

51. A. Marotta and A. Buri,
Thermochimica Acta, 25 (1978) 155.
52. A.C. Vajpei, Uma, I.P. Saraswat and K. Chandra,
J.Mater.Sci., 19 (1984) 3341.
53. K. Kauffman and F. Hazel,
J.Inorg.Nucl.Chem., 37 (1975) 1139.
54. A.M. Van Diepen and F.K. Lotgering,
J.Phys.Chem.Solids, 35 (1974) 1641.
55. J. Mallikarjuna and A.R. Das,
Trans.Ind.Ceram.Soc., 48:5 (1989) 86.
56. W. Roos, H. Haak, C. Voigt and K.A. Hempel,
J. Physique C1, 38 (1977) 5.
57. A.P.B. Sinha in 'Solid State Chemistry' edited by
C.N.R. Rao (1974), Marcel Dekker, Inc., New York.

CHAPTER 4

GOPPER MANGANITE

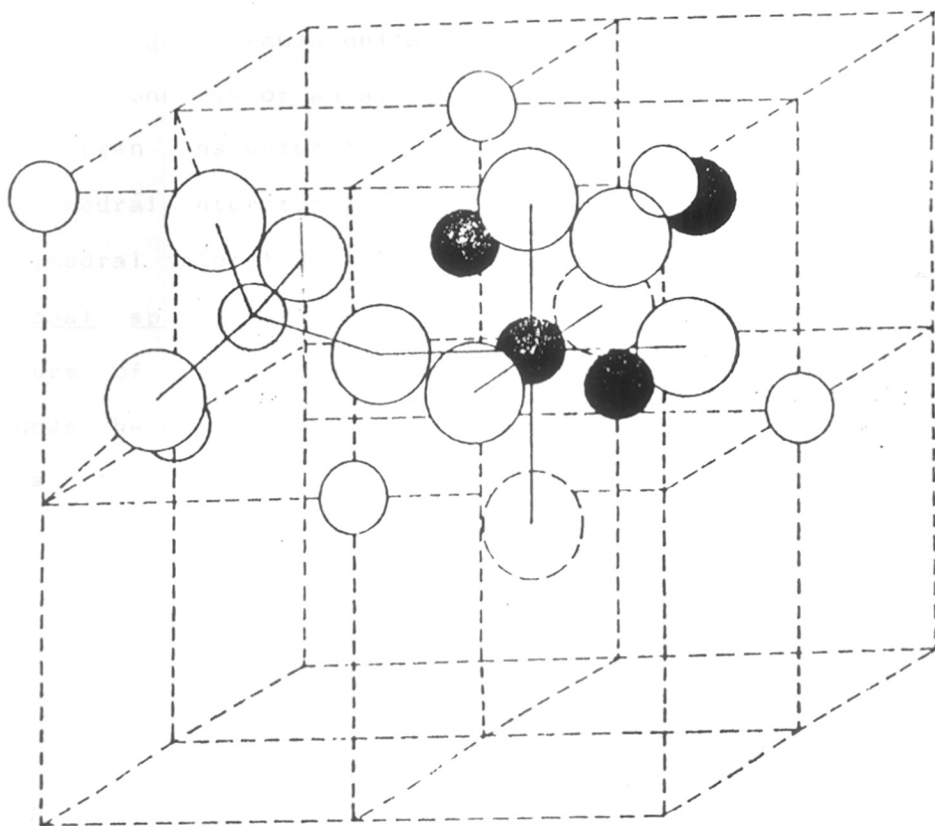
Application of the coprecipitation technique has been further extended to synthesize copper manganite (CuMn_2O_4). Chapter 4 deals with the preliminary studies on the preparation of copper manganite by the coprecipitation technique as compared to the usual ceramic technique. Section 4.1 gives a brief account on spinels in general, Section 4.2 discusses the results of various experiments done on copper manganite and Section 4.3 gives the conclusions drawn from both the methods of preparation.

4.1 INTRODUCTION TO SPINES

Spinel is a generic name for a class of compounds, isomorphous with the mineral, magnesium aluminate i.e. MgAl_2O_4 . In 1915 Bragg [1] studied the structure of this mineral and found it to be cubic and comparable to the structure of diamond, with each carbon atom replaced by a molecule of the spinel. Spinel can be represented by a formula $\text{A}[\text{B}_2]\text{O}_4$, where A is a metal ion at tetrahedral site and B is the metal ion at octahedral site. Ferrites AFe_2O_4 , manganites AMn_2O_4 , aluminates AAl_2O_4 , cromites ACr_2O_4 , etc. are a few of the well known members of the spinels family. Spinel are further classified into cubic and tetragonal spinels.

4.1.1 X-Ray structure : Cubic spinel

Fig. 1 illustrates the cubic structure of the spinel. The unit cell has the lattice parameter $a \approx 8 \text{ \AA}$.



Oxygen ions.



Tetrahedral cations.



Octahedral cations.

FIG. 1.

UNIT CELL OF AN IDEAL SPINEL SHOWING ONLY TWO OCTANTS

There are eight formula units of AB_2O_4 per unit cell. The structure consists of an almost perfect cubic close packing of 32 oxygen ions which form 64 tetrahedral interstices and 32 octahedral interstices. Out of these, 8 tetrahedral and 16 octahedral interstices are occupied by the 24 metal ions.

Tetragonal spinel : Aminoff [2] studies the crystal structure of a related compound, Mn_3O_4 . A number of compounds belonging to this tetragonal structure are also known and they are called as 'distorted spinels or tetragonal spinels'. The unit cell is a body centered tetragon with $a \simeq 5.5 \text{ \AA}$ and $c \simeq 9 \text{ \AA}$. There are four AB_2O_4 molecules per unit cell. 8 cations are at octahedral sites and 4 cations are at tetrahedral sites. Octahedral site has 4 oxygens (O_1) situated in the C-plane and 2 oxygens (O_2) perpendicular to the C-plane.

$$\frac{\text{distance from } O_2 \text{ to cation}}{\text{distance from } O_1 \text{ to cation}} = \frac{C}{a\sqrt{2}}$$

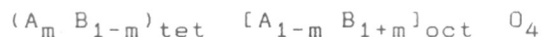
Thus it is a distorted octahedron, while the tetrahedral site has 4 oxygens all at equal distance. The above described body centered unit cell becomes comparable to the cubic spinel when converted into a larger C face-centered tetragonal cell, with the lattice parameters a' and c' given by a relationship $a' = a\sqrt{2} \simeq 8 \text{ \AA}$ and $c' = C \simeq 9 \text{ \AA}$. The unit cell volume of this new cell is twice that of the body centered cell and contains 8 molecules of AB_2O_4 .

4.1.2 Classification on the basis of cation distribution

Barth and Posnjak [3] introduced the names 'Normal', 'Inverse' and 'Random' to the following 3 types of distribution of cations.

- | | |
|--|------------------|
| (1) 8 A ions occupy 8 tetrahedral sites
16 B ions occupy 16 octahedral sites | } Normal spinel |
| (2) 8 B ions occupy 8 tetrahedral sites
8 A ions + remaining 8 B ions occupy
16 octahedral sites | } Inverse spinel |
| (3) 8 A and 16 B cations are distributed
randomly among 8 tetrahedral and 16
octahedral sites. | } Random spinel |

General cation distribution can be written as



$m = 1$ normal spinel

$m = 0$ inverse spinel

$0 < m < 1$ random spinel

This cation distribution plays a very significant role in electrical and magnetic properties of the spinel [4-6]. Cation distribution cannot be easily detected by X-ray diffraction method as mostly A and B ions have similar X-ray scattering power. Determination of resultant magnetic moment offers useful method for analysing the cation distribution. Verwey [7] investigated the cation distribution in spinels and gave the following site preferences for various ions.

(a) Zn^{2+} , Cd^{2+} , Ca^{2+} , In^{3+} , Ge^{4+} prefer tetrahedral site,

(b) Ni^{2+} , Cr^{3+} , Ti^{4+} , Sn^{4+} prefer octahedral site,

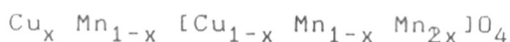
(c) Mg^{2+} , Fe^{2+} , Co^{2+} , Mn^{2+} , Fe^{3+} are indifferent ions,

Gorter [8] classified such distribution on the basis of electronic configuration, type of hybridization etc. A very useful concept 'Ligand Field Stabilization Energy (LFSE)' has also been employed in the literature.

4.1.3 Structure of manganite

Many of the manganites crystallize in tetragonal spinel structure (Hausmannite structure). The distortion to the tetragonal structure has been explained by Dunitz and Orgel [9] on the basis of Jahn-Teller theorem; it says that 'if an electronic state of a non-linear molecule is degenerate, the system is unstable and it will undergo some kind of distortion which will lower its symmetry and split the degenerate state', e.g. Cu^{2+} ion is situated at the octahedral site, the 'd' electron configuration of the ion is $(t_{2g})^6 (e_g)^3$. It gives rise to a doubly degenerate ground state, hence the regular octahedral arrangement is unstable. Distorted manganites transform from tetragonal to the cubic spinel structure when heated at elevated temperatures. For Mn_3O_4 , the phase transition temperature is $\approx 1170^\circ\text{C}$ [10]. Tetragonal to cubic phase change can occur also when the distorting ion is removed from the octahedral site [10,11]. Miyahara [12,13] studied the distortions in Cu-manganite. He reported that CuMn_2O_4 exhibits no tetragonal distortion due to the compensation effect of cupric ion ($c/a < 1$) and manganic ion ($c/a > 1$). When Cu is replaced by Zn, Mn or Cr, the distortion reappears. Shefler [14] found that depending on preparation condition copper manganite can show slight

departure from the normal spinel structure and he assigned the formula



Lot of work has been done on the spinel manganites in NCL. Irani, Sinha and Biswas [15] determined the structure of many tetragonal manganites as a function of temperature and found a transformation to cubic phase in all cases. Finch, Sinha and Sinha [16] treated this problem theoretically on the basis of order disorder process. The effect of removal of Mn^{3+} ions on the crystal distortion was first studied by Finch et al. [16]. They replaced the Mn^{3+} ion by non-distorting cations through the formation of solid solution of tetragonal Mn_3O_4 and cubic AFe_2O_4 spinel.

Valence state of Cu in copper manganite has been a subject of considerable interest. Magnetic susceptibility and electrical conductivity suggest that Cu should be Cu^{1+} in copper manganite while X-ray absorption data [17] indicates the presence of Cu^{2+} . Sinha, Sanjana and Biswas [18] first synthesized copper manganite and the observed cubic structure of CuMn_2O_4 was explained on the basis of the formula $\text{Cu}^{1+}[\text{Mn}^{3+}, \text{Mn}^{4+}]\text{O}_4$ which was supported by electrical properties. Sabane [19] studied the magnetic properties and the temperature dependence of electrical conductivity of various manganites and their solid solutions. Naik [20] prepared number of spinels having formula

$\text{Cu}_x\text{Me}_{1-x}\text{Me}_2\text{xFe}_{2-2x}\text{O}_4$ where $\text{Me} = \text{Cu}^{2+}, \text{Ni}^{2+}, \text{Co}^{2+}, \text{Zn}^{2+}$ and Mn^{2+} . Their structural, electrical and magnetic properties were studied in order to throw some light on the cation distribution and valence states of Cu and Mn in these copper manganese spinels.

4.2 RESULTS AND DISCUSSION

Conventionally manganites are prepared by a solid state reaction [18-20]. Coprecipitation technique also has been used to prepare spinel ferrite [21] and manganite [22]. We attempted the synthesis of copper manganite by both the techniques namely ceramic and coprecipitation.

4.2.1 Ceramic technique - XRD studies

Copper manganite prepared by this technique was analysed by various characterization techniques. Fig. 2 shows the XRD of sample C-1, heated at various temperatures between 600-950°C. From the figure, it is clear that the manganite formation starts at $\approx 750^\circ\text{C}$. The spectrum shows the peaks of unreacted Mn_2O_3 only but unreacted CuO is not seen. Mn_2O_3 phase persists upto 880°C. Above 880°C, the peaks corresponding to Mn_3O_4 are observed which persist upto 950°C along with the copper manganite peaks.

Low angle XRD studies were done on sample C-1 in order to probe into the surface structure. Fig. 3 clearly indicates CuMn_2O_4 as the main phase present on the surface.

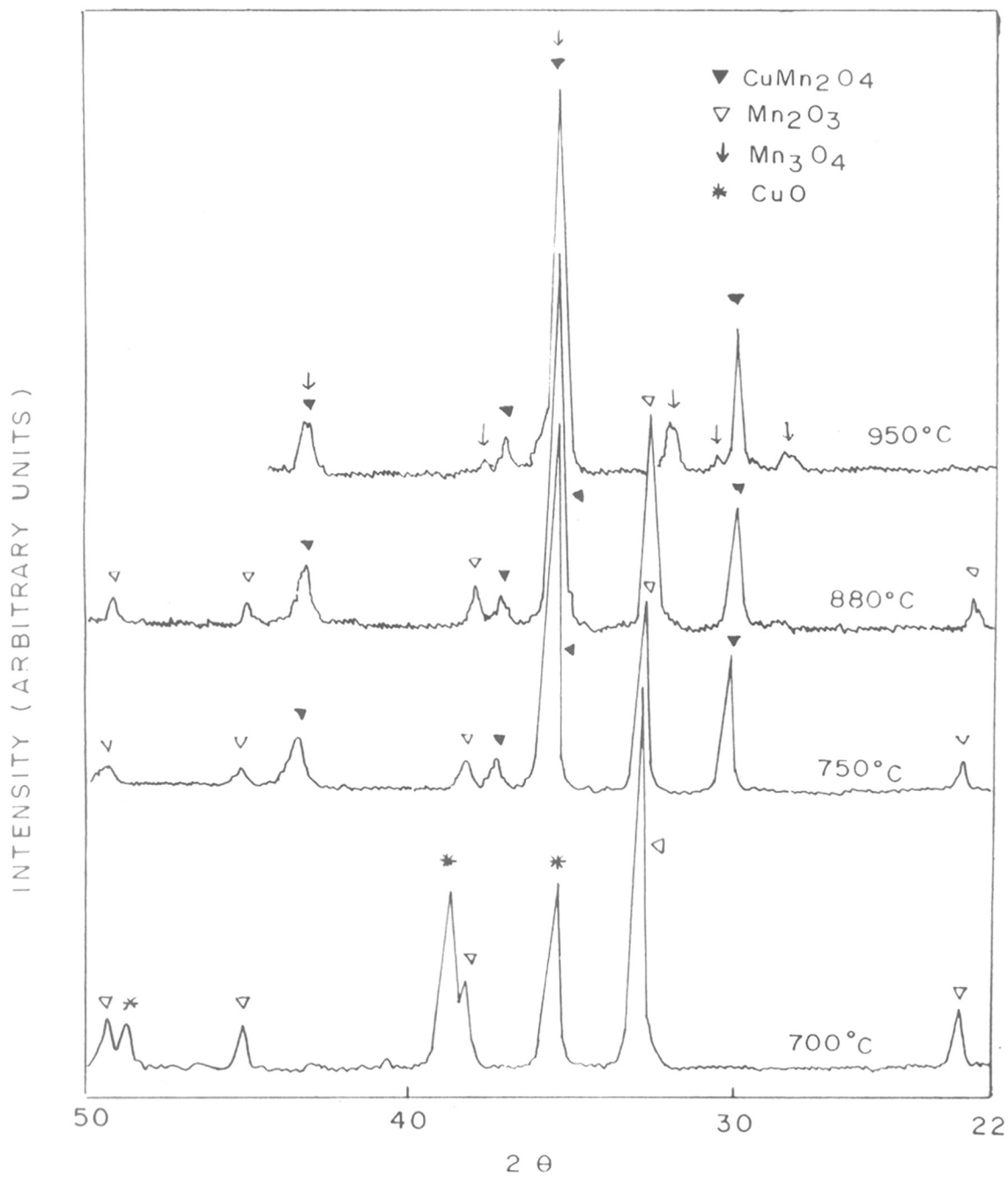


FIG.2 : XRD of sample C-1, heated at various temperatures between 600 - 950°C.

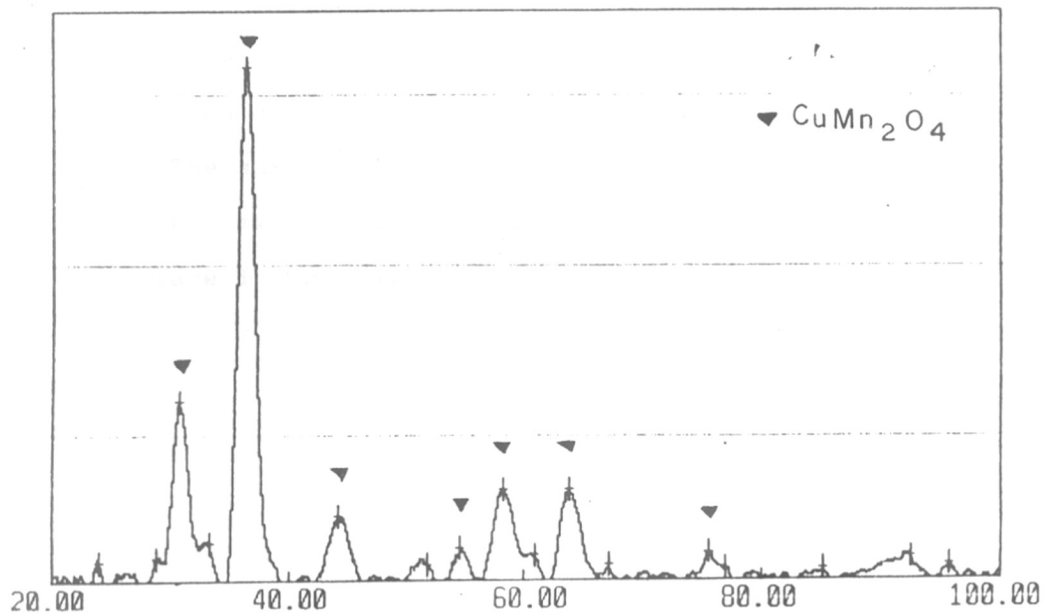


FIG.3 : Low angle X - ray diffractogram of sample C-1

DTA/DTG/TG studies : For the thermochemical studies physical mixture of CuO and Mn_2O_3 in the required ratio (sample C-1) was used. The weight changes and energy changes which occurred during heating from RT to 1200°C are shown in Fig. 4. The sample shows a broad exothermic change around 209°C . This may be due to some nonstoichiometry of oxygen taking place in CuO (as was observed in the case of DTA of CuO only). As the temperature increases three endothermic peaks appear at $T = 813, 991$ and 1165°C successively. The peak at $T = 991^\circ\text{C}$ is associated with a weight loss of 2.41%. This change may be ascribed to the decomposition of unreacted Mn_2O_3 to Mn_3O_4 (supported by the XRD results) and further at $T = 1165^\circ\text{C}$ the phase change from the tetragonal to cubic structure of Mn_3O_4 is observed [10]. The peak at $T = 813^\circ\text{C}$ seems to be related to the reaction between the oxides of copper and manganese. The assignment is purely a speculative one at this stage.

ESCA studies : Sample C-1 after calcination at $950^\circ\text{C}/24$ h was examined with the help of X-ray photoelectron spectroscopy. Carbon, contaminated in the spectrometer was used as an internal standard. Table 1 gives the XPS data of sample C-1 while Table 2 gives the multiplet splitting and spin orbit splitting of manganese in various oxidation states [23,24] along with that obtained for sample C-1. Multiplet splitting of $\text{Mn } 3s_{1/2}$ is clearly observed but for Cu , $2p_{1/2}$ and $2p_{3/2}$ spectrum does not show any clear satellite structure.

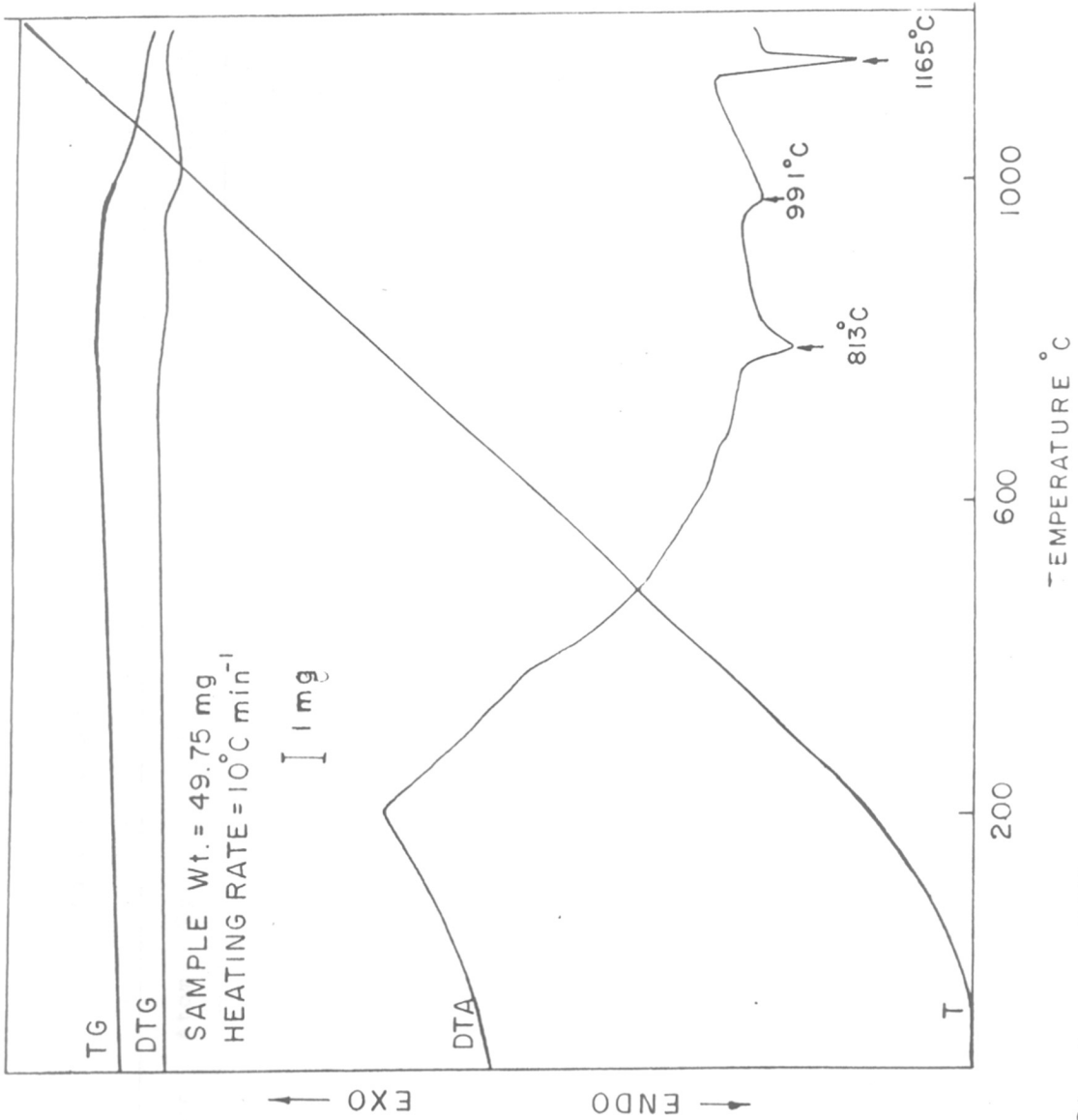


Fig. 4: Simultaneous DTA/DTG/TG curves of sample C-1 (ceramic method)

Table 1 : XPS data for sample C-1

Sample	Atom	2p _{1/2}	2p _{3/2}	3s _{1/2}	3p _{3/2} ; 3p _{5/2}	3d _{5/2} , 3d _{7/2}
C-1	Mn	652.48	641.08	83.6 89.6	47.92	3.32
	Cu	950.80	930.64		75.92	

Table 2 : Multipletsplitting and spin orbit splitting of Manganese in various compounds [24]

Compound	Multiple splitting eV	Spin-orbit splitting eV
Mn metal	4.1	
MnO	6.1	11.6
Mn ₂ O ₃	5.5	11.6
Mn ₃ O ₄	5.3	11.6
MnO ₂	4.5	11.6
Sample C-1	≈ 6.0	11.4

SEM studies : Fig. 5 shows the microstructure of the sample C-1 (heated at $950^{\circ}\text{C}/24\text{ h}$). The size of the particle is $\geq 2\ \mu\text{m}$.

4.2.2 Coprecipitation technique - XRD studies

Sample D-1 was heated at various temperatures between 200 and 950°C and the corresponding changes occurring in the structure are shown in Fig. 6. XRD of the coprecipitate shows Mn in the form of Mn_3O_4 while copper might be present in amorphous form as its signature is not recognized from the XRD pattern. As the coprecipitate is heated from 200°C onwards, XRD shows CuMn_2O_4 as a main phase at 300°C with one extra peak at $2\ \Theta = 44.7$ degrees which could not be identified. At temperatures $T \geq 600^{\circ}\text{C}$, Mn_2O_3 phase appears in addition to CuMn_2O_4 but there is no evidence for copper. This Mn_2O_3 gets converted to Mn_3O_4 at 950°C .

DTA/DTG/TG studies : Thermochemical changes of sample D-1 are shown in Fig. 7. The endothermic change at $T = 80^{\circ}\text{C}$ is associated with the loss of water from the coprecipitate. Then the sample shows three endothermic changes centered at $T = 803$, 967 and 1152°C ; similar to those of the sample C-1. The DTG shows weight loss at $T = 967^{\circ}\text{C}$ only. The peaks at 967 and 1152°C are again assigned to the change, $\text{Mn}_2\text{O}_3(\text{unreacted}) \rightarrow \text{Mn}_3\text{O}_4$ and tetragonal $\text{Mn}_3\text{O}_4 \rightarrow$ cubic Mn_3O_4 respectively. The energy change at $\approx 803^{\circ}\text{C}$ is again related to the reaction between copper oxide and manganese oxide. The analysis of the simultaneous DTA/DTG/TG plot, along with the



FIG. 5 : Scanning electron micrograph of
Sample C-1 (heated at 950°C)

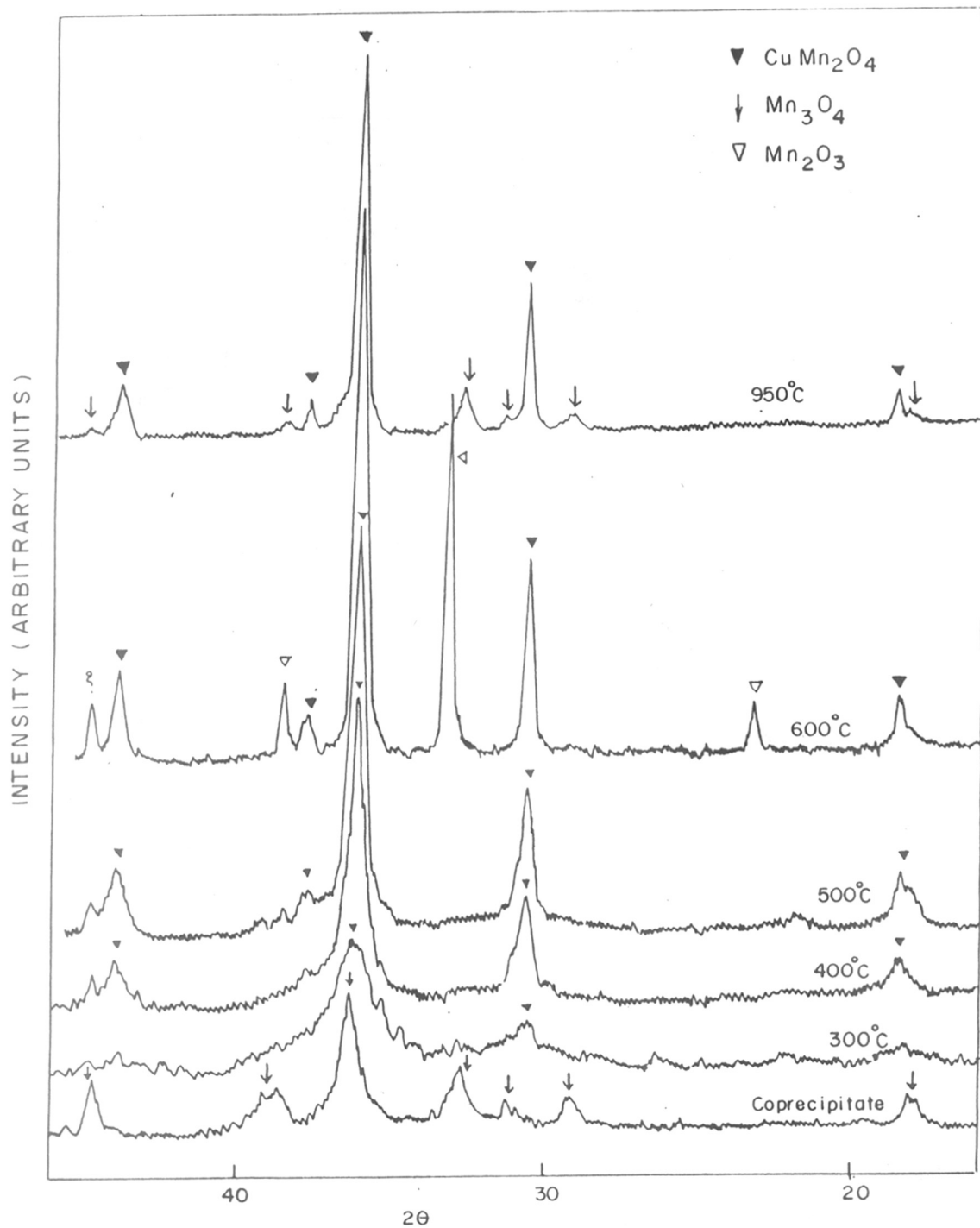


Fig.6 : X-ray diffraction patterns of sample D-1 (Coprecipitation method) heated at various temperatures between 200 - 950°C.

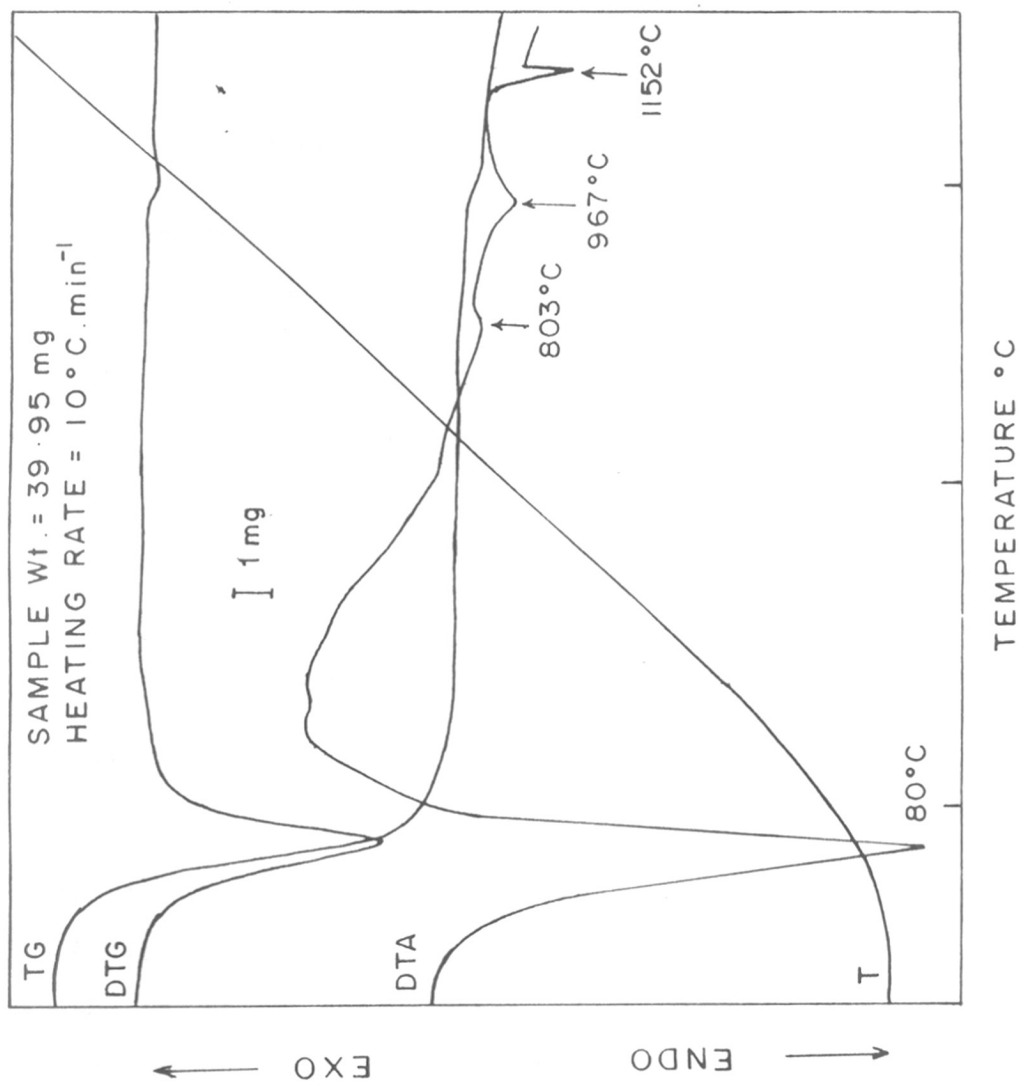


FIG.7 : Simultaneous DTA /DTG /TG curves for sample D - 1 (coprecipitation method).

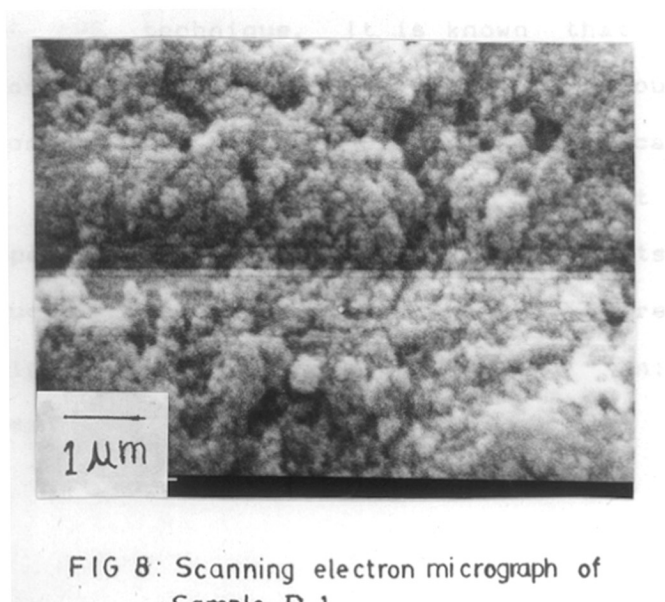
XRD studies do not spell out the exact mechanism and may have to be very carefully analysed.

SEM studies : Fig. 8 shows the particle size and its distribution in the case of the coprecipitated sample D-1. The size of the coprecipitated particles is $\approx 0.2 \mu\text{m}$.

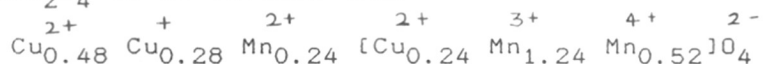
4.3 SUMMARY

XRD results indicate that copper manganite formation is initiated at much lower temperature $\approx 300^\circ\text{C}$ in the case of coprecipitation technique, compared to $T \approx 750^\circ\text{C}$ required in the case of ceramic technique. Presence of $\text{Mn}_2\text{O}_3/\text{Mn}_3\text{O}_4$ and absence of CuO during the course of reaction requires rigorous characterization of the product at various stages. The lowering of reaction temperature can be ascribed to the finer, uniform and more active particles prepared by the precipitation technique.

XPS results of CuMn_2O_4 (prepared by ceramic method) seem to be quite different but at the same time an interesting one. We observe no satellite structure for Cu^{2+} which is one of the expected oxidation state of Cu in the copper manganite structure. Absence of Cu^{2+} on the surface leads to the consequence that Cu^{1+} should be present, compelling Mn to change its oxidation state to $4+$ to maintain the charge neutrality. But surprisingly we do not have any evidence of Mn^{4+} state; instead the multiplet splitting of Mn is of the order of $\approx 6.0 \text{ eV}$, which is close to the value of Mn^{2+} . Thus XPS shows that the surface of CuMn_2O_4 prepared



by ceramic technique contains Cu^+ and Mn^{2+} . The low angle XRD which gives the surface picture, also indicates CuMn_2O_4 to be the main phase. Most recent structure proposed for CuMn_2O_4 is as follows [25]



where the author has been able to resolve not only between various Cu and Mn oxidation states but between the same cation occupying tetrahedral and octahedral sites with the help of XPS technique. It is known that the degree of inversion strongly depend upon the various experimental conditions. In conclusion, our results indicate that various species like Cu^{1+} , Cu^{2+} , Mn^{2+} , Mn^{3+} do exist in our samples of copper manganite. Extensive experiments using modern techniques (EXAFS, XANES, FTIR, MASSNMR) are expected to throw light on the very complicated electronic structure of copper manganite.

REFERENCES

1. W.H. Bragg,
Nature, 95 (1951) 561; Phil.Mag., 30 (1915) 305.
2. G. Aminoff,
Zeitschr.f.Krist., 64 (1926) 475.
3. T.F.W. Barth and E. Posnjak,
Z.Krist, 82 (1932) 325.
4. H. Forestier,
C.R. Acad.Sci. Paris, 192 (1931) 842.
5. E.J.W. Verwey, P.W. Haayman and F.C. Romeijn,
J.Chem.Phys., 15 (1947) 181.
6. F.de Boer, J.H. Van Santen and E.S.W. Verwey,
J.Chem.Phys., 18 (1950) 1032.
7. E.J.W. Verwey and E.L. Heilmann,
J.Chem.Phys., 15 (1947) 174.
8. E.W. Gorter,
Philips Res.Report, 9 (1954) 229.
9. J.D. Dunitz and L.E. Orgel,
J.Phys.Chem.Solids, 3 (1957) 20.
10. H. McMurdie and E. Golovalo,
J.Res.Natl.Bureau Stds., 41 (1948) 589.
11. E.F. Bertaut,
J.Phys.Radium, 12 (1951) 252.
12. S. Miyahara,
J.Phys.Soc. Japan, 17 Suppl. B-1 (1962) 181.
13. S. Miyahara, K. Muramori and N. Tokuda,
J.Phys.Soc. Japan, 16 (1961) 1490.
14. I.T. Sheftel, A.I. Zaslavskii and E.V. Kurlina,
Soviet Physics Solid State, 3 (1962) 1979.
15. K.S. Irani, A.P.B. Sinha and A.B. Biswas,
J.Phys.Chem. of Solids, 23 (1962) 711.
16. G.I. Finch, A.P.B. Sinha and K.P. Sinha,
Proc.Roy.Soc. London, A242 (1957) 28.
17. A. Miller,
J.Phys.Chem.Solids, 29 (1968) 633.

18. A.P.B. Sinha, N.R. Sanjana and A.B. Biswas,
Acta Cryst., 10 (1957) 439.
19. C.D. Sabane,
Ph.D. Thesis, University of Poona, (1960).
20. B.N. Naik,
Ph.D. Thesis, University of Poona, (1967).
21. R.G. Kulkarni and H.H. Joshi,
J.J. Solid State Chemistry, 64 (1986) 141.
22. P.M. Khopkar, J.A. Kulkarni and V.S. Darshane,
Thermochimica Acta, 93 (1985) 481.
23. J.S. Foord, R.B. Jackman and G.C. Allen,
Phil.Mag.A, 49 (1984) 657.
24. M. Oku, K. Hirokawa and S. Ikeda,
J. Electron Spectroscopy and Related Phenomenon,
7 (1975) 465.
25. M. Lenglet, A.D'Huysser, J. Kasperek, J.P. Bonnelle and
J. Durr.,
Mat.Res.Bull., 20 (1985) 745.

S.D. Kulkarni

708L/85

LIST OF RESEARCH PUBLICATIONS

1. XPS studies of AMn_2O_4 (A=Ni, Cu, Zn, Cd and Mg).
S.D. Kulkarni, A.P.B. Sinha and S.K. Date.
 Solid State Physics Symposium, 27-C (1984) p.100.
2. X-ray Photoelectron Spectroscopic Studies on Oxides of Manganese and Maganites: An Overview.
S.D. Kulkarni, C.E. Deshpande, A.P.B. Sinha and S.K. Date.
 Proceedings of the National Seminar on X-ray Spectroscopy and Related Areas, 1985, p.50.
3. Synthesis of Chemically Coprecipitated Hexagonal Sr-ferrite and its Characterization.
S. D. Kulkarni, J.J. Shrotri, C.E. Deshpande and S.K. Date.
 J. Mater. Sci., 24 (1989) 3739.
4. An improved process for the Preparation of High Intrinsic Coercivity Sr-ferrite Powder.
 S.K. Date, C.E. Deshpande, J.J. Shrotri and S.D. Kulkarni.
 Patent application filed on 7-11-88, No. 963/DEL/88.
5. Synthesis of Ultrafine Particles of Strontium Ferrite by Chemical Coprecipitation with Sodium Hydroxide.
 S.K. Date, C.E. Deshpande, S.D. Kulkarni and J.J. Shrotri.
 Advances in Ferrites, International Conference on Ferrites, ICF-5 held at Bombay 1989. p.55.
6. Thermochemical Characterization of Ultrafine Sr-hexaferrite.
S. D. Kulkarni, C. E. Deshpande, J. J. Shrotri, V. G. Gungikar and S. K. Date.
 Thermochemica Acta, 153 (1989) 47.

ACKNOWLEDGEMENT

I am deeply indebted to my research guide, Dr. S.K. Date for his valuable guidance. His enthusiastic, optimistic and cooperative attitude has helped me a lot during the course of these investigations.

I thank Dr. P. Ratnasamy, Head, Physical and Inorganic Chemistry Divisions, for his kind support for this work.

I wish to share this moment of happiness especially with Mr. S.S. Sardesai, University of Poona, whose inspiring guidance and continuous encouragement, made me to see the delights of a research career. I am fortunate to have a number of stimulating discussions at various stages of this work, which has induced in me, analytical thinking.

I express my sincere thanks to Dr. C.E. Deshpande for his critical discussions and valuable suggestions throughout the course of this work, and thanks are also due to Mrs. J.J. Shrotri for on the spot help and guidance in the preparative work. I am thankful to Dr. S.D. Sathaye, Dr. S.D. Pradhan and Dr. V.G. Gunjekar for many useful discussions about the experimental results.

I am grateful to all the staff members of special instrument laboratory, who extended their cooperation in characterization of the materials, particularly Mr. M.V. Kuber (XRD), Dr. V.G. Gunjekar (thermal studies), Dr.(Mrs.) A. Mitra (SEM), Dr.S. Badrinarayan and Dr. A.B.

Mandale (XPS), Mrs. A. Belhekar and Miss M. Agashe (IR) and Mr. R.F. Shinde and Dr. P.P. Bakare (Magnetic Measurements).

I am also thankful to Mr. H.B. Harwade and Mr. Ramakrishnan for their technical assistance.

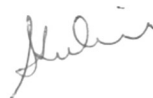
I take this opportunity to express my deep sense of gratitude to my parents Mr. A.M. Ranade and Mrs. S.A. Ranade and other family members for their continuous encouragement throughout my educational career. I was fortunate to have their unflinching support to face all the odds with patience and courage, which were inevitable during the course of this work.

I am also grateful to my husband, Mr. Dilip Kulkarni, for his continuous encouragement and generous help and my in-laws for their cooperation during the course of these studies.

Last but not least are the sincere thanks to Lilu who inspite of many difficulties, extended her whole hearted cooperation in typing of the manuscript of this thesis.

Encouragement and cooperation from all my friends is also being acknowledged.

I wish to thank Director, National Chemical Laboratory, Pune - 411 008, for kindly permitting me to submit this work in the form of a thesis.



(Mrs. Shailaja D. Kulkarni)